MEASUREMENT AND MODELING OF WATER IN POROUS MEDIA USING MILLIMETER-WAVE AND TERAHERTZ SPECTROSCOPY

by

Jacob Bouchard

A Dissertation

Submitted to the Faculty of the

WORCESTER POLYTECHNIC INSTITUTE

in partial fulfillment of the requirements for the

Degree of Doctor of Philosophy

in

Physics

December 2023

APPROVED:

____

Professor Douglas Petkie, Advisor, Physics Department, WPI

____

Professor Lyubov Titova, Committee Member, Physics Department, WPI

____

Professor Raisa Trubko, Committee Member, Physics Department, WPI

____

Doctor Shannon Eichmann, Committee Member, Petroleum Engineering Specialist, Aramco Research Center

APPROVED:

Professor Douglas Petkie, ______________________________
Advisor Signature/Date
Physics Department, WPI

Professor Lyubov Titova, ______________________________
Committee Member, Signature/Date
Physics Department, WPI

Professor Raisa Trubko, ______________________________
Committee Member, Signature/Date
Physics Department, WPI

Doctor Shannon Eichmann, ______________________________
Committee Member, Signature/Date
Petroleum Engineering Specialist, Aramco Research Center

ACKNOWLEDGEMENTS

There are many people who I would like to thank for their help and friendship both over the course of my eight and a half years at WPI and throughout my life.

First, I would like to thank my family for their unending support. To my parents Robert and Robin, thank you for teaching me the satisfaction that comes with a job well done and giving me the confidence to explore the unknown. Your resourcefulness and DIY spirit has never ceased to inspire me. To my sisters Sarah and Jillian, thank you for always being there for me, from venting to just goofing around or enjoying a good meal together, time spent with the two of you has helped get through some of tougher parts of this work.

To my advisor Doug Petkie, I cannot thank you enough for all that you have done for me at WPI. From bringing me into your lab with no prior experience as a junior, showing me the joy of research, giving me opportunities to grow as a student and scientist. There is not nearly enough time or room to describe all of the ways you have helped me during my time at WPI, but I hope you know that I will always look back at the time I spent working with you fondly. Not only have you influenced my development as a researcher but as a person too. Your leadership style and fun personality have made working with you for the past 5 and a half years a pleasure.

To my committee members Dr. Lyubov Titova, Dr. Raisa Trubko, and Dr. Shannon Eichmann, thank you for your insight and advice.

To Dr. Shannon Eichmann, Dr. Martin Poitzsch, Dr. Hooisweng Ow and the team at Aramco Americas, thank you for excellent project and all your work and support. Our collaboration was a highlight of my time as a PhD student.

To the Center for Advanced Research in Drying, the Massachusetts Clean Energy Commission, and the United States Department of Energy. Thank you for financially supporting the smart dryer project and my work to develop a novel moisture sensor.

To my friend and colleague Dr. Jim Eakin, thank you for always being there for me. You have been so kind and helpful over the years. From helping to order and set up equipment, plan experiments, giving me networking advice, discussing research problems, inspiring many hobbies, and giving me space to vent, you have helped immensely. I will always cherish our friendship.

To my collaborators at the Multiscale Heat Transfer Laboratory at WPI, thank you for your insights on industrial drying and for providing numerous samples.

To my lab mates Vuong Truong, Peter Hedlesky, Jacen Urbaniak, José Acosta, and Alex Kiely, thank you for your help in setting up experiments, discussing results, finding math errors, and helping me hone my crossword skills. You have all made the lab an enjoyable place to work.

To Cecilia Dean, Michelle Vanadia, Anna Valdez, Simon Rees, Sahana Venkatesh, Ming Tang, Abigail Johnson, Joshua Petkie, José Acosta, and Jacen Urbaniak, thank you for all your contributions to develop the moisture sensor.

To all my friends and coworkers at the LEAP lab and the physics department, thank you for your friendship, advice, and support.

To my friends and former colleagues at SI2 Technologies, an ARA company, thank you for giving me the opportunity to work with all of you and learn many new skills.

I have been exceedingly lucky throughout my life to have been taught and supported by many wonderful teachers and professors. I would like to thank all of them and specifically identify two teachers who I feel greatly impacted the course of my life. My 4th grade teacher Mrs. Ernestine Tulumello, who taught me the value of personal responsibility and instilled in me a work ethic which has carried me through my academic career. And my 9th grade Biology teacher and friend Mr. Forest Henderson who taught me to follow my interests and passions to the fullest and the power of a positive attitude.

Finally, to all my friends outside of the academic world, thank you for your continued support and thank you for understanding when I disappear when things in the lab get hectic.

Throughout the course of this work, I have gotten to read many interesting papers and texts which have greatly deepened my understanding of the field. Some of them have also given me a deeper appreciation for the sense of humor shared by scientists. I would like to reproduce a quote which I found in Claus F. Klingshirn's excellent book Semiconductor Optics, ISBN: 3540268464, 9783540268468. Klingshirn attributes the quote to E. Mollwo, but its exact origins are unknown.

"The author hopes that, with respect to this work, the deviations from exact scientific truth and perfect understandability are in a reasonable balance."

Regardless of the origin of the quote, I share this sentiment with respect to this thesis and thank you for reading it.

TABLE OF CONTENTS

ABSTRACT

In many industrial and manufacturing processes, determining the presence and concentration of water in a variety of materials is necessary. In some of these situations, taking traditional, contact dependent, measurements are either impossible or impractical. By exploiting the strong interaction between THz radiation and water, a non-contact volumetric moisture sensor can be designed. This sensor will operate within the band from 100 GHz to approximately 1 THz, allowing it to be tuned based on the optical thickness of the sample under inspection. However, the optical thickness not only depends on the complex dielectric constant, but also on the structure of the sample and can be a strong function of frequency. Optimizing the sensor performance depends on the details of the signature science and phenomenology of each specific application. This work will outline two distinct applications where THz is used to detect moisture to augment and improve industrial processes. The two applications are: 1) A non-contact volumetric moisture sensor for paper and pulp manufacturing (sponsored by US DOE) and 2) A novel porosity imaging technique to measure bulk porosity as well as image pore size distribution in carbonate rocks for oil wellsite evaluation (sponsored and in collaboration with Aramco Americas: Aramco Research Center - Houston).

LIST OF FIGURES

LIST OF TABLES

1 INTRODUCTION

Water is arguably the most important and ubiquitous substance on Earth. It is vital to all known forms of life, and it sustains a variety of ecosystems, covering approximately 71% of the planet. Water also finds uses in a wide range of industrial processes including fabrication, processing, and dilution. In 2015 alone, industrial water usage was estimated at 14,800 million gallons per day [1]. In many of the industrial processes that use water, knowing where that water is and in what volume it is present in is crucial for maintaining process quality and consistency. As such, considerable work has been done to develop systems and sensors to measure the presence and volume of water. These systems work to balance sensitivity, cost, and speed of measurement, as well as conforming to other limitations imposed by the specific processes that they are designed to monitor.

Although the moisture sensing market is quite large and mature, niche cases still exist where suitable moisture sensors have not been developed for specific processes. In this dissertation I will detail work performed to develop sensing systems for two such niche processes. To develop these systems, I will be utilizing the relatively novel technique of terahertz (THz) spectroscopy which offers certain attractive qualities. The two processes which I discuss in this work are quite different from each other, but both offer interesting challenges.

The first process considered in this work requires not just the development of a moisture sensor, but the development of an entire methodology for the mapping of microporosity in oil wellsite core samples. The second process is a more traditional industrial process where a sensor for measuring the volumetric moisture content of paper samples must be developed, the key challenge here being the required accuracy and geometrical constraints.

2 BACKGROUND

2.1 INDUSTRIAL MOISTURE SENSING

With the use of water in such a wide variety of industrial processes, it is no surprise that there is a large market for moisture sensors. In many of these processes determining the presence and concentration of water within materials is often crucial to ensure efficiency, quality, and repeatability. To integrate into any industrial process, many aspects of the process must be taken into consideration when designing a moisture sensor. There are three main parameters of a moisture sensor that are considered, these are their operable moisture range, line compatibility, and sample compatibility. A sensor's operable moisture range is simply what range of moisture content that the sensor works over, this range can be expressed in either volumetric moisture content (θ_w) (equation 1), wet basis moisture content (WBMC) (equation 2), or dry basis moisture content (DBMC). A sensors line compatibility is how compatible the sensor is with process line integration, that is whether it can be used as part of an automated continuous process or not. A sensor's sample compatibility is a factor of how well the sensor works with samples that vary in thickness, roughness, color, reflectance, and dielectric properties. Industrial moisture sensors made to nondestructively measure solid samples can be split into three categories based on their method of operation. These categories are gravimetric, infrared, and microwave. An overview of these methods follows.

$$\theta_w = \frac{V_{water}}{V_{water} + V_{sample}} \tag{1}$$

$$\mathrm{WBMC} = \frac{\mathrm{Mass}_{\mathrm{water}}}{\mathrm{Mass}_{\mathrm{water}} + \mathrm{Mass}_{\mathrm{sample}}} * 100 \tag{2}$$

$$\mathrm{DBMC} = \frac{\mathrm{Mass}_{\mathrm{water}}}{\mathrm{Mass}_{\mathrm{sample}}} * 100 \tag{3}$$

2.1.1 Gravimetric Moisture Sensing

The gravimetric method for measuring moisture content is the simplest method considered here. This method simply uses a balance of suitable precision to measure the mass of the sample when it contains no water and then again when it contains an unknown amount of water. By comparing the difference in mass between the two measurements and assuming that the only two materials present are your initial sample and some amount of water, you can calculate the mass of water in your sample. This method can be augmented by using a drying system and knowing the drying curve of a sample, which is the rate at which the sample dries versus its moisture content. By weighing a sample containing an unknown amount of water, drying it a small amount, and then reweighing it and comparing the change in mass with the known drying curve of the sample, the moisture content of the sample can be calculated [2].

Both the basic gravimetric method and the loss on drying (LOD) method provide very accurate moisture content measurements over the entire range of moisture contents. Their sample compatibilities are also quite large, if the sample can be weighed and its dry mass is known, or in the case of LOD method as long as its drying curve is known, the gravimetric method can be used. The key limiting factors in the accuracy of moisture content measurements taken using a gravimetric method are the accuracy of the mass balance used and in the case of the LOD method, the accuracy of the drying curve and drying method used. Where the gravimetric method is lacking is in its line compatibility. With its requirement of high accuracy mass measurements, care must be taken when measuring the mass of a sample and a well-defined volume of sample must be measured. These requirements limit the gravimetric method to use in batch process operations.

2.1.2 Infrared Moisture Sensing

The infrared (IR) method for moisture sensing is based on the strong interactions between liquid water molecules and IR radiation (λ = 700 nm to 3 μm, f = 428 THz to 100 THz). In this range, the electromagnetic radiation induces hydrogen vibrations in the molecules which results in very strong absorption of the wave [3]. The IR method relies on there being a large contrast in the absorption due to liquid water and the dry sample to calculate moisture content. IR sensors emit IR radiation which propagates onto the sample to be measured, depending on the moisture content of the sample some of this radiation is absorbed while the rest of it is reflected to the sensor where the intensity of the radiation is measured [4]. From this measurement, the moisture content of the sample is calculated by comparing the intensity of the measured radiation with the intensity of the radiation emitted and with the known absorbance due to the dry sample.

The IR method provides fast and accurate moisture content measurements in an easy to integrate package. An example of an industrial IR moisture sensor, an OMNIR from Finna Sensors is pictured in Figure 1 showing its simple and compact packaging. The OMNIR has a measurement rate of 60 samples per second, the ability to measure samples from 0.1% WBMC to 95% WBMC with an accuracy of ±0.1% WBMC. These specs are on par with most sensors on the market, which quote operating moisture ranges from 1% to 100% WBMC. This is not surprising given the high sensitivity of IR radiation to moisture; however, these moisture ranges can be deceiving when talking about IR moisture sensors. The particularly strong interactions between the sample and the IR leads to relatively poor penetration depths within wet samples, with literature listing

IR penetration depth between 1 mm and 5 mm depending on the sample [5-8]. Given a sample thicker than the penetration depth, the IR sensor will effectively average the overall moisture content of the sample, neglecting any possible moisture content variations within the sample, which may not always be valid. In terms of sample compatibility, IR moisture sensors are able to measure a wide variety of samples but will have issues with samples that absorb IR radiation to a similar degree to water, thick samples with large moisture content variations, and typically are designed to work with samples whose colors do not vary much [9]. An additional capability of the IR moisture sensing method is that the short wavelengths allow for high resolution moisture content imaging of relatively smooth samples [10].

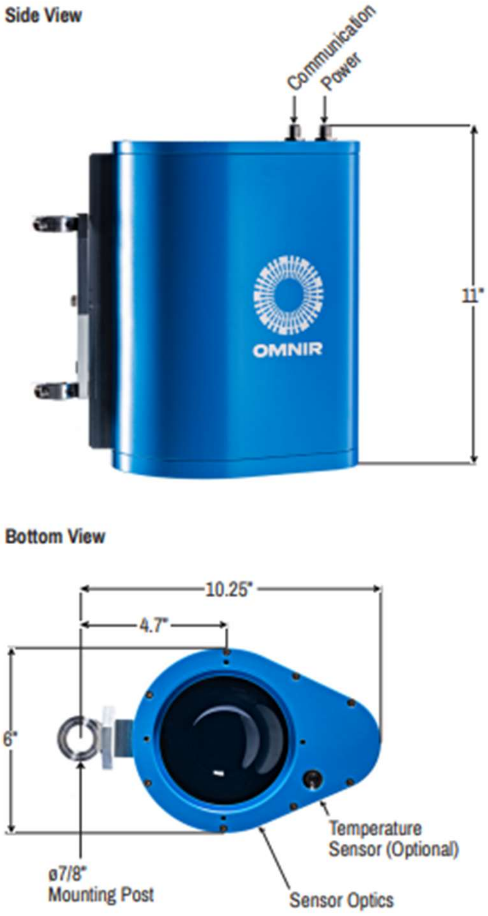

Figure 1. Diagram of the OMNIR infrared moisture sensor from Finna Sensors, showing its simple, compact, and line compatible packaging. Sourced from [11].

2.1.3 Microwave Moisture Sensing

The microwave method of moisture sensing uses electromagnetic radiation in the frequency range from 2 kHz to 18 GHz [12-14] and relies on the absorption of the radiation due to liquid water. Moisture sensors using the microwave method can achieve operable moisture content ranges from 1% to 100% but require quite thick samples to achieve sensitivity in the low range. This is because of the relatively small interactions between liquid water and frequencies in the microwave range. This lack of strong interaction can be used to achieve compatibility with much thicker samples such as bulk grain, lumber, and crushed rock, which would be incompatible with the IR method. This, however, makes microwave sensors incompatible with thin samples. The microwave method does still require the absorbance due to the dry sample to be much less than the absorbance due to liquid water. This sample dependence makes it difficult to quantify the overall performance of these sensors as the moisture range depends on the thickness and porosity of the sample while the accuracy will depend on the total moisture content. As far as line compatibility, microwave moisture sensors can and already have been integrated into many different industrial process lines. Currently, industrial adoption of moisture sensors using the microwave method is low compared to IR moisture sensors, with only a few microwave moisture sensors available on the market.

2.1.4 Nuclear Method

Like the microwave method, the nuclear method passes energy through a sample and measures the power that makes it through, but the nuclear method uses either beta or gamma radiation instead of microwave radiation. Nuclear moisture meters have higher output power than microwave sensors and this allows them to measure thicker samples and have higher sensitivities in thin samples [15]. Currently this is the method employed in many paper manufacturing plants but there are some concerns with its use. The main two concerns are the licensing and specialist personnel that are needed to operate and maintain the sensor, and the safety concerns that come with the ionizing radiation emitted by the sensor.

2.2 TERAHERTZ SCIENCE

Electromagnetic radiation in the sub-THz range (~60 GHz) was first reliably generated and measured by Jagadish Chandra Bose in 1895 [16]. In his experiments, Bose demonstrated the unique ability of waves of these frequencies to propagate over long distances and through dielectric materials. Since those early experiments, the field of millimeter wave (mmWave) or terahertz (THz) science has refined techniques to generate and detect radiation in the band from 10 GHz to 10 THz. First practically demonstrated in 1989 [17], THz time domain spectroscopy (THz TDS) is a technique which allows for generation and detection of frequencies over a very large bandwidth simultaneously. In 1995 it was demonstrated that THz TDS could also be used to create high quality images [18]. Work in the field has developed to a high degree of sophistication with off-the-shelf components and systems coming to market for lab scale use in the past several years.

Outside of the lab, the communications industry has been looking at bands within the THz band for new high speed communication standards [19]. This possible application, as well as the development of THz sources for certain RADAR [20, 21] has resulted in the price of THz sources in certain bandwidths becoming more affordable and thus attractive for industrial development.

2.2.1 History of Electromagnetic Science

In this section I will briefly review the history of sources and detection methods for electromagnetic science. This review will discuss early experiments in the late 1800s up through to the modern day and aims to provide an understanding of the current state of the field.

2.2.1.1 Early Experiments and Developments

Starting with Maxwell's publication of "A dynamical theory of the electromagnetic field" in 1865, where he posited that electric and magnetic fields travel through space at the speed of light [22], physicists sought to experimentally prove the existence of these electromagnetic waves. Over 30 years later, in 1886 Heinrich Hertz began a series of experiments using spark gap transmitters and detectors. His transmitter consisted of two copper wires which were 1 meter in length with a small “spark gap” between them and large zinc spheres on the opposing ends[23]. An induction coil operating at approximately 30 kV was attached to this oscillator and caused a spark to jump across the gap between the wires. The acceleration of charges involved in this “jumping” spark was what caused the production of electromagnetic waves which were polarized parallel to the direction of the spark. The 30 cm zinc spheres, which functioned as resonators, made it so Hertz’s oscillator functioned at approximately 50 MHz.

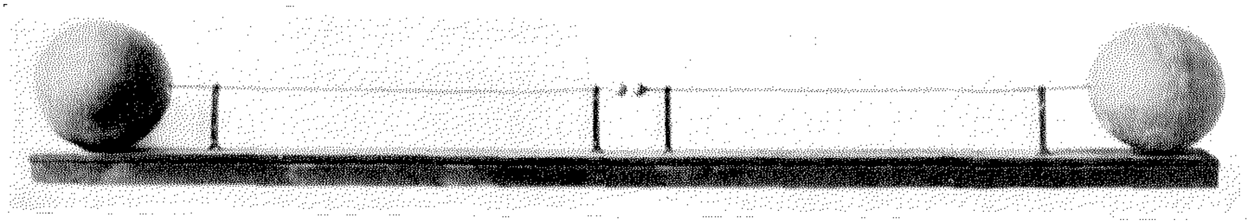

Figure 2. A photo of Heinrich Hertz’s first spark gap oscillator. The two copper wires are approximately 1 meter in length with zinc spheres of diameter 30 cm and a spark gap in the middle. This oscillator was attached to an induction coil and produced horizontally polarized electromagnetic waves[23].

To detect the electromagnetic waves generated by his oscillator, Hertz made use of so called “resonators” made of coiled copper wire which were carefully “tuned” to the frequency of the oscillator. The waves produced by the oscillator would travel through the air and induce a current in the resonator. This induced current in the resonators, would cause small sparks to jump across their own corresponding spark gaps. The width of the gaps on the resonators were adjustable with use of a micrometer allowing for the measurement of the induced spark width and thus the strength of the electromagnetic wave incident upon the resonator.

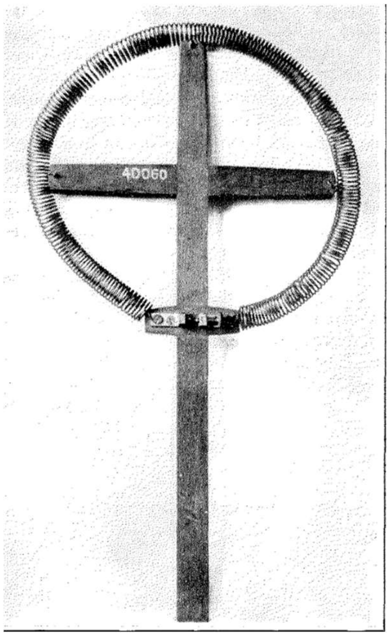

Figure 3. One of Hertz's resonators with its coiled copper wire antenna and spark micrometer acting as the detector[23].

Hertz went on to investigate the polarizability of these electromagnetic waves in order to complete his verification of Maxwell’s predictions. With this work done, Hertz supposedly stated when asked about the practical importance of his results “It's of no use whatsoever ... this is just an experiment that proves Maestro Maxwell was right—we just have these mysterious electromagnetic waves that we cannot see with the naked eye. But they are there.”[24].

After Hertz’s early death in 1894, Oliver Lodge presented a lecture on Hertzian waves at the British Royal Institution. Lodge demonstrated the generation and detection of electromagnetic waves across longer distances than were used in Hertz’s original work. He was able to achieve these longer distances using a new detector which was developed 4 years earlier by Édouard Branly, called a coherer (pictured in Figure 4). The coherer made use of the electrical contact resistance phenomena, which is that small metal filings when exposed to an electromagnetic field will cling together or cohere and conduct electricity. These detectors would be used as a switch in a DC circuit, allowing current to flow when electromagnetic waves were incident upon the coherer.

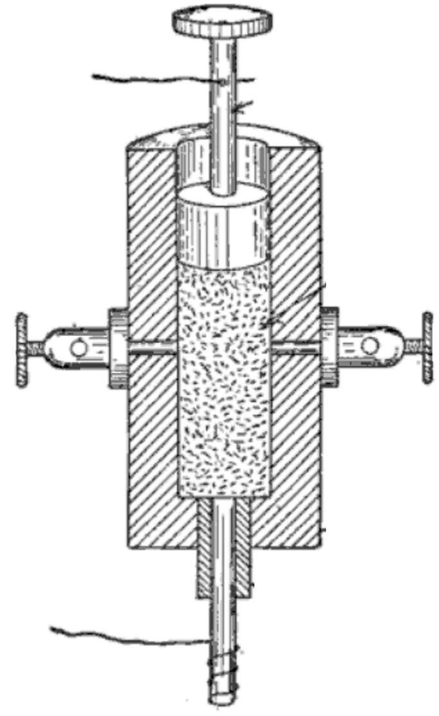

Figure 4. A cross sectional drawing of a Branly coherer showing the metal filing within the chamber and electrical connections at either end.

Lodge's lecture was very well received and spurred on a considerable amount of development in the field of electromagnetic research. Jagadish Chandra Bose, inspired by the publication of Lodge's lecture, began his own study on the quasi-optical nature of higher frequency electromagnetic radiation. In 1894, Bose constructed and tuned his own spark gap transmitter (pictured in Figure 5) which emitted radiation at approximately 60 GHz.

Figure 5. A photograph of Bose's 60 GHz emitter and receiver at the Jagadish Chandra Bose Museum in Kolkata [25].

Bose’s work resulted in the development of waveguides, horn antennas, dielectric lenses, and a new form of detector which relied on the resistance drop of a galena (lead sulfide) crystal when exposed to electromagnetic radiation. In his experiments, Bose collected and concentrated the electromagnetic radiation onto a galena crystal using a horn antenna. By passing a current through the crystal and carefully monitoring its change, Bose was able to measure the strength of his waves, this marked the first practical application of a semiconductor. After a year of work, Bose demonstrated his findings at the town hall of Kolkata where he touched upon some the most important properties of the millimeter waves that he was generating. Bose showed that these waves can travel through human bodies, walls, and over long distances, he also showed that these waves had practical applications, using them to trigger circuits which rang bells and ignited gunpowder [26]. These demonstrations coupled with work being performed concurrently by Guglielmo Marconi convinced the wider world of the practical applications of electromagnetic waves for long distance communication.

2.2.1.2 Development of Continuous Wave Systems

Work done by Marconi resulted in the development of long-distance wireless telegraphy which revolutionized long distance communication. With the first wireless telegraphy company being formed by Marconi in 1897. These systems made use of very large spark gap transmitters operating between 15 kHz and 2 MHz and with powers ranging from 0.25 kW up to 500 kW. While these systems allowed for signals to be sent over hundreds of kilometers using systems such as Morse code, they produced damped electromagnetic waves which smeared their power over a large bandwidth. This broad emission of frequencies invariably led to transmitting stations interfering with each other and prevented complex signals such as voice to be encoded on the waves. As early as 1892 physicists such as George Fitzgerald Francis knew that a continuous wave (CW) transmitter producing a sine wave of a pure frequency would be of more use. Francis attempted to realize such a transmitter but was unsuccessful [27].

The development of a suitable CW source took two separate paths and resulted in two distinct transmitter types, the arc converter, and the Alexanderson alternator. The arc converter made use of a spark which was produced by an alternating current and produced CW signals in the kilohertz range as well as quite a few harmonics. The Alexanderson alternator, which was first constructed by Reginald Fessenden, was essentially an AC electrical generator designed to work at radio frequency (pictured in Figure 6). The frequency generated by the alternator could be tuned by changing the rotation speed. This current was passed through an amplifier circuit which allowed for the waves to be encoded with complex signals such as the human voice, with the first radio transmission of a human voice taking place on Christmas Eve 1906 by Fessenden using an Alexanderson alternator operating at 100 kHz [28]. The key drawbacks of these systems were their bulk and complexity which made them impractical for many applications. The concepts developed in these early years set the stage for even further development of solid-state systems.

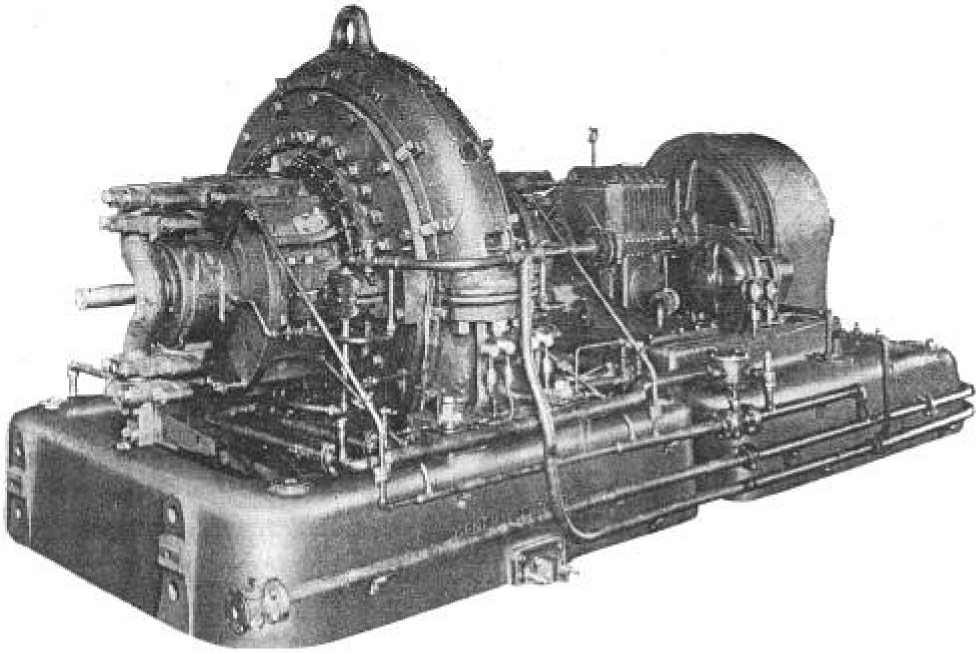

Figure 6. A photo of an Alexanderson alternator designed to operate at 200 kW and installed at the New Brunswick, New Jersey Naval station [28].

Throughout the development of these early CW transmitters, receivers also saw advancement beyond the initial coherer which proved unreliable. In 1902 Marconi introduced his magnetic detector which detected radio waves by first coupling an antenna to a coil of thin wire which was placed in a magnetic field, a continuous loop of iron was passed through the coil and then through a separate detector coil. When a radio wave excited the first coil, the hysteresis of the iron caused a pulse of current to be induced in the sensor coil [29]. This current pulse could be translated to an audio pulse and used as a Morse code signaling system.

In 1903 Fessenden invented his electrolytic detector which used thin silver-plated platinum wire enclosed in a glass rod, and the tip of the wire was immersed in an electrolyte solution such as nitric acid. The electrolyte solution was held inside a platinum cup which was connected to ground and acted as an anode while the wire was positively biased. The bias across the solution causes the solution to break down via electrolysis which causes insulating bubbles to form on the wire. These bubbles function as a gate which only allows radio frequency (RF) signals to pass from the wire to the cup and into the circuit. This detector also functioned as an amplitude modulated (AM) demodulator, rectifying AM signals and effectively decoding them.

In 1904 John Ambrose Fleming invented the first vacuum tube which consisted of hot wire filament cathode and a metal plate acting as an anode, these were placed in a glass tube which was evacuated of air and sealed. The cathode was able to pass electrons to the anode through thermionic emission, but electrons could not travel the other way as the anode was unheated. These diode "valves" rectified the oscillating AM radio signal into a DC voltage varying signal. Building upon Fleming's work, Lee de Forest added a wire grid between the cathode and anode creating the triode tube. The grid in the triode could be used to control current flow from the cathode, this control also allowed for effective voltage and power amplification. These tubes found much use as both RF emitters and detectors, although their emissions were limited to the high frequency band.

Initially started to circumvent de Forest's patents, Albert Wallace Hull began experimenting with using an external magnetic field to control current flow in a diode vacuum tube. The application of the magnetic field deflected the electrons flowing from the cathode at a right angle to the field. Crucially, Hull found that there existed a field strength, called the Hull cut-off magnetic field, where the electrons are deflected such that they just reach the anode [30]. At this critical field strength, some of the electrons miss the anode and remain to circle around the tube, these circling electrons emit electromagnetic radiation in the microwave band due to cyclotron radiation. Noticing this phenomenon Hull went on to invent the Hull magnetron which was only tube-based source to emit high power in the centimeter range.

2.2.1.3 Solid-State Systems

To support the development of sonar in World War I, Paul Langevin sought to apply the piezoelectric effect to create a quartz crystal oscillator. These initial efforts were unsuccessful but in 1917 Alexander Nicholson built the first crystal oscillator out of Rochelle Salt [31]. Development progressed with quartz and three years later, Walter Guyton Cady produced the first quartz oscillator at Bell Telephone Laboratories [32]. These oscillators use piezoelectric crystals which deform when exposed to an electric field and generate an electric field when they return to their original shape. This allows the crystals to function as an RLC circuit with a precise resonant frequency. Crystal oscillators can be produced with resonant frequencies from 10 kHz to around 100 MHz [33], this range can be extended through the use of frequency multipliers or dividers.

To provide greater stability to the resonant frequency of the crystal oscillators which can change with the ambient temperature, the oscillators can be placed into an oven which maintains the oscillator at a constant temperature. These crystal oven oscillators are able to achieve very low frequency uncertainties, with the 1929 US frequency standard being a group of 100 kHz crystal ovens operating with a frequency uncertainty of 10^{-7} Hz [34].

There is some uncertainty about exactly when the first resonant cavity magnetron (RCM) was invented, with the earliest possible device coming from the work of K. Okabe in Japan in 1929 [35]. Regardless, the RCM was a significant improvement over the Hull magnetron as it did away with the need to use a fragile vacuum tube. The device worked by placing a cathode within a specially shaped anode, as seen in Figure 7. The slots in the anode function as conductors while the cylindrical holes, called resonating cavities, function as inductors. This makes the system act as a solid-state LC circuit whose resonant frequency is set by its physical dimensions. To couple the radiation out of the RCM into a coaxial cable, a "tap" wire can be placed in one of the resonating cavities, the radiation may also be coupled into a waveguide by connecting it to a resonant cavity. RCMs act as great sources for high power electromagnetic radiation, with peak powers as high as 2.5 megawatts [36], and with frequencies as high as 95 GHz [37].

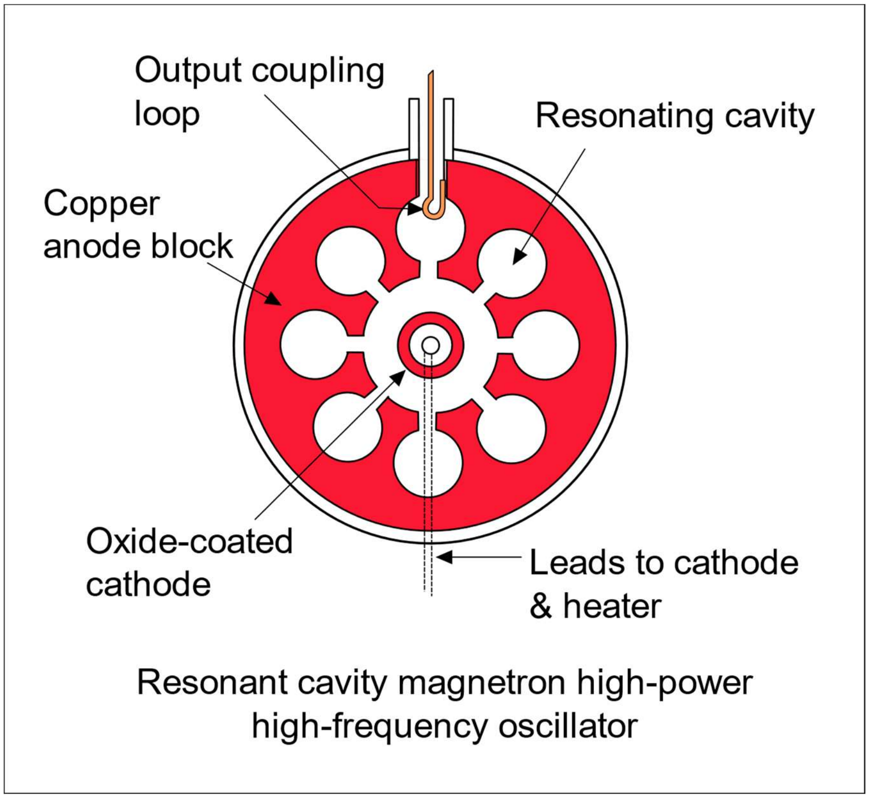

Figure 7. A labeled diagram of a cavity magnetron, sourced from [38].

Desiring a device with similar operating qualities as the RCM but with the ability to tune the output frequency during operation, Bernard Epsztein created the M-type backward wave oscillator (BWO) in 1951 [39] and improved upon by Rudolf Kompfner with the O-type BWO

[40]. The basic structure of the BWO, as seen in Figure 8, consists of a travelling wave tube through which a source RF signal travels, through the center of the travelling wave tube, an electron beam is directed. The electron beam is significantly stronger than the RF signal and its interactions with the RF signal results in the electron beam being an amplified version of the wave in the tube.

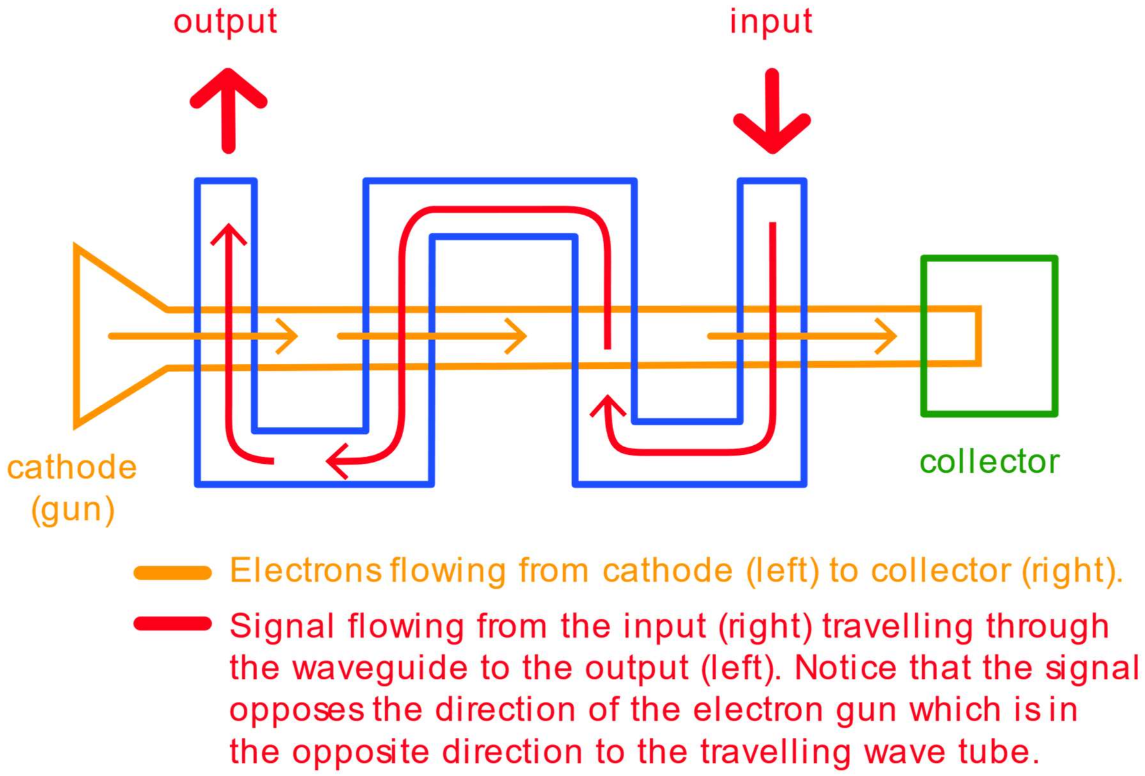

Figure 8. Basic annotated block diagram of a backward wave oscillator showing the general function of the device. Sourced from [41].

In the typical helical design, the amplified signal is extracted from the BWO along the length of the oscillator with a conductor. The BWO allows for the generation of frequencies over wide bandwidths with devices operating from 100 MHz out to 1.4 THz with high stability and appreciable power in the range of 10s of milliwatts [42].

The development of semiconductor diodes in the mid-1930s allowed not only for the replacement of vacuum tube-based diodes in most systems, but also the creation of novel sources and detectors based on these devices. The Gunn diode is one such device which is based on the Gunn effect first documented by Jo Be Gunn in 1962 [43]. This effect is present in certain semiconducting materials such as gallium arsenide and gallium nitride whose electronic band structure contains sub bands in addition to the valence and conduction bands. When biased with a suitable voltage, electrons can populate these higher sub bands, with a high enough voltage many electrons can populate these bands which causes them to slow down and thus reduces the current flowing through the crystal. This all results in a negative differential resistance. Gunn diodes made from gallium arsenide and gallium nitride consist of three layers of N-doped material, a lightly N-doped region sandwiched between two heavily N-doped regions. The diode is biased into its negative resistance region and when coupled with a load circuit, results in a circuit with zero differential resistance which will produce spontaneous oscillations whose frequencies are determined by the structure of the center N-doped region. Gunn diodes can be used to generate oscillations from 200 GHz out to around 3 THz with powers on the order of 100 mW [44].

Semiconductor diodes have also been used as a method to detect and rectify electromagnetic radiation. Chiefly the Schottky diode, named for German physicist Walter Schottky, has been used in detectors functioning from hundreds of kilohertz out to 1.7 THz and beyond [45]. The basic structure of a Schottky diode as N-type semiconductor in contact with a conductive metal plate and its key feature is its remarkably fast reverse recovery time which can be less than 100 ns in the case of fast detectors [46].

Initially in the absence of detectors fast enough for THz applications, cooled bolometers were used as power detectors. These devices consist of materials with temperature dependent resistivities which heat up when electromagnetic radiation is incident upon them [47]. These detectors can be made to be quite sensitive to power variations and work over very wide bandwidths. The key drawbacks of the bolometer are that they require an amplitude varying signal and operate at cryogenic temperatures, limiting their application outside of the lab.

2.2.1.4 Optical methods

In recent years, methods to generate frequencies in the THz range have been developed using optical methods. These methods include gas lasers which excite rotational states of certain molecules which in turn generate THz radiation [48], and optical rectification in nonlinear crystals and gases which converts ultrafast laser pulses to high frequency electromagnetic radiation [49, 50].

Optically based detection methods have also been developed, chiefly the photoconductive antenna. A photoconductive antenna consists of a photoconductive crystal, typically gallium arsenide, with two gapped metallic strips placed across it acting as a dipole antenna. When an ultrafast laser pulse is directed into the gap between the strips, the device becomes sensitive to high frequency photocurrents, which results in a voltage across the two strips. However, if a dc bias is setup across the strips and an ultrafast laser pulse is directed into the gap, the device will actually create high frequency photocurrents and couple them out of the crystal [51].

2.3 TERAHERTZ FOR MATERIALS INSPECTION

With advent of stable sources and detectors operating in the THz regime, it has been utilized as a materials inspection tool in a wide variety of applications from art restoration, defense and security, biology and health, and many more [52-56]. As a sensor methodology, THz sensors are compatible with many different materials with good penetration into non-conductive non-polarizable dielectrics as well as access to resonances of many gases. The theory behind this application is that as an electromagnetic wave passes through a medium, it interacts with the molecular structure of the medium and depending on the material and its geometry, the traveling electromagnetic wave is distorted and scattered in a predictable way. The influence on the terahertz beam from the medium is due to the electromagnetic wave interacting with molecules of the medium or with the bulk physical structure. In the millimeter wave/THz bandwidth, from 0.03 THz to 10 THz, these excitations are molecular rotations in gases, lower frequency bond vibrations, crystalline phonon vibrations in some solids, and hydrogen-bonding stretches and torsions in gases and liquids [57]. In the case of bulk, polarizable materials like liquid water, the wave creates a polarized electric field that all the polar molecules move to align themselves with. When measured, the strength of these effects in a material are called the dielectric constant or relative permittivity of a material ε_r. ε_r is dependent on frequency ω, dimensionless, and complex with its form shown in equation (4).

$$\varepsilon_r = \varepsilon_r' + \varepsilon_r'' \tag{4}$$

This can be expressed in terms of the more familiar quantities, extinction k coefficient, and refractive index n as:

$$\varepsilon_r' + \varepsilon_r'' = (n + ik)^2 = (n^2 - k^2) + i(2nk) \tag{5}$$

Here the extinction coefficient k can be expressed in terms of the absorption coefficient α and the frequency ω and speed of light c as.

$$k = \frac{c}{4\pi\omega}\alpha$$

(6)

Now solving for the index of refraction n and the extinction coefficient k in terms of ε_r' and ε_r'' we get equations (7) and (8).

$$n = \sqrt{\varepsilon_r' + k^2} = \sqrt{\frac{1}{2}(\varepsilon_r' + (\varepsilon_r'^2 + \varepsilon_r''^2)^{1/2}}$$

(7)

$$k = \frac{\varepsilon_r''}{2n}$$

(8)

Lastly, we can write the ratio of ε_r' and ε_r'' in terms of n and k as seen in equation (9).

$$\frac{\varepsilon_r''}{\varepsilon_r'} = \frac{2nk}{n^2 - k^2}$$

(9)

The components of the relative permittivity are not directly measured, but their effects on a travelling wave are. From these effects we can calculate ε_r' and ε_r'', this is the basis of spectroscopy. When a travelling wave passes through a sample, four things can happen to it. Its power may be reflected by the interface between the medium it was travelling in before the sample (we will assume air as this is typically the case) and the sample or the interface between the sample and the travelling medium. Its power may be scattered due to the coarse structure of the sample. Its power may be absorbed by the material in the sample through mechanisms described earlier. Finally, the passage of the wave through the sample may be sped up or slowed down depending on the ratios of the refractive index of the sample and the travelling medium.

Using a spectrometer, intensity or electric field and phase measurements of the wave travelling through only the medium and the medium and the sample, allow for these four effects to be quantified. Depending on the optical set up of the spectrometer these effects will present slightly differently. Only free-space spectrometers are relevant to this work, as such only free-space designs will be discussed.

In transmission mode the system is designed to pass the THz beam through the sample at one end and read the wave which passes through the other. The loss in power between the reference and sample measurements, $\Delta I = I_{ref} - I_{samp}$, is a convolution of reflected, scattered, and absorbed power. This convolution can be seen in Figure 9, it is also described by equation (10).

$$I_T = I_0 - (I_R + I_{S1} + I_{S2} + I_A) \tag{10}$$

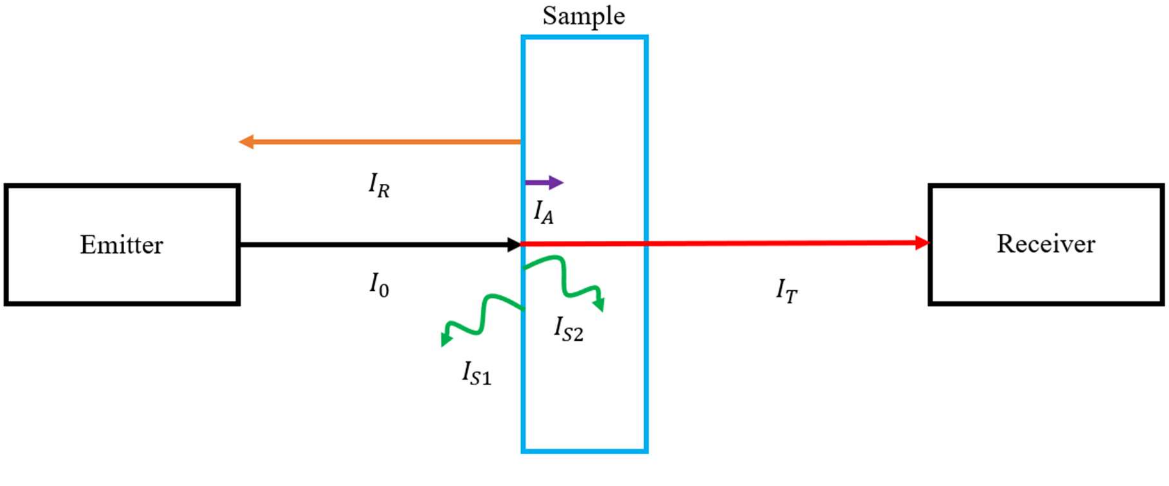

Figure 9. A basic block diagram of a transmission mode spectrometer showing the various methods of power loss in the incident wave I_0 when transmitting through a sample. Assuming a sufficiently absorbing sample such that higher orders of power can be neglected.

This convolution of loss factors can make it difficult to quantify the desired quantity α which is only a factor of I_A. However, if the reflectivity of a sample is known and its scattering is either negligible or consistent, the I_A term can be teased out. From this I_A term, we can calculate α using the beer lambert law shown in equation (11).

$$I_A = I_0 * e^{-\alpha * d} \tag{11}$$

This can be arranged to directly give α as shown in equation (12).

$$\alpha = \frac{\ln\left(\frac{I_0}{I_A}\right)}{d} \tag{12}$$

The wave will be slowed by the index of refraction of the sample, the magnitude of this slowing is shown in equation (13) where ν is the velocity of the wave in the sample, and c is the speed of light in a vacuum.

$$v = \frac{c}{n} \tag{13}$$

This change in velocity results in an overall phase shift at the detector. This is due to the wave taking longer to travel the optical path of the system. Even though the space between the emitter and receiver did not change, the addition of the sample with a higher index of refraction changes the optical path length. The change in time it takes the beam to pass through the system with and without a sample are shown in equations (14) and (15) where n_1 is the index of the travelling medium (for free space spectrometers this is typically air) n_2 is the index of the sample, "PL" is the optical path length of the spectrometer, and *d* is the thickness of the sample.

$$t_{ref} = \left(\frac{c}{n_1}\right)/"PL"$$

(14)

$$t_{samp} = \left(\frac{c}{n_2}\right)/d$$

(15)

Subtracting t_{ref} from t_{samp} gives a time delay Δt which can be related to the phase shift θ using equation (16) where ω is the frequency of the wave.

$$\theta = 2\pi * \omega * \Delta t$$

(16)

In reflection mode the system is designed to pass the THz beam through the sample once, reflect off some highly reflective surface, and pass back through the sample and into the detector (Figure 10). In reflection mode, if the THz beam is perpendicular to the front face of the sample, the loss in power due to absorption in the sample can be masked by the power reflecting off the top surface of the sample. With the power at the detector I_{T2} with respect to the incident power I_0 shown in equation (17), this equation assumes that the sample is sufficiently absorbing such that higher orders of reflection, absorption, and scattering, are small enough such that they can be ignored.

$$I_{T2} = I_0 - (I_{S1} + I_{S2} + I_{A1} + I_{A2} + I_{R2} - I_{R1})$$

(17)

Here we can reduce the term $I_{A1} + I_{A2}$ to the simpler $2I_{A1}$ since the absorbance is constant.

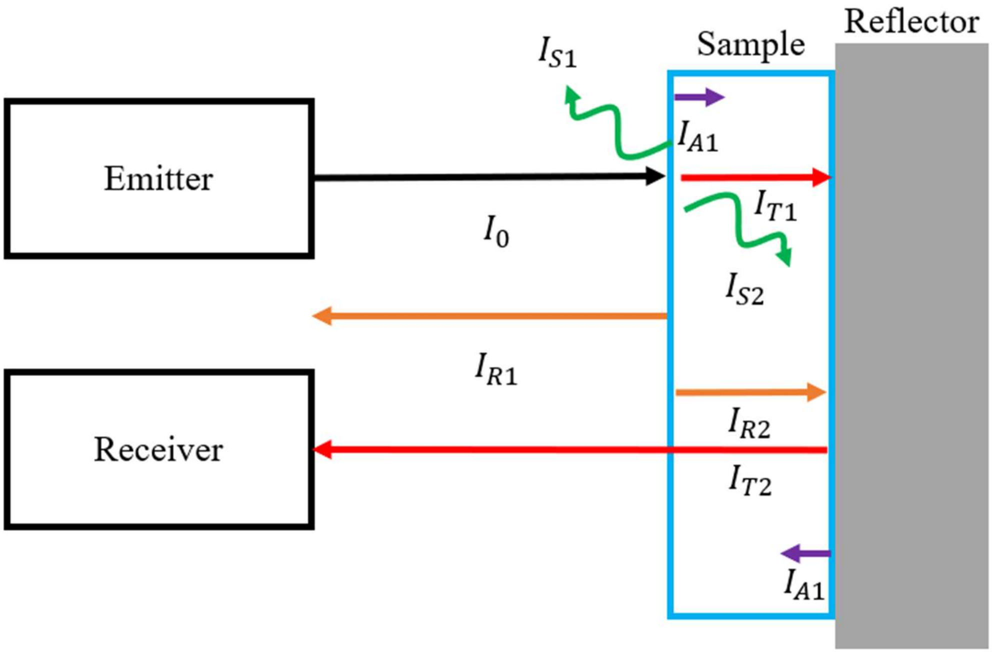

Figure 10. A basic block diagram of a reflection mode spectrometer showing the various methods of power loss in the incident wave I_0 when transmitting through a sample. Assuming a sufficiently absorbing sample such that higher orders of power can be neglected.

Now as with the transmission mode system, extracting the $2I_{A1}$ term from measurements can be quite complicated but some tricks exist to help with this. If a sample's reflectance is known beforehand, it can be subtracted out directly. Samples can also be engineered to produce little to no top surface reflectance over the measurement bandwidth, allowing the I_{Rn} terms to be ignored. If the emitter and receiver are placed such that the THz beam is not perpendicular to the top surface, I_{R1} will refract out of the detection path and will appear as a loss instead. Finally, if a time domain spectrometer is designed with fine enough time sensitivity such that time resolution is much greater than the time delay caused by the beam transiting the sample, the signal from I_{R1} will show up earlier in time than I_{T2} and can be separated easily.

The time delay or phase shift of the measured wave in reflection mode is similar to the case of transmission mode operation with a few key differences. Since the wave is reflected, both off the top surface of the sample in the case of I_{R1} and off the reflector in the case of I_{T2}, it is shifted in phase by π from the phase of the incident wave. This phase shift occurs in both the reference measurement and the sample measurement. Equation (15) also undergoes a modification to become equation (18). This modification is due to the wave passing through the sample twice.

$$t_{samp} = \left(\frac{c}{n_2}\right)/2d \tag{18}$$

Operating in this mode can be far more difficult and require more expensive components than operating in transmission mode but it also offers some key benefits. With their emitter and receiver being coplanar, reflection mode systems are often more compact. They offer the ability to do so called “standoff” measurements which is often key when designing sensors to be used outside of the lab. Reflection mode spectrometers are also quite useful when working with thin samples or samples with low absorption, the two passes that the wave makes through the sample effectively doubles the sample’s thickness and increases measurement sensitivity.

The preceding discussion was meant to present and discuss THz spectroscopy in general cases. As such, some nuances have been omitted. Chiefly the effects of multiple reflections within a sample were ignored. If a sample is sufficiently thick and has flat and smooth sides, the sample can act as a Fabry-Pérot cavity. This will result in patterns of constructive and destructive interference. Strong effects from this phenomenon are rare in samples which are not engineered to act as Fabry-Pérot cavities which is why the intricacies of this interaction are not included here.

There are two distinct methods by which THz can be used to inspect and characterize samples, these are continuous wave (CW) THz spectroscopy and THz time-domain spectroscopy (TDS). In this section these two methods will be introduced and discussed.

2.3.1 Continuous-Wave Terahertz Spectroscopy

CW THz spectroscopy is akin to other CW spectroscopy methods but uses frequencies in the millimeter wave/THz range (0.03 THz – 10 THz). Sources for CW THz spectroscopy must have good long-term power and frequency stability in order to provide accurate frequency dependent material property measurements. CW THz spectroscopy systems consist of a THz source and detector coupled with some form of optical system. This optical system can be set up in either transmission or reflection mode as discussed above. Within this optical system, devices such as optical choppers, delay lines, phase stretchers, and raster scanning imaging systems can be included. Depending on the measurements to be done, a spectrometer can be built to measure power or power and phase information.

By simply monitoring the power on the detector and comparing the change in power with and without a sample in the optical path, measurements of a sample's transmittance $T(\omega)$, can be made. These transmittance measurements combine the reflection, scattering, and absorbing interactions in the sample into a generalized attenuation coefficient $AT(\omega)$ and the transmittance can be modeled using the Beer-Lambert law (equation (19)) where $I_0(\omega)$ is the intensity measured when no sample was in the optical path (sometimes called the reference measurement) $I(\omega)$ is the intensity measured when the sample was present in the optical path, and d is the thickness of the sample.

$$I(\omega) = I_0(\omega) * e^{-AT(\omega)*d}$$

(19)

Transmittance measuring systems can be suitable for THz CW imaging, non-destructive characterization, and detection. This can also be useful when the absorbance is much greater than the scattering or reflection due to a sample and the cost of the spectrometer is a concern.

Transmittance spectrometers are the cheapest and easiest setups to construct but their phase insensitivity prevents the measurement of more fundamental material properties such as index of refraction n and absorption coefficient α. When measurements of these parameters are needed, such as in the case of novel materials characterization [58], non-contact thickness measurements [59], and even moisture content detection [60, 61]. To construct a phase sensitive CW THz spectrometer, the phase stability of the emitter must first be considered as any uncertainty here will propagate through all measurements and impact the performance of the system. Next a method of phase sensitive detection (PSD) must be chosen. The three main methods of PSD are lock-in amplification, frequency mixing, and optical beat monitoring. These methods are discussed below.

2.3.1.1 Lock-In Amplifier Phase Detection

Lock-in amplification is the most versatile of the three methods, able to be used with all methods of emission and detection. Lock-in amplifiers rely on the THz radiation to be time varying in either intensity or frequency in a known way. The signal by which the signal varies, referred to as either the local oscillator (LO) or external reference frequency, which is typically either a square or sine wave is fed into the amplifier. The amplifier then generates two of its own reference signals called the *I* and *Q* references, which match the frequency of the external reference (Figure 11) and take the form of a sine wave. The *I* reference is a sine wave which has the same frequency and a fixed phase shift from the reference signal and has the general form $\sin(\omega_{ref}t + \theta_{ref})$ where $\omega_{ref} = 2\pi f_{ref}$. The Q reference, called the quadrature signal is phase shifted 90º from the I signal and has the form $\sin(\omega_{ref}t + \theta_{ref} + 90)$.

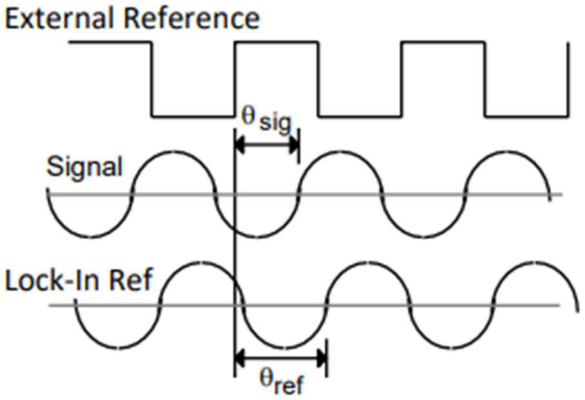

Figure 11. A basic diagram showing the external reference, signal, and lock-in reference used in the lock-in amplification method of phase sensitive detection. In this case the lock-in reference is the *I* or in phase reference Sourced from [62].

By multiplying the signal from the detector with voltage V_{sig} with the I signal we get V_I seen in equation, and by multiplying the detector signal with the Q signal we get V_Q seen in equation.

$$V_I = \frac{1}{2}V_{sig}\cos(\theta_{sig} - \theta_{ref}) \tag{20}$$

$$V_Q = \frac{1}{2}V_{sig}\sin(\theta_{sig} - \theta_{ref}) \tag{21}$$

These two signals are proportional to cosine and sine respectively and can be simplified and rewritten as the terms *X* and *Y* (equations (*22*) and (*23*)).

$$X = V_{sig}\cos\theta \tag{22}$$

$$Y = V_{sig} \sin\theta$$

(23)

These two terms represent the signal from the detector as a vector relative to the lock-in's reference oscillator and we can calculate the magnitude R and phase θ of the signal vector accordingly.

$$R = (X^2 + Y^2)^{1/2}$$

(24)

$$\theta = \tan^{-1}(Y/X)$$

(25)

While this method does give phase information, it is not the phase of the electromagnetic wave itself, but the phase of the amplitude modulated signal. This does result in this method being useful for measuring the amplitude of an electromagnetic wave, systems that use this method are typically prone to interference from standing waves.

2.3.1.2 Frequency Mixing Method

The frequency mixing method makes use of devices called frequency mixers which are precisely made arrays of diodes. This method is only compatible with frequency modulated continuous-wave (FMCW) systems as it requires a varying frequency. In an FMCW system, the source is swept in frequency with a known bandwidth B, repetition rate τ (Hz), and waveform. The power from the source is split between the emitter and the local oscillator (LO) port of the mixer, the power from the detector is fed into the radio frequency (RF) port of the mixer, and the resultant frequency is read from the intermediate frequency (IF) port of the mixer.

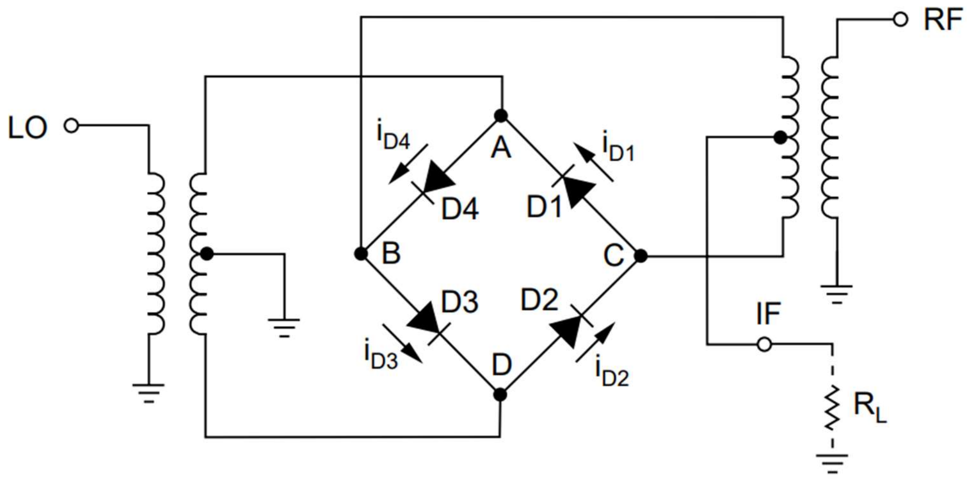

Figure 12. A simple circuit diagram of a double balanced four diode ring mixer from [63].

During operation, the signals on the on the LO and RF ports of the mixer are combined and at the IF port a signal made up of a combination of numerous signals with frequency f_{IF} described in equation (26).

$$f_{IF} = |f_{LO} \pm f_{RF}| + f_{LO} + f_{RF} \tag{26}$$

Although not described in equation (26), f_{IF} also contains harmonics of the term $|f_{LO} \pm f_{RF}|$ i.e. components with the frequency $|f_{LO} \pm m * f_{RF}|$ where m is any integer. These components are typically ignored as with each increase in m the power of the signal at that frequency falls off. When coupled with a suitable bandpass filter we can reduce the IF output to the pure difference frequency in equation (27), this is called down conversion. The time dependence of f_{LO} andf_{RF} come from the frequency sweeping of the source.

$$f_{IF} = |f_{LO}(t) - f_{RF}(t)| \tag{27}$$

With a down converting mixer, we can sense the phase of the CW THz in our system by comparing f_{IF} when the optical path is empty f_{ref} and when our sample of interest is placed in the optical path f_{samp}. If we consider $f_{LO}(t)$ and $f_{RF}(t)$ as they change with time at mixer, we can see how we can measure phase. Here we consider the most common case where the frequency of the source varies as a sawtooth wave, and we assume that the repetition rate τ is slow enough such that the signal at the LO and RF port are within one period of each other $(0 < t < \tau)$. When the path is empty, we get equations (28) and (29) where B_0 is the starting frequency of the source, L is the optical path length, and c is the speed of light. An illustration of the frequency vs time at both the LO and RF ports is seen in Figure 13.

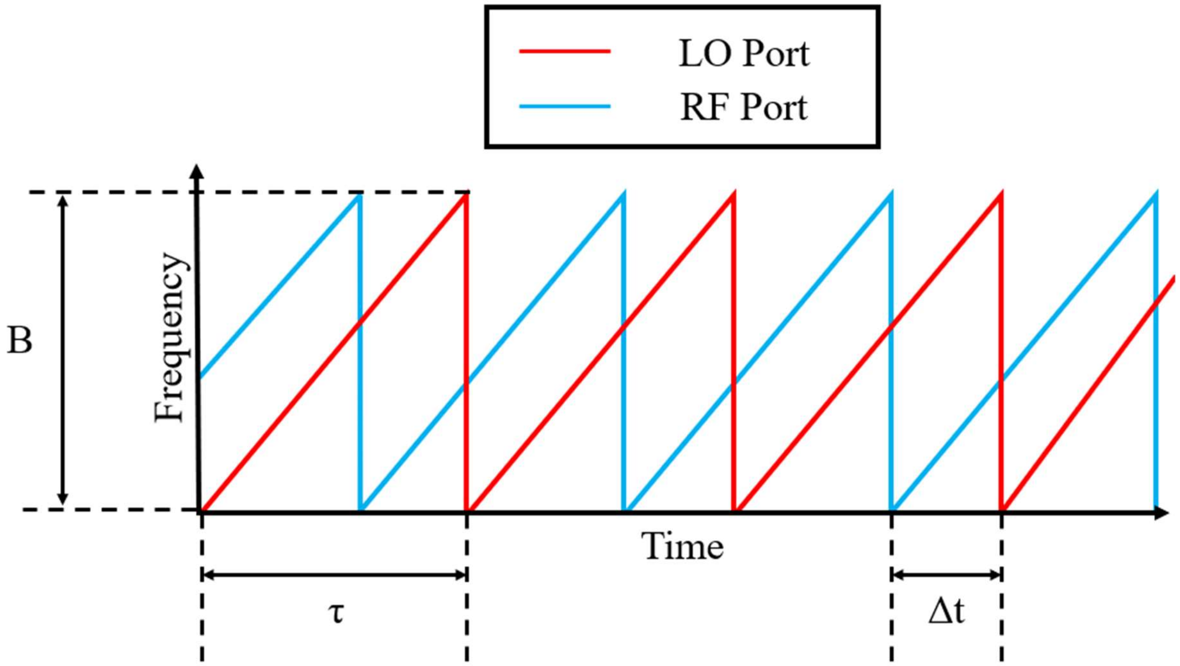

Figure 13. Plot of frequency vs time at the RF and LO port of a mixer used as a phase sensitive detector in an FMCW system sweeping frequency as a sawtooth.

$$f_{LO}(t) = B_0 + \frac{t}{\tau} * B$$

(28)

$$f_{RF}(t) = B_0 + \frac{\left(t - \frac{L}{c}\right)}{\tau} * B$$

(29)

Here we see in equation (29) that f_{RF} lags in frequency by a set time $\frac{L}{c}$, this is what makes f_{ref} a constant frequency $\left(\frac{t}{\tau} * B\right) - \left(\frac{(t-L/c)}{\tau} * B\right)$. When our sample is placed in the path f_{LO} stays the same but f_{RF} becomes equation (30).

$$f_{RF}(t) = B_0 + \frac{\left(t - \frac{L}{c} - t_s\right)}{\tau} * B$$

(30)

Here t_s is the additional time delay introduced by our sample. By comparing f_{ref} and f_{samp} we get a frequency difference which corresponds to a time difference caused by the term t_s, the additional time taken to transit the sample, Δt. This Δt can be used to calculate phase θ using equation (31).

$$\theta = 2\pi * \tau * \Delta t$$

(31)

If the index of refraction *n* does not significantly vary over *B*, this phase θ is constant over *B*. If this is not the case, the sawtooth at the RF port would become distorted as different frequencies would be phase shifted to different degrees and θ must be measured at every frequency.

The frequency mixing method has the benefit of making it easy to integrate into small footprint sensors that operate at low powers. It is also a cheaper solution than the lock-in method with a mixer operating at 67 GHz costing under $300. The limitations of this method are that it requires the system to be operated in FMCW mode and that suitable mixers operating in the THz bandwidth are rare and typically operate at cryogenic temperatures.

2.3.1.3 Optical Beat Monitoring Method

The optical beat monitoring method is used in systems that generate and detect CW THz using the optical method covered earlier. These systems measure THz intensity at the detector by mixing the photocurrent created at the detector by the incident THz wave with an optical beat frequency. This method is well described in Roggenbuck et.al. [64]. Due to this method's lack of relevance to the work discussed here, only a very brief summary of that description is presented here.

Measurements of photocurrent I_{PH} from optical systems depend on the THz electric field E_{THz} at the detector and on the phase difference $\Delta\theta$ between the THz field and the laser beat at the detector. Which gives rise to the relation in equation (32).

$$I_{PH} \propto E_{THz} \cos(\Delta\theta) = E_{THz} \cos(2\pi\, \Delta L\, \omega/c) \tag{32}$$

Here ω is the frequency of the THz beam, c is the speed of light, and ΔL is the difference in optical path between the laser beat to the detector L_D and the optical path travelled by the laser beat to the emitter L_S and the path of the THz beam from the emitter to the receiver L_{THz}, seen in equation (33)

$$\Delta L = (L_S + L_{THz}) - L_D$$

(33)

When the frequency of the THz beam is swept linearly, an interference pattern is generated in the form of a cosine wave. The spacing of the maxima of the interference pattern of the reference measurement are equally spaced in frequency with locations of maxima of order m given in equation (34).

$$\omega_{max,m}^{ref} = m \frac{c}{\Delta L^{ref}}$$

(34)

When passing through a sample of thickness *d* the optical path length of the THz beam is increased by $(n_{samp} - n_{air})d$, and thus the maxima shift. By comparing the interference pattern of the system during a reference measurement to the pattern when a sample is measured, the shift in maxima at a given frequency ω corresponds to a phase shift induced by the sample.

Since the phase shift can be evaluated at the minima, maxima, or zero crossing point of the interference pattern, this method gives a frequency resolution of the phase of ¼ the period of the pattern. More precisely the phase resolution is proportional to $c/(4 * \Delta L)$. This means that phase resolution can be improved by varying the optical path difference.

2.3.2 Time Domain Terahertz Spectroscopy

THz time domain spectroscopy (TDS), which uses ultrafast pulses of broadband THz radiation to probe samples, was first proposed in the mid-1980s by DH Auston and colleagues [65]. It took a further 5 years of development before Van Exter and colleagues demonstrated a working system [17, 66]. These systems are based on optical generation and detection methods of THz and work by shorting a charged dipole antenna with sub-picosecond pulses of laser light, a diagram of such a dipole is seen in Figure 14. The shorting of this biased dipole results in burst of broadband THz radiation lasting multiple picoseconds with time varying amplitude.

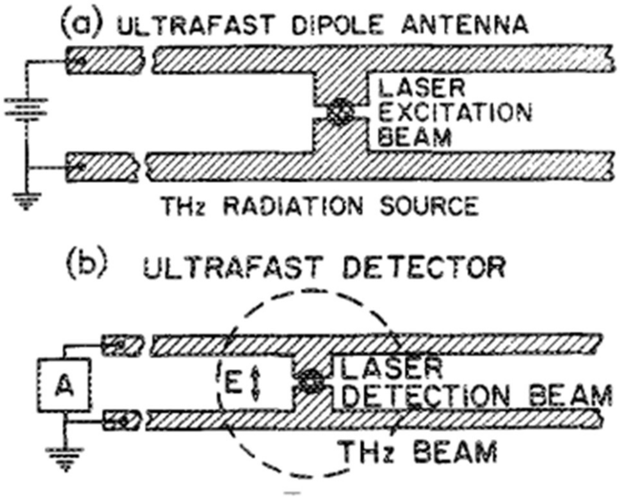

Figure 14. Diagrams of the THz emitter (a) and detector (b) used in THz TDS. In the emitter (a) the dipole is electrically biased and the ultrafast laser pulse in the gap of the dipole shorts it out and generates and accelerates photocurrents lasting multiple picoseconds. In the detector (b) the current across the dipole is monitored and ultrafast laser pulse in the gap makes the dipole sensitive to photocurrents which are induced by incident THz radiation.

The time varying THz signal is propagated through an optical path much like in the CW method and the signal strength and phase is measured at the detector. On the detector, the time since pulse was emitted is monitored and the received pulse is given in units of photocurrent in nanoamps versus time since emission in picoseconds. For the detector to be made sensitive to a THz electric field, the same pump signal must be sent to the dipole gap at the detector. To ensure the arrival of the pulse is in time with the arrival of the THz signal, a delay stage is used. This delay stage adds additional optical path length into the detection arm of the spectrometer. A diagram of a typical THz TDS system can be seen in Figure 15.

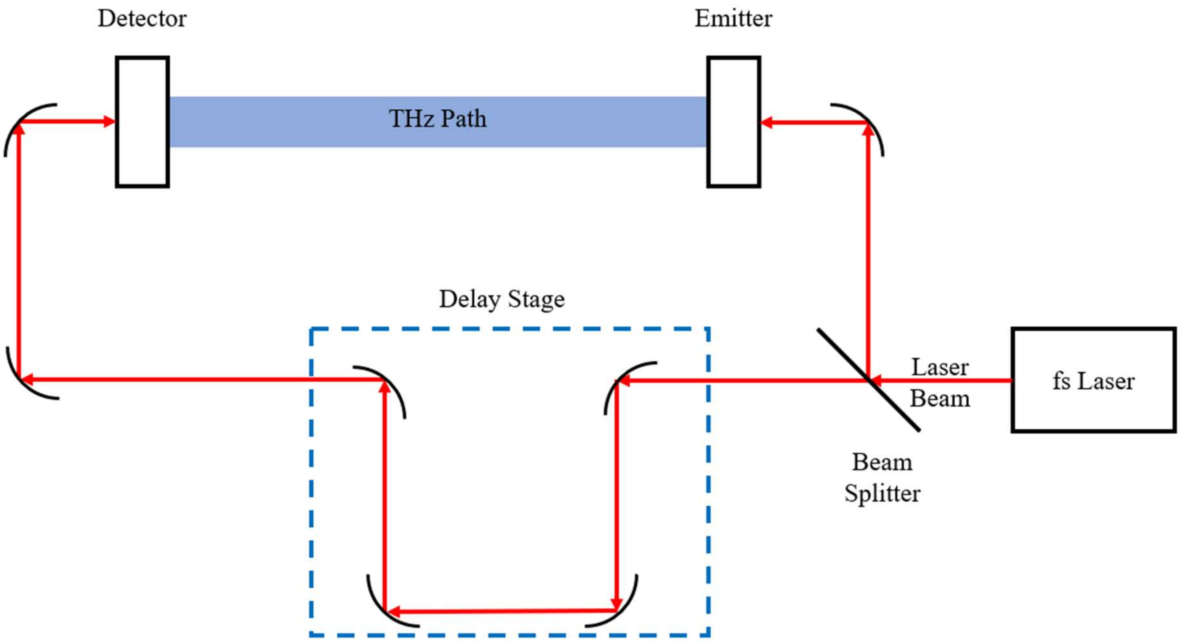

Figure 15. A simplified block diagram showing the optical paths used in a THz time-domain spectrometer.

The measurement of the empty optical path is again called the reference measurement and sets a baseline for time delay and signal absorption. When a sample is measured, the pulse is delayed and broadened, and its peak-to-peak amplitude is lessened as its energy is absorbed. For sample measurement the pulse's delay is measured in delay with respect to the reference pulse. These effects can be seen in Figure 16

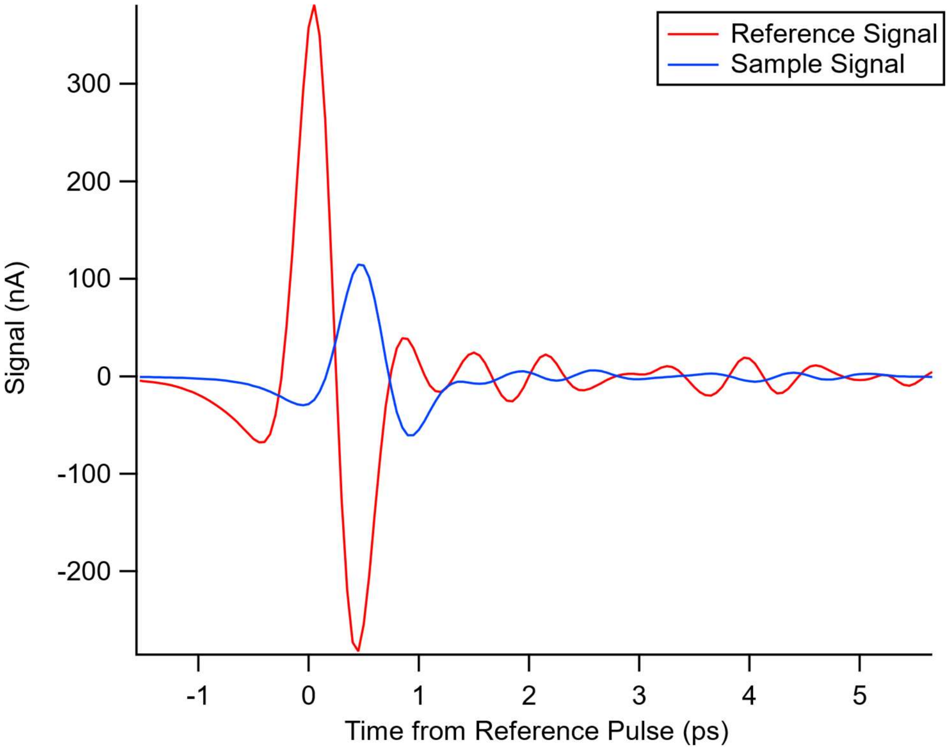

Figure 16. A graph of the time domain signal strength in a THz TDS system with the reference pulse in red and a sample pulse in blue. Time is given in time from reference pulse showing a 0.5 ps delay in the sample. Signal strength is in nanoamps showing a reduction in peak-to-peak amplitude of over 350 nanoamps in the sample.

These time varying signals measured in THz TDS contain frequency components over an extremely wide bandwidth with some systems achieving over 6 THz of bandwidth [67]. To convert the time dependent current measurement $E(t)$ to a frequency dependent function $f(\omega)$ through a fast Fourier transform (FFT) following equation (35).

$$E(t) \xrightarrow{\text{FT}} \int_{-\infty}^{\infty} E(t)\, e^{-i2\pi\omega}\ dt = f(\omega) \tag{35}$$

This frequency dependent function produces a complex value at each frequency. The absolute value of this complex value represents the amplitude of a complex sine wave at that frequency while the complex component corresponds to the phase. The magnitude and phase components of the pulses in Figure 16, can be seen in Figure 17 and Figure 18.

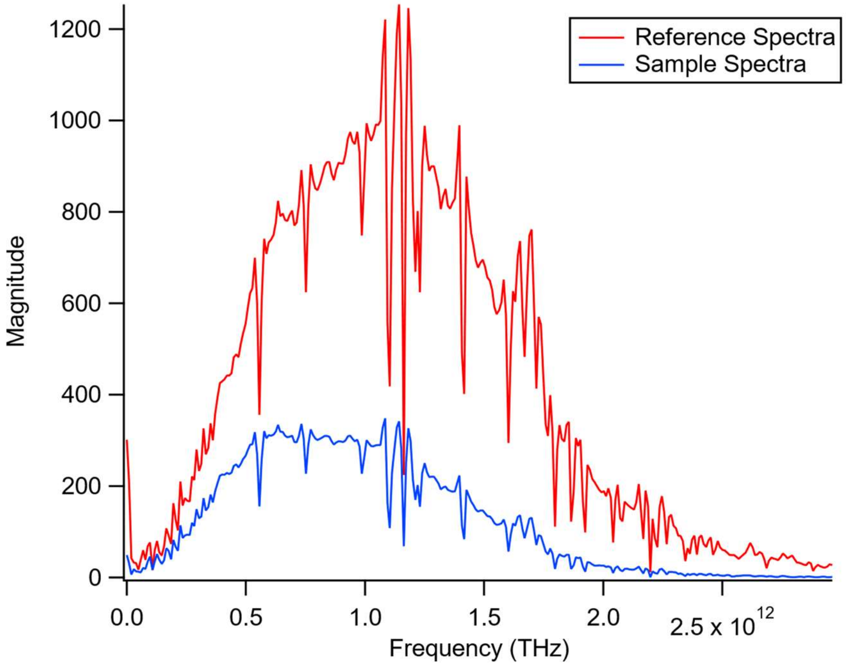

Figure 17. Frequency dependent magnitude of the reference and sample pulses from Figure 16.

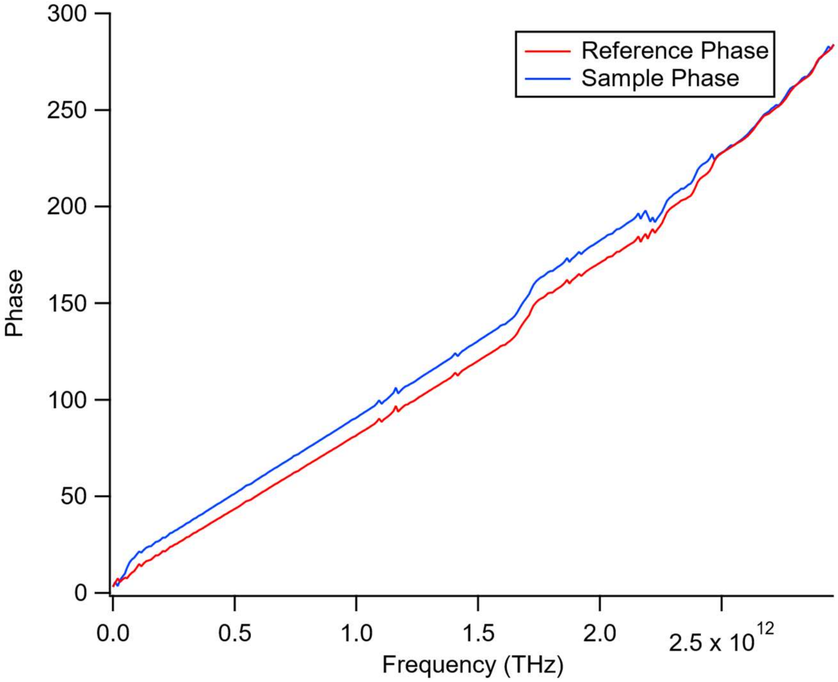

Figure 18 Frequency dependent phase of reference and sample pulses from Figure 16.

THz TDS offers many advantages over CW methods. The fine time sensitivity allows for simplification of the measurement of multiple layers of material [68]. In the case of a THz TDS sensor operating in reflection mode, the top surface reflections of a sample can be recognized due to their earlier arrival times, allowing for measurements to be simplified. The broad bandwidth of THz TDS may also give access to the resonant frequency of a molecule of interest.

There are two factors which prevent the development of THz TDS sensors for use outside of the laboratory, these are the cost of the systems and the relative complexity of their design. Turnkey THz TDS systems are available from multiple vendors which offer more compact footprints, but these systems have costs on the order of magnitude of $100,000 and typically have limited power, bandwidth, and time window. Laboratory scale systems have much larger footprints, and require supervision by a qualified scientist, but they typically have larger bandwidth, higher power, and larger achievable time windows.

2.4 EFFECTIVE MEDIUM THEORY

Effective medium theory has its roots in work done to relate macroscopic material properties such as relative permittivity ε, to microscopic molecular properties such as molecular polarizability $\boldsymbol{p}$. The first recognized work in the field is the derivation of the Clausius-Mossotti relation (equation (36)) which was independently developed by Ottaviano Fabrizio Mossotti and Rudolf Julius Emmanuel Clausius in 1850 and 1879 respectively [69, 70].

$$\frac{\varepsilon - 1}{\varepsilon - 2} = \frac{4\pi}{3} \sum_j N_j \boldsymbol{p}_{Vj} \tag{36}$$

This relation can be written in the more familiar form without the summation and looking at molecular polarizability $\boldsymbol{p}$ instead of polarizability volume $\boldsymbol{p}_V$ to highlight its significance, this is seen in equation (37).

$$\frac{\varepsilon - 1}{\varepsilon + 2} = \frac{\chi}{\chi + 3} = \frac{N\boldsymbol{p}}{3\varepsilon_0} \tag{37}$$

In this form we see the relationship between the bulk material properties of relative permittivity ε, dielectric susceptibility χ, and the microscopic molecular property of polarizability $\boldsymbol{p}$. The relation clearly shows that the bulk properties are proportional to molecular properties times their concentration per unit volume N. This one relation was the genesis of the field of effective medium theory and all subsequent models are refinements on this relation, each with their own assumptions which define what systems they are suitable to describe. For the Clausius-Mossotti method, it can accurately model local dielectric fields within a dipole but fails when the density of the molecules approaches and passes the critical point where $N = \frac{3}{4\pi \boldsymbol{p}_V}$. This method also assumes that all polarity $\boldsymbol{p}$ is induced so systems consisting of permanent dipoles cannot be modeled.

The next leap forward in the field came with James Clerk Maxwell Garnett's paper, "Colours in metal glasses and in metallic films" [71]. In this work Maxwell Garnett wanted to explain and predict the optical properties of glasses and films made with metallic inclusions and set about building his theory of material homogenization. This produced the well-known Maxwell-Garnett mixing formula seen in equation (38).

$$\frac{\varepsilon - \varepsilon_1}{\varepsilon + 2\varepsilon_1} = \eta_2 \left(\frac{\varepsilon_2 - \varepsilon_1}{\varepsilon_2 + 2\varepsilon_1}\right) \tag{38}$$

This formula models the bulk dielectric ε of a mixture consisting of a host material having a relative permittivity ε_1 with spherical inclusions with relative permittivity of ε_2 which are randomly distributed amongst the host and whose volume fraction relative to the volume of the host is given by η_2.

This mixing formula was sufficient for the purposes of Maxwell-Garnett, but issues arise if it is applied to systems where the assumptions inherent to the model do not hold. The model is only valid when $\eta_2 < 10^{-5}$ [72], it struggles to accurately model conductivity, and the choice of which material to regard as the host must be done with some care as the model is not symmetric when inverting materials 0 and 1.

In an effort to model more complex mixtures, the Maxwell-Garnett model has been rederived by many scientists, resulting in specialized effective medium models which are valid in certain cases. In the following subsections I will introduce two effective medium models which, when combined can accurately describe water present in a porous dielectric.

2.4.1 Bruggeman's Model

In 1935 V.D. Bruggeman published his work entitled "The calculation of various physical constants of heterogeneous substances." In this work he derived his model to calculate the dielectric constants and conductivities of mixtures of isotropic substances, this was the next great advancement in effective medium theory. Presented here is the derivation of this model summarized from [73].

To begin his derivation, Bruggeman broke the problem down and considered the contributions of both materials independently, this was done to solve the symmetry problem faced by the Maxwell-Garnett method. Treating material 1 first, we consider a homogeneous material with a relative permittivity ε containing a spherical inclusion with radius a made of material 1 with relative permittivity ε_1. The electric field in the material far away from the inclusion is a constant E_0 but close to the inclusion the electric field is described by equation (39) and inside the inclusion the electric field becomes equation (40).

$$E_{out} = \left(E_0 + 2\frac{C_1}{r^3}\right)\cos\theta\,\hat{r} + \left(-E_0 + \frac{C_1}{r^3}\right)\sin\theta\,\hat{\theta} \tag{39}$$

$$E_{in} = -A_1\cos\theta\,\hat{r} + A_1\sin\theta\,\hat{\theta} \tag{40}$$

In these equations C_1 and A_1 are constants described by equations (41) and (42) and represent the equivalent dipole moments which generate the fields E_{out} and E_{in} respectively.

$$C_1 = \left(\frac{\varepsilon_1 - \varepsilon}{\varepsilon_1 + 2\varepsilon}\right)a^3 E_0 \tag{41}$$

$$A_1 = -\left(\frac{3\varepsilon}{\varepsilon_1 + 2\varepsilon}\right)E_0 \tag{42}$$

Having these values allows us to calculate the electric flux deviation caused by the polarization of the inclusion which we call $\Delta\Phi_1$. Since the inclusion is spherical, we can calculate the flux by taking a disc with surface area πa^2 in a plane normal to the electric field E_0, i.e., $\theta = \pi/2$. Following Gauss's Law $\Delta\Phi_1$ is calculated as equation (43).

$$\varDelta\varPhi_1 = 2\pi\left(\int_0^a \mathrm{d}r\ r\varepsilon_1 E_{in} - \int_0^a \mathrm{d}r\ r\varepsilon E_0\right) = 2\pi a^2 \varepsilon E_0\left(\frac{\varepsilon_1 - \varepsilon}{\varepsilon_1 + 2\varepsilon}\right) \tag{43}$$

With the case of material 1 settled, Bruggeman proposed a bold and important hypothesis that in the case of the hybrid material, there should be zero average flux deviations. Essentially Bruggeman proposed that flux deviations are caused by single particle polarizations. A mathematical description of this hypothesis is seen in equation (44).

$$\eta_1 \varDelta\varPhi_1 + \eta_2 \varDelta\varPhi_2 = 0 \tag{44}$$

From this hypothesis we have the Bruggeman model seen in its standard form in equation (45), with a more convenient rearrangement present in equation (46).

$$\eta_1\left(\frac{\varepsilon_1 - \varepsilon}{\varepsilon_1 + 2\varepsilon}\right) + \eta_2\left(\frac{\varepsilon_2 - \varepsilon}{\varepsilon_2 + 2\varepsilon}\right) = 0 \tag{45}$$

$$\varepsilon = \frac{1}{4}\left(\beta + \sqrt{\beta^2 + 8\varepsilon_1\varepsilon_2}\right) \tag{46}$$

Here $\beta = (3\eta_1 - 1)\varepsilon_1 + (3\eta_2 - 1)\varepsilon_2$ and is used for simplicity.

The model which Bruggeman developed solved many of the issues with the Maxwell-Garnett method. Bruggeman's model is symmetric with respect to host or inclusion material designation, and it can be expanded to describe a medium consisting of any number of components. We can also work with materials where $\varepsilon_1 \gg \varepsilon_2$ or vice versa. Perhaps the model's most significant feature is its functionality over large concentration ranges, for instance, as $\eta_1 \rightarrow 1$ $\varepsilon \rightarrow \varepsilon_1$. This property also holds for $\eta_2 \rightarrow 1$ $\varepsilon \rightarrow \varepsilon_2$ through symmetry.

Bruggeman's model is widely used but it is by no means a perfect model. The derivation shown above was for mixtures that take form of a continuous host material with inclusions taking the form of a continuum of spheres. If it was rederived using differently shaped inclusions the behavior of the model's critical threshold [74], that is the volume fraction where the bulk dielectric properties of the material change from behaving more like material 1 to more like material 2 or vice versa, would differ greatly. This close association between inclusion shape and model behavior is undesirable and is in direct opposition to the universality concept in percolation theory [75].

2.4.2 Looyenga's Model

Dissatisfied with the shape dependence of Bruggeman's model, H. Looyenga derived his own model and presented it in his 1965 paper, "Dielectric Constants of Heterogeneous Mixtures". Looyenga first showed that Bruggeman's model and another more recent model by Böttcher [76] seen in equation (47), could both be derived from the same model but produce subtly different equations.

$$\eta_2 = \frac{(\varepsilon - \varepsilon_1)(2\varepsilon + \varepsilon_2)}{3\varepsilon(\varepsilon_2 - \varepsilon_1)} \tag{47}$$

In Looyenga's derivation of his new model he starts with a model consisting of two concentric spheres of radius a and b respectively. These spheres are placed in a continuous, homogeneous dielectric with relative permittivity ε_c, Figure 19, and the sphere of radius b is made of a pure material with permittivity ε_1. Looyenga's first key insight was to consider the sphere a to not be made of a pure material with permittivity ε_2, instead he considered it to be a mixture of materials 2 and 1 which differed very slightly to material 1. He also assumed that a was large compared to the particles of the mixture and that it contained many particles.

From this model the derivation follows by considering the behavior of the volume fraction of material 2, η_2, as a function of the permittivity of the system of spheres, ε, at neighboring values of ε. These values are represented as $\varepsilon - \Delta\varepsilon$ and $\varepsilon + \Delta\varepsilon$. Taylor expanding the function at these values yields equations (48) and (49).

$$\eta_2(\varepsilon - \Delta\varepsilon) = \eta_2(\varepsilon) - \Delta\varepsilon\eta_2'(\varepsilon) + \frac{1}{2}(\Delta\varepsilon)^2\eta_2''(\varepsilon) \tag{48}$$

$$\eta_2(\varepsilon + \Delta\varepsilon) = \eta_2(\varepsilon) + \Delta\varepsilon\eta_2'(\varepsilon) + \frac{1}{2}(\Delta\varepsilon)^2\eta_2''(\varepsilon) \tag{49}$$

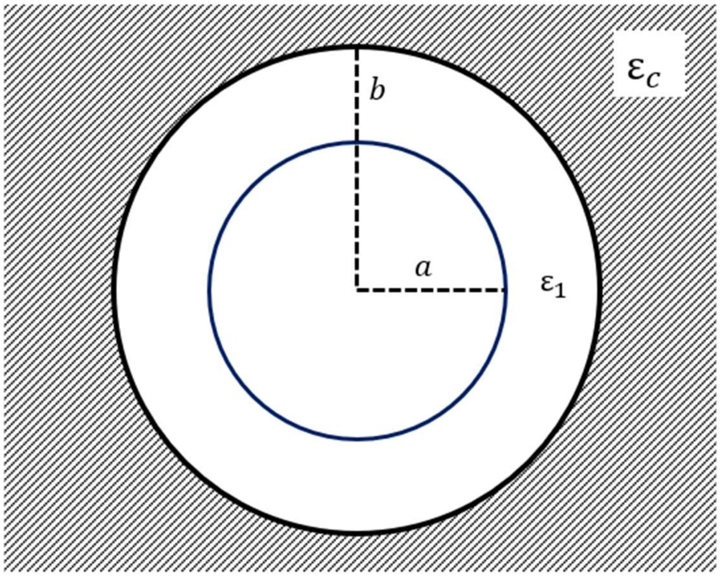

Figure 19. The model of concentric spheres which Looyenga considered when deriving his model of mixtures.

To apply Böttcher and Bruggeman's models to equations (48) and (49), Looyenga first rewrites Bruggeman's model from the form seen in equation (46) to the form seen in equation (50) in terms of η_2.

$$\eta_2 = 1 - \frac{\varepsilon_2 - \varepsilon}{\varepsilon_2 - \varepsilon_1}\left(\frac{\varepsilon_1}{\varepsilon}\right)^{\frac{1}{3}} \tag{50}$$

Now the two models can be applied if we consider the system with permittivity ε to be composed of modified volume fractions $(1 - \eta_2^*) \equiv \eta_1^*$ with permittivity $(\varepsilon - \Delta\varepsilon)$, and η_2^* with permittivity $(\varepsilon + \Delta\varepsilon)$. η_2^* is related to the previous values $\eta_2(\varepsilon - \Delta\varepsilon)$ and $\eta_2(\varepsilon + \Delta\varepsilon)$ by equation (51).

$$\eta_2^* = \frac{\eta_2(\varepsilon) - \eta_2(\varepsilon - \Delta\varepsilon)}{\eta_2(\varepsilon + \Delta\varepsilon) - \eta_2(\varepsilon - \Delta\varepsilon)} \tag{51}$$

Now with equations (48) and (49), we can simplify this to the form in equation (52).

$$\eta_2^* = \frac{1}{2} - \frac{1}{4}\Delta\varepsilon\frac{\eta_2''(\varepsilon)}{\eta_2'(\varepsilon)}$$

(52)

In this form we can apply either Böttcher or Bruggeman's model in the case where $\eta_2 \equiv \eta_2^*$, $\varepsilon_1 = \varepsilon - \Delta\varepsilon$ and $\varepsilon_2 = \varepsilon + \Delta\varepsilon$. First, applying Böttcher's model, we get equation (*53*).

$$\eta_2^* = \frac{\Delta\varepsilon}{3\varepsilon} * \frac{3\varepsilon + \Delta\varepsilon}{2\Delta\varepsilon} = \frac{1}{2} + \frac{\Delta\varepsilon}{6\varepsilon}$$

(53)

Combining equations (52) and (53) we get a differential equation for η_2 seen in equation (54)

$$3\varepsilon\eta_2''(\varepsilon) + 2\eta_2'(\varepsilon) = 0$$

(54)

This differential equation has the solution given in equation (55) where C_1 and C_2 are integration constants.

$$\eta_2 = C_1\varepsilon^{\frac{1}{3}} + C_2$$

(55)

To solve for these integration constants, we simply apply the boundary conditions $\eta_2 = 0, \varepsilon = \varepsilon_1$ and $\eta_2 = 1, \varepsilon = \varepsilon_2$. Plugging in these boundary conditions and solving gives us Looyenga's model. In equation (56) we see the model which solves for the volume fraction η_2, while equation (57) shows the rearrangement which allows for the solution of the permittivity of the mixture ε.

$$\eta_2 = \frac{\varepsilon^{\frac{1}{3}} - \varepsilon_1^{\frac{1}{3}}}{\varepsilon_2^{\frac{1}{3}} - \varepsilon_1^{\frac{1}{3}}} \tag{56}$$

$$\varepsilon = \left[\left(\varepsilon_2^{\frac{1}{3}} - \varepsilon_1^{\frac{1}{3}}\right)\eta_2 + \varepsilon_1^{\frac{1}{3}}\right]^3 \tag{57}$$

These results may also be derived by applying Bruggeman’s formula to (52) and if the higher powers of the term $\Delta\varepsilon$ are ignored (this is valid because we make the assumption that $\Delta\varepsilon$ is very small) we arrive back at equation (56) and (57).

This model was very successful at simulating the permittivity’s of the mixtures which Looyenga was concerned with. In his paper he presented a comparison of his model with experimental data measuring the permittivity of a mixture of glass spheres with permittivity $\varepsilon_2 = 4.594$ dispersed in a solution of carbon tetrachloride $\varepsilon_2 = 2.228$. This comparison showed it outperforming both Böttcher and Bruggeman’s models. The primary advantage that Looyenga’s model has over Bruggeman’s is that the shape of the inclusions is never considered in the derivation, this is hugely important when dealing with mixtures of irregularly shaped particles. However, from the derivation we can clearly see that there are some assumptions made which limit the applicability of Looyenga’s model. Primarily, the Looyenga model is only suitable for systems where ε_2 and ε_1 are similar. However in literature the Looyenga model has been found to perform similarly to Bruggeman’s model and even the Maxwell-Garnett model when applied correctly [77, 78] this serves to highlight the subtle differences between these models.

2.5 THE DEBYE RELAXATION AND WATER

When applying effective medium theory to a mixture where one of the materials is water, care must be taken when selecting a value for the permittivity of water. There are many examples in the literature of studies dedicated to measuring the complex permittivity of liquid water at a wide range of frequencies and temperature [79-84]. Going to the literature and trying to find data that was taken at the temperature and frequency of interest becomes impractical and at times impossible, this is where the Debye model is invaluable.

In his 1929 work, "Polar Molecules", Peter Debye sought to explain how polar molecules like water react in an electric field. He considers an ensemble of non-interacting molecules placed in a uniform electric field as the starting point and then considers what happens when the field is turned off. Debye assumed, incorrectly, that the molecules would undergo Brownian rotational motion and return to their rest state. Although his assumption as to why the effect happens was incorrect, he had discovered dipole relaxation [85] and was able to model it by linearizing the diffusion equation in spherical coordinates arriving at the Debye model seen in equation (58).

$$\varepsilon(\nu) = \varepsilon_{\infty}(t) + \frac{\varDelta}{1 - i2\pi\nu\tau} \tag{58}$$

Here ε is the complex relative permittivity of the system of molecules $\varepsilon = \varepsilon' - i\varepsilon''$, ε_{∞} is the high frequency limit of the relative permittivity of the water molecules, ν is the frequency of the applied electric field, Δ is a constant with the definition $\varDelta = \varepsilon_s - \varepsilon_{\infty}$ where ε_s is the static or low frequency relative permittivity of the water molecules and τ is the Debye relaxation time. The Debye relaxation time is dependent on the rotational friction constant ζ as $\tau = \frac{\zeta}{2k_BT}$ where T is the temperature and k_B is the Boltzmann constant. We can write ζ using Stokes' law which states that the rotational friction experienced by a sphere of radius R rotating in a medium with a shear viscosity η as equation (59).

$$\zeta = 8\pi\eta R^3$$

(59)

The application of the Stokes law directly leads to the Debye-Stokes model for the temperature dependent Debye-Stokes model seen in equation (60).

$$\tau(T) = \frac{4\pi\eta(T)R^3}{k_B T}$$

(60)

Even though Debye's assumption as to what his model was explaining was incorrect, with molecular dynamics showing that the molecular relaxation occurs as discontinuous "jumps" rather than Brownian rotations [86-90], the Debye model has been used to model the relative permittivity of liquid water to great success.

The single Debye model, shown in equation (58), has been shown to be valid up to approximately 90 GHz where it begins to underestimate the relative permittivity [91]. To get around this the model can be expanded to take any number of relaxation times into account. This expansion for both the real and imaginary components of ε are seen in equations (61) and (62).

$$\varepsilon'(\nu, t) = \varepsilon_s - (2\pi\nu)^2 \left(\frac{\tau_1^2 \Delta_1}{1 + (2\pi\nu\tau_1)^2}\right) + \cdots + \left(\frac{\tau_n^2 \Delta_n}{1 + (2\pi\nu\tau_n)^2}\right)$$

(61)

$$\varepsilon''(\nu,t) = 2\pi\nu\left(\frac{\tau_1^2\Delta_1}{1+(2\pi\nu\tau_1)^2}\right)+\cdots+\left(\frac{\tau_n^2\Delta_n}{1+(2\pi\nu\tau_n)^2}\right)$$

(62)

Hamelin et.al. [92] found the static permittivity of liquid water at standard atmospheric pressure and in the temperature range 0-100 °C to be fit to the temperature t by the polynomial in equation (63).

$$\varepsilon_s(t) = 87.9144 - 0.404399t + 9.58726 * 10^{-4}t^2 - 1.32892 * 10^{-6}t^3$$

(63)

In his 2006 work, "Permittivity of Pure Water, at Standard Atmospheric Pressure, over the Frequency Range 0-25 THz and the Temperature Range 0-100 °C" [91], W. J. Ellison reviewed all known experimental data measuring the relative permittivity of liquid water over the frequency range 0-25 THz and temperature range 0-100 °C, and sought to find an expanded Debye model which best fit the data. To fit the parameters τ and Δ, Ellison used the models seen in equations (64) and (65) where t_c is the critical temperature and is part of the model.

$$\tau_i(t) = c_i e^{\left(\frac{d_i}{(t+t_c)}\right)} \text{ for } 1 \le i \le n$$

(64)

$$\Delta_i(t) = a_i e^{(b_i t)}$$

(65)

He found that to accurately model data beyond the range of 90 GHz a two parameter Debye model was needed. The two-parameter model was found to be valid until 500 GHz where a third parameter was needed to extend the range to 3 THz. Table 1 shows the parameters for the one Debye relaxation model, Table 2 shows the parameters for the two Debye relaxation model, and Table 3 shows the parameters for the three Debye relaxation model.

Parameter	Value
a_1	80.69715
b_1	0.004415996
c_1	$1.367283 * 10^{-13}$
d_1	651.4728
t_c	133.0699

Table 1. Fitting parameter for the one parameter Debye model from Ellison et.al.

Parameter	Value
a_1	79.42385
b_1	0.004319728
c_1	$1.352835 * 10^{-13}$
d_1	651.4728
a_2	3.611638
b_2	0.01231281
c_2	$1.005472 * 10^{-14}$
d_2	743.0733
t_c	132.6248

Table 2. Fitting parameter for the two parameter Debye model from Ellison et.al.

Parameter	Value
a_1	79.3319
b_1	0.00432795
c_1	$1.353345 * 10^{-13}$
d_1	653.1149
a_2	3.610705
b_2	0.01069618
c_2	$3.654\,087 * 10^{-16}$
d_2	1220.405
a_3	1.966861
b_3	0.00251792
c_3	$5.098792 * 10^{-15}$
d_3	396.1829
t_c	132.4965

Table 3. Fitting parameter for the three parameter Debye model from Ellison et.al.

Although the origin of the third relaxation that Ellison fits to extend his models range is unknown and somewhat controversial, it is able to accurately model the relative permittivity of liquid water over a very large range of frequencies and a useful range of temperature. Thus it makes up an important part of any effective medium model looking to describe a system containing liquid water.

3 TERAHERTZ MOISTURE MAPPING FOR POROSITY

This section serves to introduce and cover one of the two main projects involved in this work. This project is sponsored by Aramco Americas: Aramco Research Center – Houston and was completed in collaboration with scientists from the Houston and Cambridge center. The goal of this work is to build upon previous work using THz TDS to measure the porosity in core samples taken from oil well sites. The primary objective was to use THz TDS to image lateral pore distribution within core samples, with a secondary objective being to correlate these maps with traditional methods of porosity measurements. If successful the workflow developed in this work could be used as a novel, complimentary method of core sample analysis.

3.1 BACKGROUND

Using THz spectroscopy to characterize porosity within a sample is not a new idea, with numerous examples in literature [93-95], and notions of this application appearing as early as 2003 [96]. Most of this work has been done with the focus of measuring the porosity of pharmaceutical tablets with encouraging results. In these studies, porosity was quantified by measuring the proportion of a THz beam that gets scattered by the pores within a compressed powder. More recently, the oil and gas industry has become interested in novel porosimetry methods to complement their existing core analysis routines.

When establishing an oil well site and drilling the initial bore hole, petrophysicists and well site engineers have samples of the strata taken at regular depths along the bore. These samples, typically called "core samples" are long cylindrical plugs of the rock that make up the well site and they hold valuable information about the quality of the oil to be found there. With oil well sites typically made up of many wells pumping oil from the same large reservoir, and with the recovery of core samples costing up to and over one million dollars, samples are usually only taken from a few or even one well. One parameter that is of special interest when measuring core samples, particularly those from carbonate wells, is the bulk porosity and the concentration of micropores.

The porosity is of such interest to core analysts, and all others working the well, because of the oil retention within these pores [97-100] which has recently been highlighted in the literature. Oil present in the well exists within the pores of the reservoir rock and during primary production will freely flow out of the large pores and fractures in the rock. Over time, this free-flowing oil will be depleted and the remaining hydrocarbons trapped in the smaller pores must be extracted by more complicated means. Even with secondary production methods most well sites cannot recover up to 50% of the oil present, which remains trapped in the micropores.

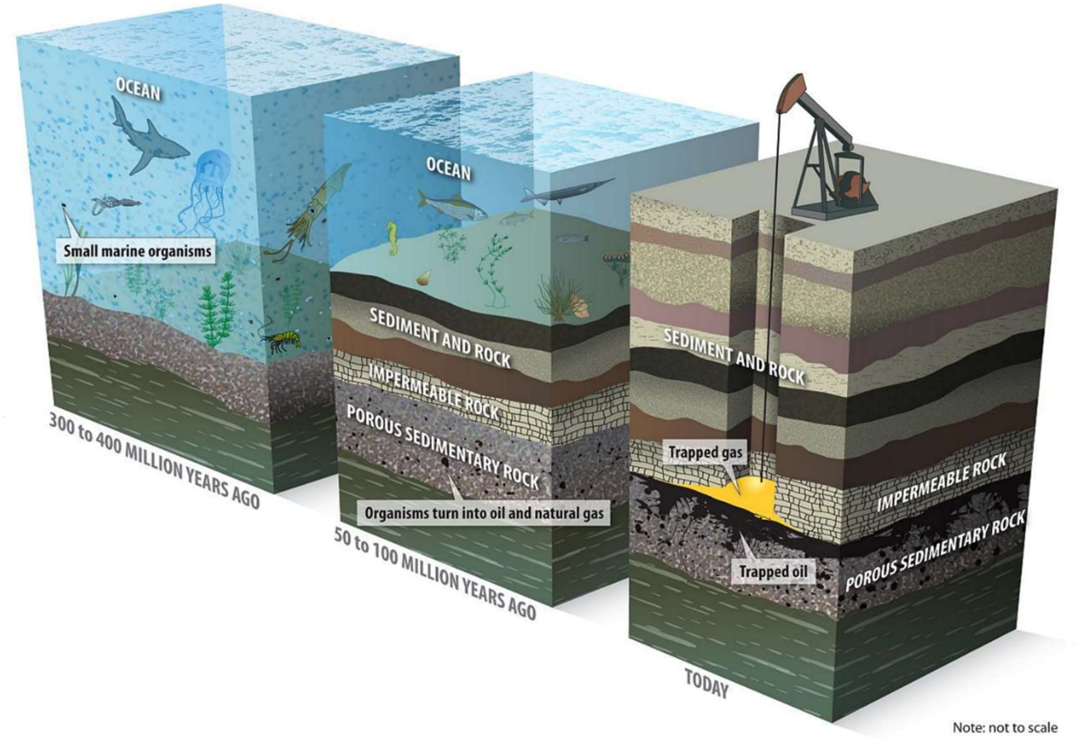

Figure 20. A diagram showing the formation of carbonate oil reservoirs and how their formation results in oil trapped in porous reservoir rock. Image sourced from [101].

This effect is most pronounced in carbonate reservoirs, which are in ancient dried out seabeds, and have geologies dominated by carbonate rock. This rock is extremely porous and heterogeneous in pore type, size, and distribution [102-104] with a large concentration of micropores. With 60% of global petroleum reserves located in carbonate reservoirs, efficient methods to quantify microporosity in core samples must be developed to support more effective reservoir utilization.

Current methods utilized by core analysts to measure the porosity of a sample include mercury intrusion (MICP), optical and scanning electron microscopy (SEM), computed tomography (CT), and gas porosimetry[105-113]. These methods all have their own strengths and weaknesses, with mercury intrusion able to resolve pores over a very wide range of throat sizes but also contaminating and effectively destroying the measured sample [114]. Gas adsorption can provide quick measurements of both porosity and surface roughness but can require highly trained personnel to run. Standard optical microscopy is quite limited in accuracy as it can only measure surface porosity, and SEM and CT measurements require large and expensive instrumentation in carefully controlled lab environments. SEM and CT measurements do offer more illustrative porosity heterogeneity data by mapping internal pore structures [115], but the intensive image processing involved leads to slow turnaround times. These slow turnaround times can be troublesome when decisions about oil recovery methods depend on them.

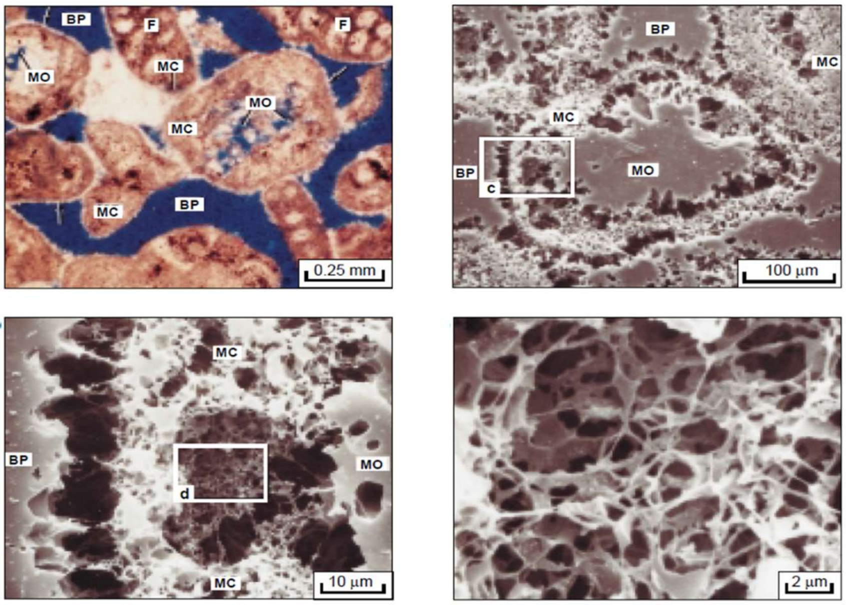

Figure 21. Images of the porosity within carbonate reservoir rock. Top left is a thin section photomicrograph, all others are taken with SEM. Sourced from [99].

Clearly a complementary porosity measurement method, which could provide accurate bulk porosity as well as map porosity distribution across a core sample quickly, could for more efficient well operation. Such a method would allow for decisions to be made quickly and with a high degree of confidence, while samples are sent off for more rigorous testing at offsite laboratories. THz spectroscopy may provide a platform to develop such a measurement method.

In 2017 Aramco Americas Research Center – Houston, sponsored a project to study using THz scattering to quantify porosity in core samples [116]. In this study, a method was devised to calculate the average porosity in a 1 mm subsection of thin (4.5 mm) pieces of core sample analogue. THz TDS was used to examine scattering and absorption over a bandwidth of approximately 2.5 THz. To accurately measure the micropores, which are less than 1 µm in diameter, the authors found that simple scattering caused by an empty pore was not enough. This is not surprising as the index of refraction of the $CaCO_3$ at 1 THz (n = 1.8) and the index of the air-filled pores at 1 THz ($n \approx 1$) are not sufficiently different to cause significant scattering. To increase the contrast in the indices of refraction between the porous and non-porous areas, water was saturated into the pores. The presence of water in the pores increases the index contrast as the index of the water filled pores at 1 THz ($n \approx 4.3$) is larger than that of the $CaCO_3$ which should increase scattering by a small amount but a large loss of power was observed. This increase in loss of power in the THz wave was due to the strong broadband absorbance of liquid water. This effect served to improve the signal to noise of the measurements. Once saturated with water, the samples were allowed to dry over 1200 minutes, and they were measured with THz TDS every three minutes. This procedure was automated to measure 12 samples simultaneously, 6 consisting of a core analogue material A, and 6 consisting of a similar core analogue material B.

By measuring the change in peak-to-peak amplitude of the THz pulse as a factor of dehydration time (Figure 22), the authors were able to apply diffusion theory to calculate scattering, average pore diameter, and compare percent micro and macro porosity concentrations. The results of these calculations for samples A and B compared to measurements taken using the MICP method are present in Figure 23.

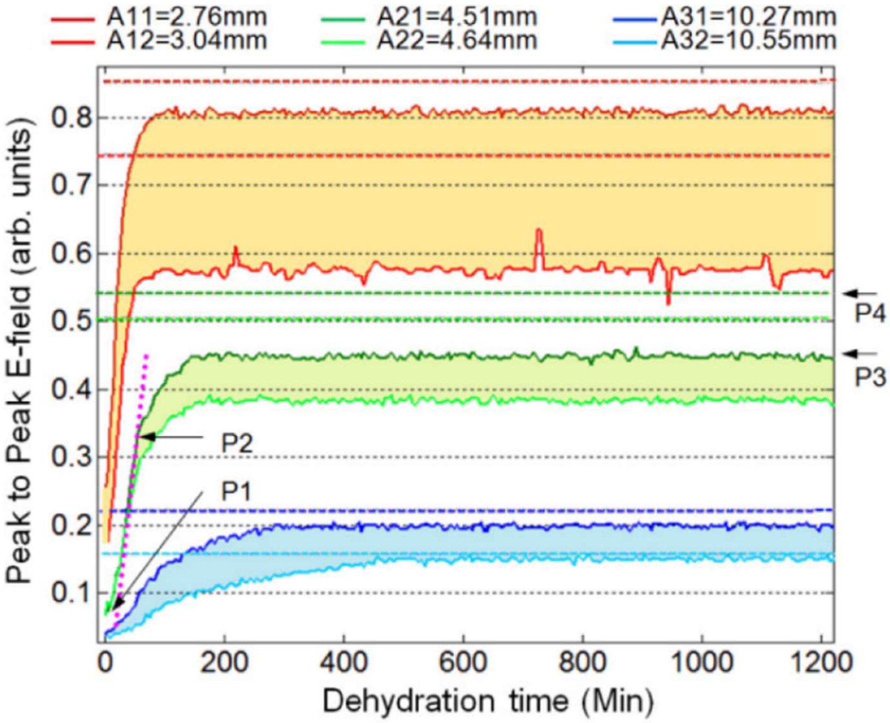

Figure 22. Peak-to-peak amplitude of the THz pulse passing through a sample of core analogue material A as a function of dehydration time. The solid lines are the measurement data while the dashed lines are the peak-to-peak amplitudes measured for the dry samples. Sourced from [116].

Sample	A	B	comparison
M.I. Total porosity	11.69	13.8	B has 2.1% higher porosity
THz scattering through diffusion theory	15.3	32.3	B has 17% higher estimated porosity
M.I average pore diameter (μm)	0.35	0.38	B has 3% higher estimated average pore diameter
THz scattering through diffusion theory pore diameter (μm)	255	332	B has 30% higher estimated average pore diameter
M.I. at 1μm (macro:micro)	53.37%:46.63%	65.46%:34.56%	B has 12% more macropores
THz water profilometery	54.69%:45.31%	67.57%:32.43%	B has 13% more macropores

Figure 23. A table comparing data from the mercury intrusion and the THz scattering dehydration method. Sourced from [116].

This comparison shows that the THz scattering dehydration method is in good agreement with the MICP method for comparative calculations such as the ratio of macropore to micropore concentration but is far off in quantitative calculations such as the estimated average pore diameter and total porosity. These errors come from limitations in the diffusion theory used for the THz method. The diffusion theory relies on estimating Mie scattering which only happens for pores larger than 0.1λ. Overall this study showed that THz TDS can be made sensitive to microporosity in core sample material if a suitable contrast is used. It also proved that by measuring the change in peak-to-peak amplitude of the THz pulse as a function of water content, reasonably accurate measurements of the porosity and microporosity of a sample can be calculated. These two discoveries are important to establish THz TDS as a viable method to measure porosity. In 2020 Aramco Americas Research Center – Houston, collaborated with our team at WPI to further the development of a THz based porosity measurement.

3.2 EXPERIMENTAL DESIGN

To build on the work previously done to quantify core sample porosity using THz TDS we devised a new method which consists of THz TDS imaging, selective pore clearing, and porosity by mass calculations. Our workflow is described below.

3.2.1 Sample Preparation

Our new method was tested with 8 samples prepared from 3 different core plugs. Plugs 2 and 3 were made of Indianna Limestone ($CaCO_3$) with relatively well understood porosities. Indianna Limestone is typically used as a representative carbonate for porosity testing and samples with known porosities, the plugs for this study were sourced from Kocurek Industries (Caldwell, Texas). Plug 1 was from a carbonate field and was used to test the method against real world samples. From each cylindrical core plug, samples were cut at 2 mm and 4 mm thick, as well as additional 6 mm thick samples which were only cut from plugs 2 and 3. The resulting circular samples were cut in half leaving two half-moon shaped samples. This new method was trialed on one of these half-moon segments for each thickness and each core type, the remaining half was retained. Before measuring, the samples were cleaned to clear any pore occluding dust resulting from the cutting process. This cleaning consisted of submerging the sample in Type 1 ultrapure water and placing it under vacuum for 2 days, then centrifuging the bulk of the water and any dust or debris out of the sample, finally the samples were dried in an oven at 100 °C to clear any remaining water.

3.2.2 THz TDS Imaging

With the primary goal being able to map the porosity across the core sample, a Toptica Teraflash with an imaging extension was used. The imaging extension was set up to take TDS measurements across the sample in 0.5 mm steps. This step size was chosen to balance resolution and imaging time with smaller step sizes leading to longer imaging time. With the bandwidth of the Teraflash reaching from 200 GHz to 2.5 THz, the maximum expected resolution of the system would be approximately 100 μm from the diffraction limit. From an observation of the absorption spectra through a core sample, it was seen that most of the transmitted power was below 500 GHz meaning that the choice of 0.5 mm is sufficiently close to the optical resolution of the system. This discussion of the systems' resolution shows that it will not be possible to image individual micropores which are on the order of 1 μm in diameter. The system will instead rely on imaging clusters of micropores.

At each step, two TDS measurements were averaged together to improve the signal to noise ratio (SNR). The data from the TDS imaging system is saved as a comma separated variable (csv) file with columns containing THz electric field strength at 0.5 ps increments along the 70 ps measurement window, and rows representing each pixel in the image. These measurements were translated into loss images using a custom data processing script written in IgorPro which first arranges the data into a 3D matrix with dimension i, j, and k where the ith and jth dimensions are the actual image dimensions and the kth dimension is the THz electric field vs time. The script then measures the peak-to-peak amplitude at each pixel (i, j), and creates a new 3D matrix with the same i and j dimensions but k is replaced with k_{max} which is the peak-to-peak ($THz_{max} - THz_{min}$) value of the THz pulse at the corresponding (i, j) pixel. These values can then be assigned corresponding gray-scale colors with black representing high loss and white representing low loss. The output of this script is images like the one seen in Figure 24 (b-d).

With a simple linear color scale, where white corresponds to the maximum value (379 nA) and black to the minimum value (0.28), as used in Figure 24 (b), the contrast between the average peak-to-peak values of the pixels in the open area around the sample (~377nA) and the average values within the sample (~0.5 nA) are too great and no internal features can be resolved. IgorPro allows for the color scale to be set logarithmically, with a step along the color scale corresponding to a factor of ten increase in peak-to-peak amplitude. Applying a logarithmic color scale to Figure 24 (b) results in Figure 24 (c), here we can begin to make out some regions of lower loss within the sample. Figure 24 (c) is also beginning to show the so-called “knife edge” effect which happens when propagating electromagnetic radiation strikes a well-defined edge and diffracts around it. This is explained by the Huygens-Fresnel principle which states that a well-defined obstruction to an electromagnetic wave, acts as a secondary source and creates a new wavefront. The new wavefront propagates into the geometric shadow area of the source [117, 118]. In our image the effect takes place along the edges of the sample not in contact with the sample harness, and results in the halo-like region at the top and bottom of Figure 24 (c) as well as the change in shape of Figure 24 (d). Figure 24 (d) has a linear color scale but the range of the scale was set by hand to balance internal structure visibility and image distortion, in this image the color scale went from black at 0.28 nA and white at 2 nA.

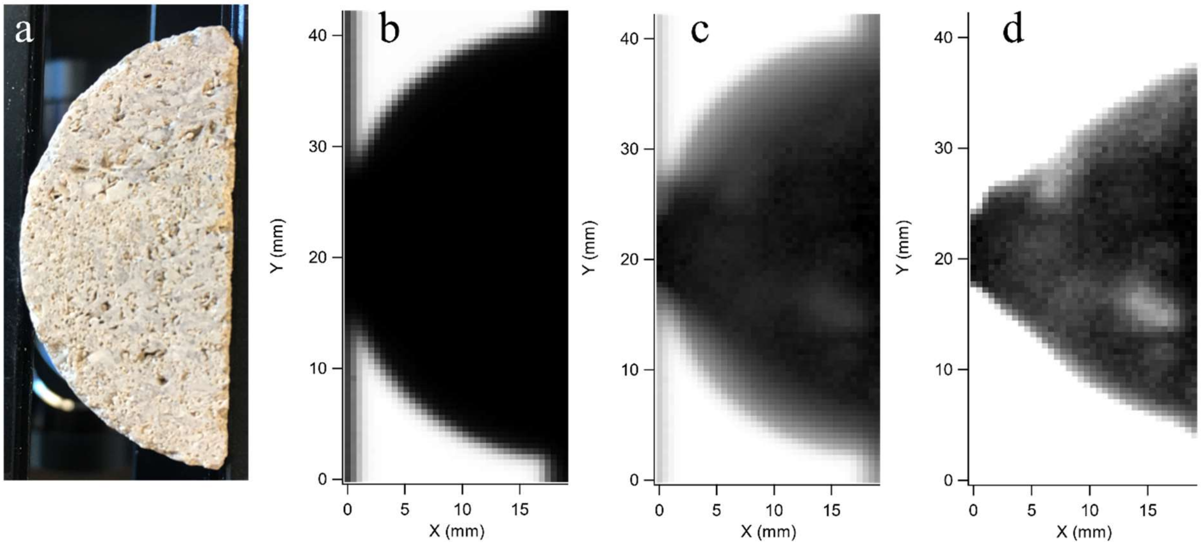

Figure 24. A comparison of loss images (b-d) using different color scaling with a photograph (a) to show surface features and sample fixture. (b) has a linear color scale over the whole range applied, (c) uses logarithmic color scaling over the whole range, (d) has linear scaling over a limited range with the high range cut to show internal features.

From these loss images, we can create maps of a sample's porosity. The previous work initially relied on scattering being the dominant loss factor, the scattering was induced by empty pores with sizes on the same magnitude of a wavelength. The authors found that by using water as a contrast fluid, better SNR and sensitivity to micropores could be achieved. Water can be hydrated into the pore structure of a sample and the dominant loss factor becomes broadband absorption. By imaging the core samples at varying levels of hydration and comparing the loss in the images, we can build maps of porosity. It is expected that the loss due to the water populated pores will result in an exponential decrease in transmitted intensity. This process is discussed in the next section.

3.2.3 Data Collection Workflow

When samples were first received, they were weighed using a Sartorius Entris II mass balance to obtain an initial dry mass $m_{dry,i}$. This initial mass could be used later to determine if any mineral loss occurred during the measurement procedure. The samples were then submerged in the ion-saturated water leftover from the pre-cleaning step, this water was used to prevent any further dissolution of the calcium carbonate in the sample. The samples and the water were placed under vacuum for 2 days to ensure full hydration of the internal pore structures. After 2 days the samples were removed from the vacuum chamber and the water, and excess water was blotted from their surface. The samples were weighed again to obtain a saturated mass m_{sat} and a 19 mm wide by 42 mm tall THz TDS image was taken of the sample with resolution of 0.5 mm per pixel. In this saturated image, loss occurs in the sample across the whole hydrated pore structure.

The samples were then centrifuged using an Eppendorf 5804 with an FA-45–6-30 fixed angle rotor to apply capillary pressure to the pores and clear pores above a desired size threshold. The pressure that would need to be applied to clear these pores was found using equation (66) which relates pore radius r_p, contact angle θ, and the interfacial tension σ, to the capillary pressure P_C of a capillary tube.

$$P_C = \frac{2\sigma \cos\theta}{r_p} \tag{66}$$

Samples were assumed to be water wet with a contact angle of 45° and the interfacial tension between the water and the air which would replace it was assumed to be 72.8 mN/m. With these constants, the necessary P_C to clear the pores larger than the two microporosity sizes of interest were found with a P_C of 30 psi need to clear pores with diameters larger than 1 µm and 100 psi needed to clear all pores with diameters larger than 0.3 µm. The rotational speed of the centrifuged was set to apply the desired P_C with 3140 rpm applying 30 psi and 5720 rpm applying 100 psi. After centrifugation, samples were weighed again to obtain a post centrifuged mass m_{cent}, and THz TDS images were taken of the samples. In these images, loss occurs in the sample in areas with high concentrations of micropores with diameters less than either 1 µm or 0.3 µm depending on P_C applied.

Finally, the samples were oven dried at 100 °C and under vacuum overnight to clear water from all pores. After drying the samples were weighed again to obtain a final dry mass $m_{dry,f}$ and a final THz TDS image was taken. In these images loss occurs primarily due to surface scattering of the sample, changes in the mineralogy within the sample, and broadband absorbance of the $CaCO_3$.

This workflow was repeated two to three times per 2 mm, 4 mm, and 6 mm samples clearing pores larger than 1 µm and once for the 4 mm and 6 mm samples clearing pores larger than 0.3 µm.

3.3 ANALYSIS AND RESULTS

After each run of the above workflow, the collected images and mass data were analyzed to map and calculate porosity. Porosity maps were made by comparing the THz loss images while porosity was calculated using the mass measurements m_{sat}, m_{cent}, $m_{dry,i}$, and $m_{dry,f}$ as well as by averaging the generated porosity maps. This analysis is discussed in detail below.

3.3.1 Porosity by Mass

The mass data taken at every step of the workflow can be used to calculate the total porosity $\varphi_{m,t}$ and the microporosity $\varphi_{m,\mu pores}$. This is done by finding the volume of either the total porosity or micropores. To calculate the total porosity, we take the ratio of the saturated pore volume V_p, to the bulk volume of the sample V_b as shown in equation (67).

$$\varphi_{m,t} = \frac{V_p}{V_b} \tag{67}$$

Here V_p is calculated as the difference between the mass of the saturated sample m_{sat} and the dry sample m_{dry}, following equation (68) where the density of water ρ_w is assumed to be 1 g/cm^3. V_b is the bulk volume which is calculated by dividing $m_{dry,i}$ by the bulk density of the sample ρ_b following equation (69).

$$V_p = \frac{m_{sat} - m_{dry,i}}{\rho_w} \tag{68}$$

$$V_b = \frac{m_{dry,i}}{\rho_b} \tag{69}$$

The bulk densities of the samples were calculated from their dimensions and masses. The bulk density of samples 1 and 2 was 2.2 g/cm^3 and sample 3 had a bulk density of 2.3 g/cm^3.

To calculate the amount of microporosity $\varphi_{m,\mu pores}$ from the mass measurements, we follow a similar process as with the total porosity but equation (67) is modified as equation (70).

$$\varphi_{m,\mu pores} = \frac{V_{\mu pores}}{V_b}$$

(70)

Here $V_{\mu pores}$ is the volume of micropores and is calculated as the difference between the mass of the sample after centrifugation m_{cent} and after the final drying step $m_{dry,f}$. This calculation is shown in equation (71).

$$V_{\mu pores} = \frac{m_{cent} - m_{dry,f}}{\rho_w}$$

(71)

With both the total porosity $\varphi_{m,t}$ and the amount of microporosity $\varphi_{m,\mu pores}$, the ratio of the two can be calculated directly. This ratio gives the relative amount of microporosity in the sample.

3.3.2 Porosity Maps

Porosity maps were generated from the THz loss images using an image analysis script written in IgorPro 8. To use the script the user first loads the image data into the script described in section 3.2.2 and places the "A" cursor at the bottom right corner of the sample. Then the user presses the "Cut Image" which crops the 19 mm by 42 mm image into a 17 mm by 38 mm image with the bottom right corner of the cropped image where the user placed the cursor. This cropping is done to mitigate errors caused by slight variations in the placement of the sample in the image between runs as well as to cut the sample holder from the images. The simple user interface of this script as well as an example of a correctly placed "A" cursor is seen in Figure 25. It is expected that the user will crop and export every image generated in a during a run of the workflow before moving onto the next step.

After the cropping is finished, the user loads them into the image analysis script whose user interface can be seen in Figure 26. Depending what type of map, the user wants to generate, they will pick which images to load in based on Table 4.

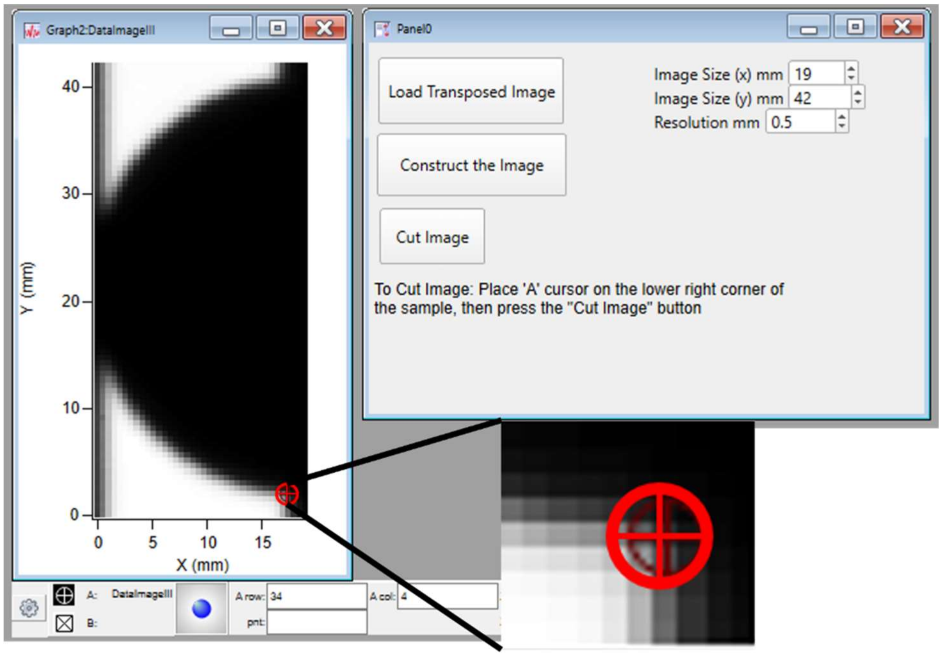

A row: 34

pnt:

A col: 4

Image Size (x) mm 19

Image Size (y) mm 42

Resolution mm 0.5

To Cut Image: Place 'A' cursor on the lower right corner of the sample, then press the "Cut Image" button

Figure 25. The user interface of the THz loss image script, showing a correctly placed “A” cursor (in red) and the “Cut Image” button. Note the two black vertical lines on either side of the sample image, these are the metal sample holder which totally blocks THz transmission.

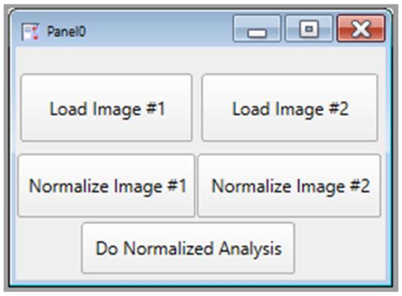

Figure 26. The user interface of the image analysis script.

Map to be generated	Image #1	Image #2
Total Porosity	Saturated	Dry
Microporosity	Centrifuged	Dry
Macroporosity	Saturated	Centrifuged

Table 4. Table showing what image choices generate each image for the image analysis script. After loading the appropriate images into the script, the user then normalizes the two images so that they can be compared. The normalization is done by dividing the intensity of every pixel by the maximum intensity and is done to mitigate errors caused by fluctuations in output power of the TDS system. Finally, the normalized images are analyzed by calculating the difference in intensity of every pixel and dividing that intensity by the average intensity of that pixel in both images. The calculation of this average difference is shown in equation (72) with the calculation of the average shown in equation (73).

$$\mathrm{AverageDif}_{i,j} = \frac{\left|\mathrm{image1}_{i,j} - \mathrm{image2}_{i,j}\right|}{avg} \qquad (72)$$

$$avg = \frac{\mathrm{image1}_{i,j} + \mathrm{image2}_{i,j}}{2} \qquad (73)$$

Figure 27 shows an example of a THz intensity difference map resulting from the analysis.

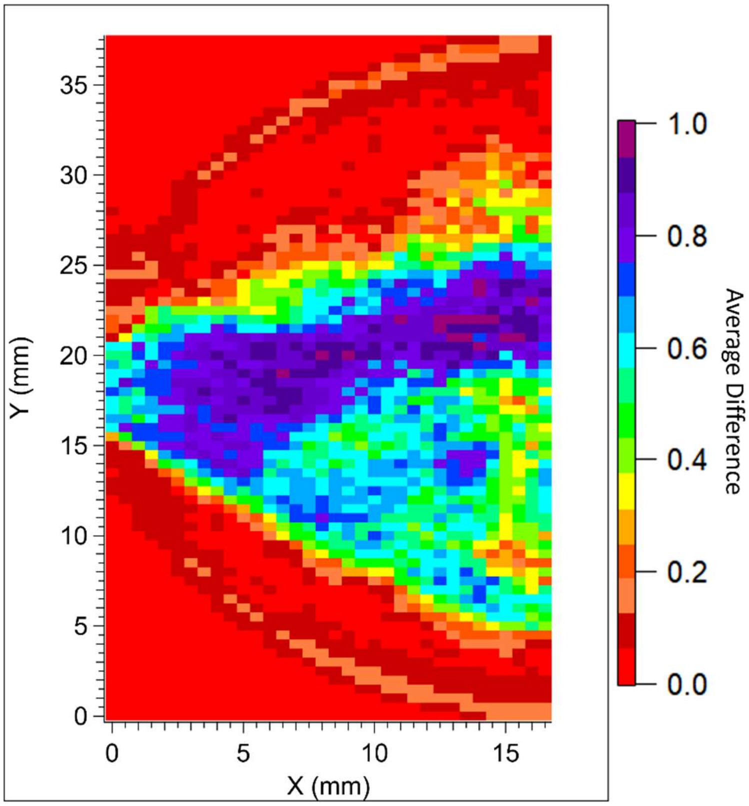

Figure 27. An example of a THz intensity difference map.

This analysis was run on every image collected during the workflow and Figure 28 shows a collage of the three THz images, the three THz porosity maps, and a photo of sample 3.

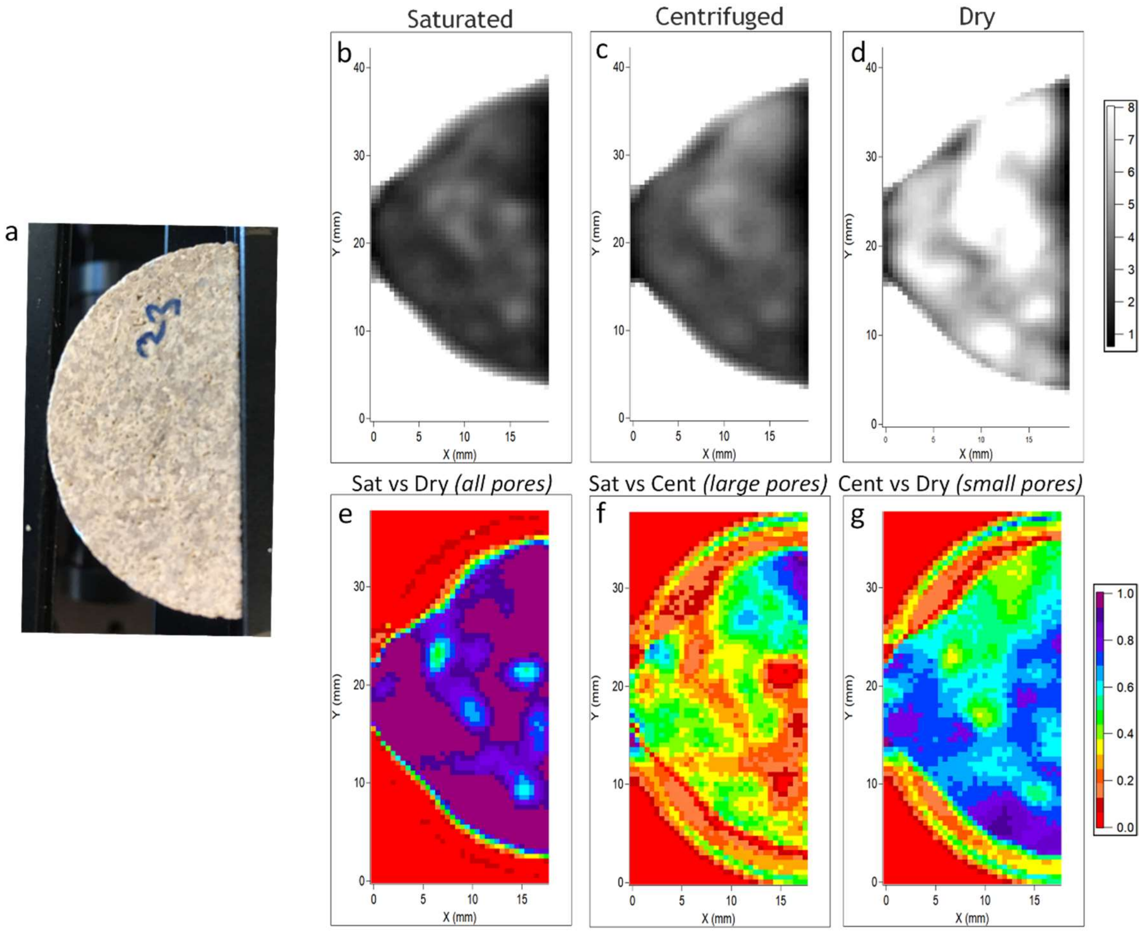

Figure 28. Loss and average loss difference THz images of sample 3 (4 mm thick) as a representative example of the data generated for all samples. (**a**) photograph, (**b-d**) loss images of the sample taken at the saturated, centrifuged (at 3140 rpm), and dried stages, and (**e-g**) attenuation difference maps analyzed by comparing the saturated and dried, saturated and centrifuged, and centrifuged and dried attenuation maps to represent the lateral variation of the saturated macropores (larger than 1 μm) and micropores (smaller than 1 μm). Sourced from [119].

3.3.3 Porosity by THz

Although the goal of this study is to simply image the regions macro and microporosity in carbonate samples, the loss images also can be used to estimate the relative amount of porosity and microporosity in a sample. This is done by modifying the image analysis script that generated the porosity maps to find the relative differences between the loss images at the three steps rather than the percent change as before. Once these new images were generated, IgorPro's image tools were used to draw a region of interest (ROI) around the sample and the average and maximum of this ROI could be measured. Figure 29 shows a relative difference map with an ROI drawn on it. The equation used for finding the percent total porosity in a sample from the ROI data is found as equation (74), where $THz_{sat,i,j}$ is the i,jth pixel of the saturated loss image $THz_{dry,i,j}$ is the i,jth pixel of the dried loss image, ρ_w is the density of water, and ρ_b is the bulk density of the sample.

$$\varphi_{THz,total} = \text{avg}\left(\frac{\frac{THz_{sat,i,j}}{THz_{dry,i,j}}}{\max\left(\frac{THz_{sat,i,j}}{THz_{dry,i,j}}\right)}\right) * \frac{\rho_w}{\rho_b} * 100$$

(74)

To calculate the percentage of micropores, with either throat diameters $d_p < 1$ µm or $d_p < 0.3$ µm depending on the centrifugation speed, versus the percentage of pores with throat diameters larger than those cleared during centrifugation equation (75) is used.

$$\varphi_{THz,\mu pores\_vs\_largepores} = \text{avg}\left(\frac{\frac{THz_{cent,i,j}}{THz_{sat,i,j}}}{\max\left(\frac{THz_{cent,i,j}}{THz_{sat,i,j}}\right)}\right) * 100$$

(75)

Finally, to calculate the percentage of micropores in a sample versus the total porosity in a sample $\varphi_{THz,\mu pores}$, which is the number typically given by MICP and is what is of most interest to those in the oil and gas industry, we combine equations (74) and (75) to get equation (76).

$$\varphi_{THz,\mu pores} = \mathrm{avg}\left(\frac{\dfrac{THz_{cent,i,j}}{THz_{sat,i,j}}}{\max\left(\dfrac{THz_{cent,i,j}}{THz_{sat,i,j}}\right)}\right) * \mathrm{avg}\left(\frac{\dfrac{THz_{sat,i,j}}{THz_{dry,i,j}}}{\max\left(\dfrac{THz_{sat,i,j}}{THz_{dry,i,j}}\right)}\right) * \frac{\rho_w}{\rho_b} * 100 \tag{76}$$

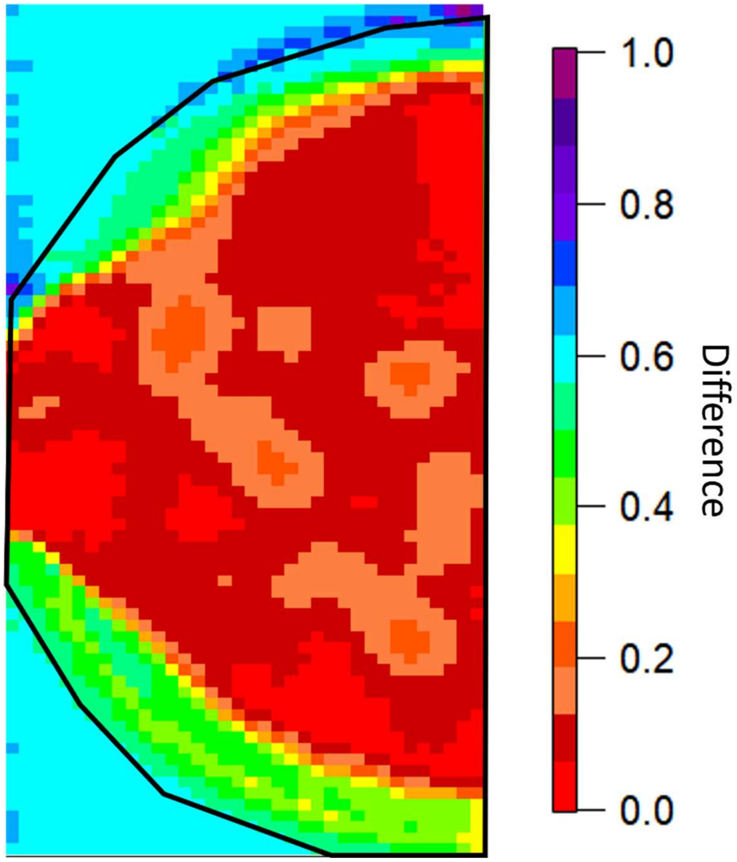

Figure 29. Average difference map of sample 3 comparing saturated and dry images from run 3 of the workflow. Using the ROI (in black) and IgorPro's image stats tool, the total porosity in sample 3 can be estimated using equation (74).

3.3.4 Results and Comparisons

Having run through the workflow 3 times using a centrifugation speed of 3140 rpm and once using a speed of 5720 rpm, 3 sets of images like those seen in Figure 28 were generated for pores with a throat diameter $d_p < 1$ µm and 1 set for pores with a throat diameter $d_p < 0.3$ µm.

Images for samples 1 and 2 for a run looking at pores with a throat diameter $d_p < 1$ μm are seen in Figure 30 and Figure 31.

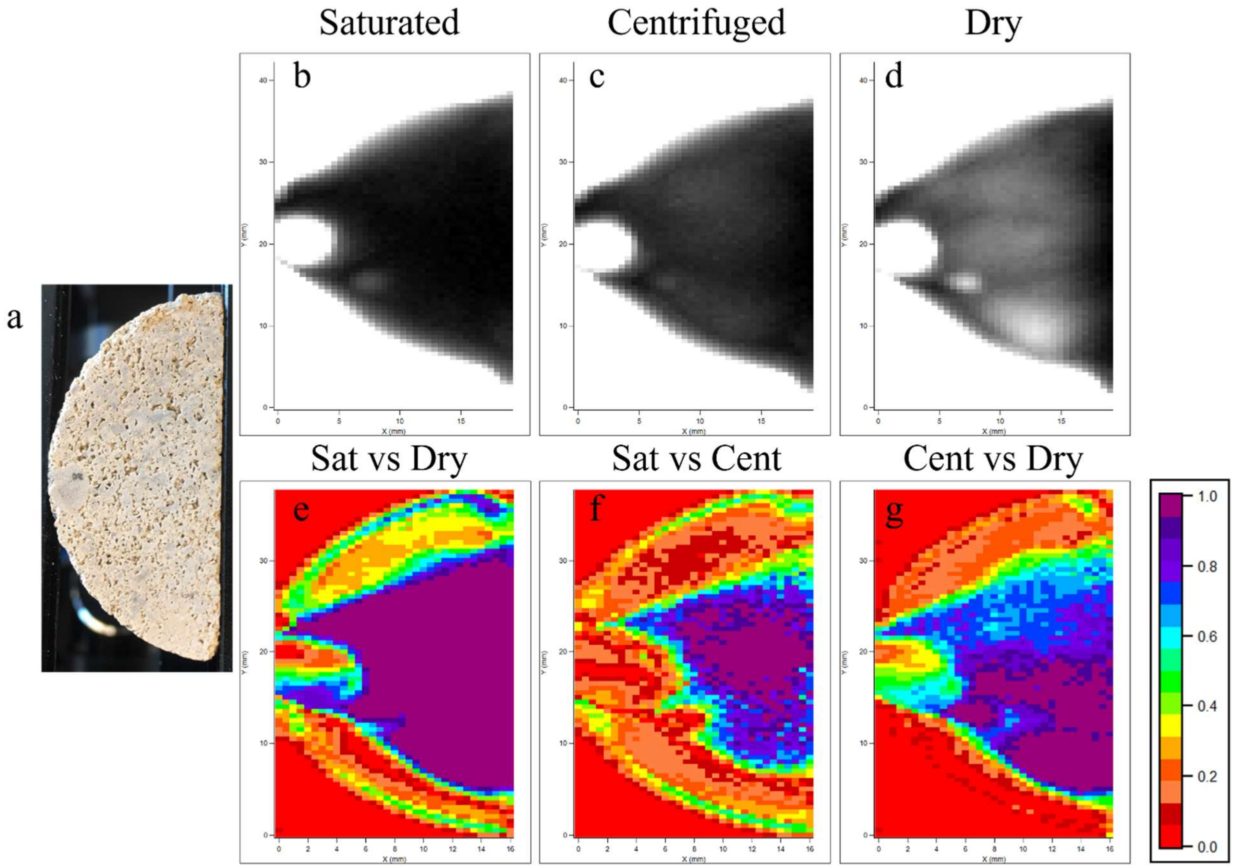

Figure 30. Loss and average loss difference THz images of sample 1 (4 mm thick) from 1 run of the imaging workflow. (**a**) photograph, (**b-d**) loss images of the sample taken at the saturated, centrifuged (at 3140 rpm), and dried stages, and (**e-g**) attenuation difference maps analyzed by comparing the saturated and dried, saturated and centrifuged, and centrifuged and dried attenuation maps to represent the lateral variation of the saturated macropores (larger than 1 μm) and micropores (smaller than 1 μm).

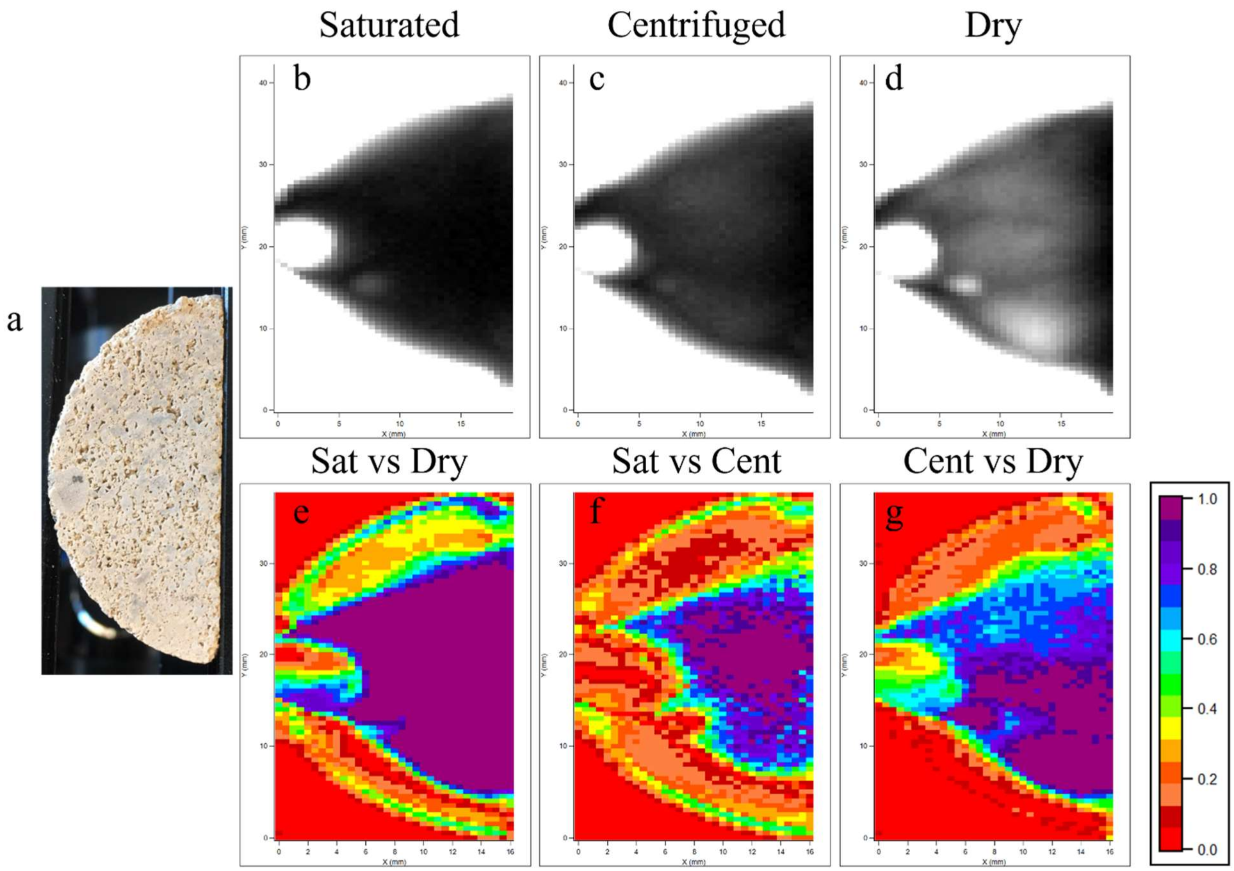

Figure 31. Loss and average loss difference THz images of sample 2 (4 mm thick) from 1 run of the imaging workflow. (**a**) photograph, (**b-d**) loss images of the sample taken at the saturated, centrifuged (at 3140 rpm), and dried stages, and (**e-g**) attenuation difference maps analyzed by comparing the saturated and dried, saturated and centrifuged, and centrifuged and dried attenuation maps to represent the lateral variation of the saturated macropores (larger than 1 μm) and micropores (smaller than 1 μm).

To understand the accuracy of the porosity estimates from the loss map comparisons described by equations (74), (75), and (76), the total porosity, and percent microporosity for both micropore domains measured, were calculated using the mass measurements using equations (66) and (71). The porosity and microporosity of the samples were also measured using the MICP method which was performed on the remaining core plug material not utilized for THz imaging. The estimates of porosity from the THz method for 3 of the 4 runs are presented in Table 5, Table 6, Table 7, and Table 8. Run 1 is not included in any analyses due to issues during the precleaning step which left considerable debris in the pore structure of the samples. 2 mm thick samples are also excluded due to their mechanical instability.

Run #2 $d_p < 1$ µm	Sample 1 (4 mm)	Sample 2 (4 mm)	Sample 3 (4 mm)
$\varphi_{THz,total}$	20%	10%	17%
$\varphi_{THz,\mu pores\_vs\_large pores}$	35%	39%	22%
$\varphi_{THz,\mu pores}$	7%	4%	8%

Table 5. THz porosity estimates from run #2.

Run #3 $d_p < 1$ µm	Sample 1 (4 mm)	Sample 2 (4 mm)	Sample 2 (6 mm)	Sample 3 (4 mm)	Sample 3 (6 mm)
$\varphi_{THz,total}$	14%	14%	10%	15%	6%
$\varphi_{THz,\mu pores\_vs\_large pores}$	35%	44%	22%	34%	48%
$\varphi_{THz,\mu pores}$	5%	6%	2%	5%	3%

Table 6. THz porosity estimates from run #3.

Run #4 $d_p < 0.3$ µm	Sample 1 (4 mm)	Sample 2 (4 mm)	Sample 3 (4 mm)
$\varphi_{THz,total}$	10%	12%	18%
$\varphi_{THz,\mu pores\_vs\_large pores}$	34%	27%	54%
$\varphi_{THz,\mu pores}$	3%	3%	10%

Table 7. THz porosity estimates from run #4. Excluding 6 mm samples.

Run #4	Sample 2 (6 mm)	Sample 3 (6 mm)
$\varphi_{THz,total}$	14%	8%
$\varphi_{THz,\mu pores\_vs\_largepores}$ $d_p < 1$ µm	6%	51%
$\varphi_{THz,\mu pore\_vs\_largpores}$ $d_p < 0.3$ µm	5%	51%
$\varphi_{THz,\mu pores}$ $d_p < 1$ µm	0.8%	4%
$\varphi_{THz,\mu pores}$ $d_p < 0.3$ µm	0.7%	4%

Table 8. THz porosity estimates of 6 mm samples from run #4.

Comparing $\varphi_{THz,\mu pores}$ for $d_p < 1\ \mu m$ and $d_p < 0.3\ \mu m$ with data from mass measurements $\varphi_{m,\mu pores}$, and from MICP measurements $\varphi_{MICP,\mu pores}$, it can be seen (Figure 32, Figure 33, and Figure 34) that this method of estimation gives results consistent with other methods of porosimetry.

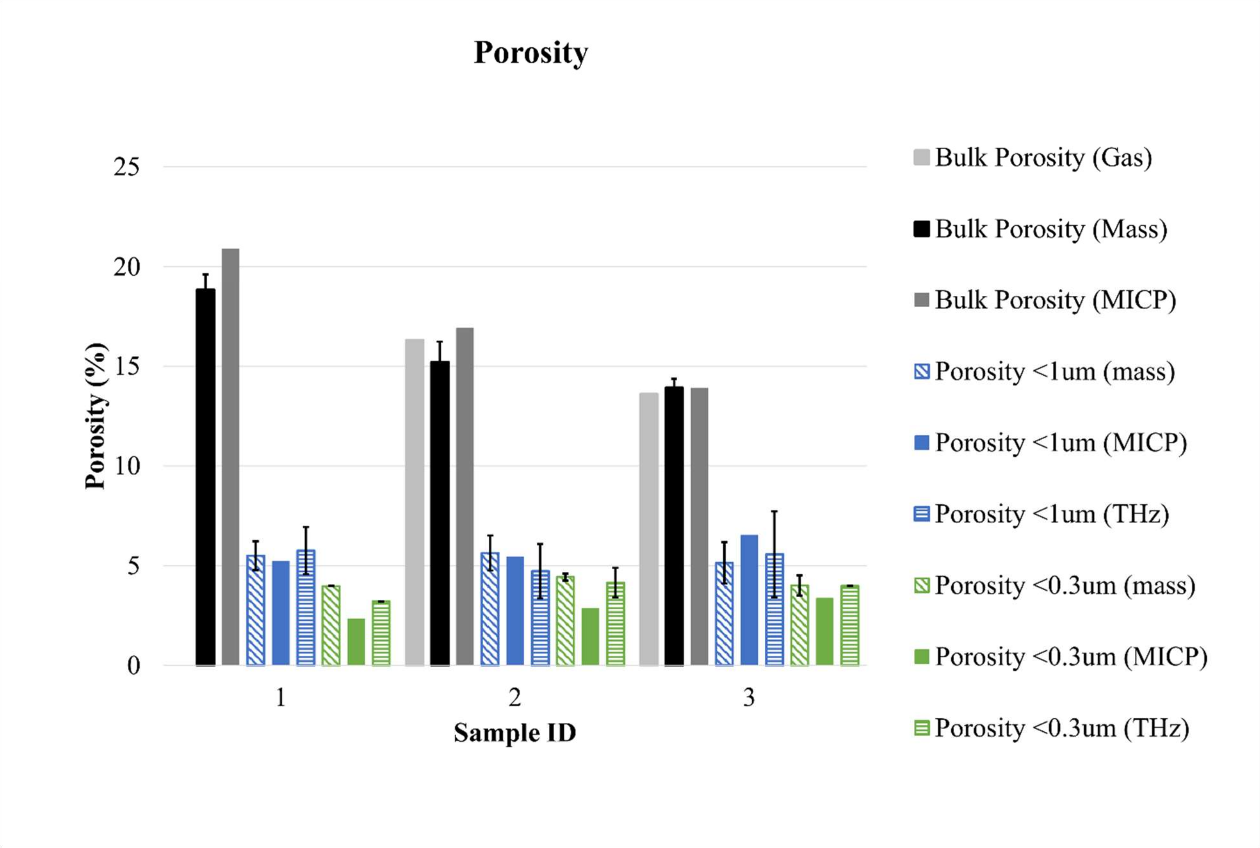

Figure 32. Porosity and microporosity measurements from different methods. Total porosity and the porosity below the two cutoffs $d_p < 1$ µm and $d_p < 0.3$ µm for samples 1-3. Total porosity from gas porosimetry (in light gray) and MICP (in dark gray) are measured using full plugs and half plugs for each sample. Total porosity (in black) is the average of all measurements of the thin half-moon samples used for THz imaging. Porosity below each pore size threshold from mass and THz is the average of data collected on half-moon samples.

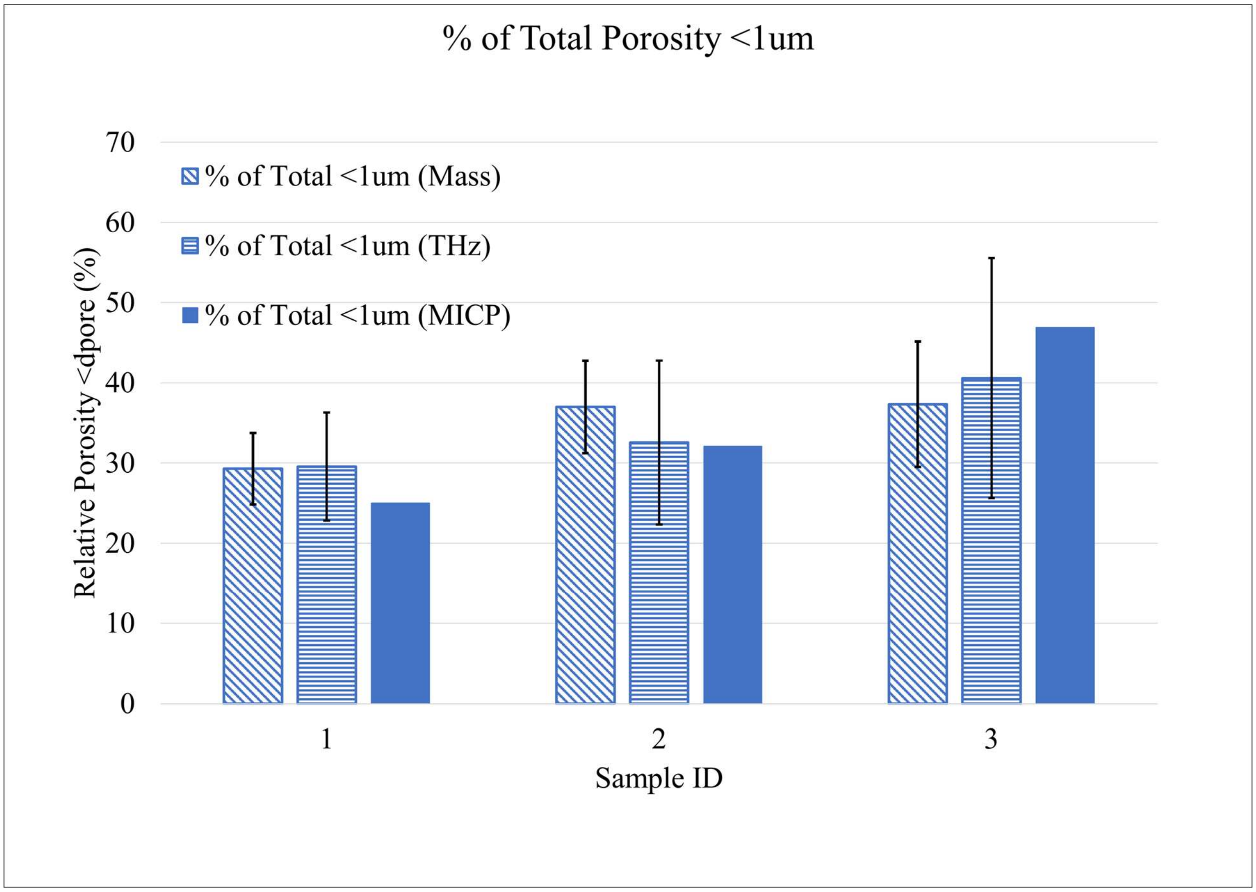

Figure 33. Relative amount of the total porosity to the microporosity for $d_p < 1$ µm.

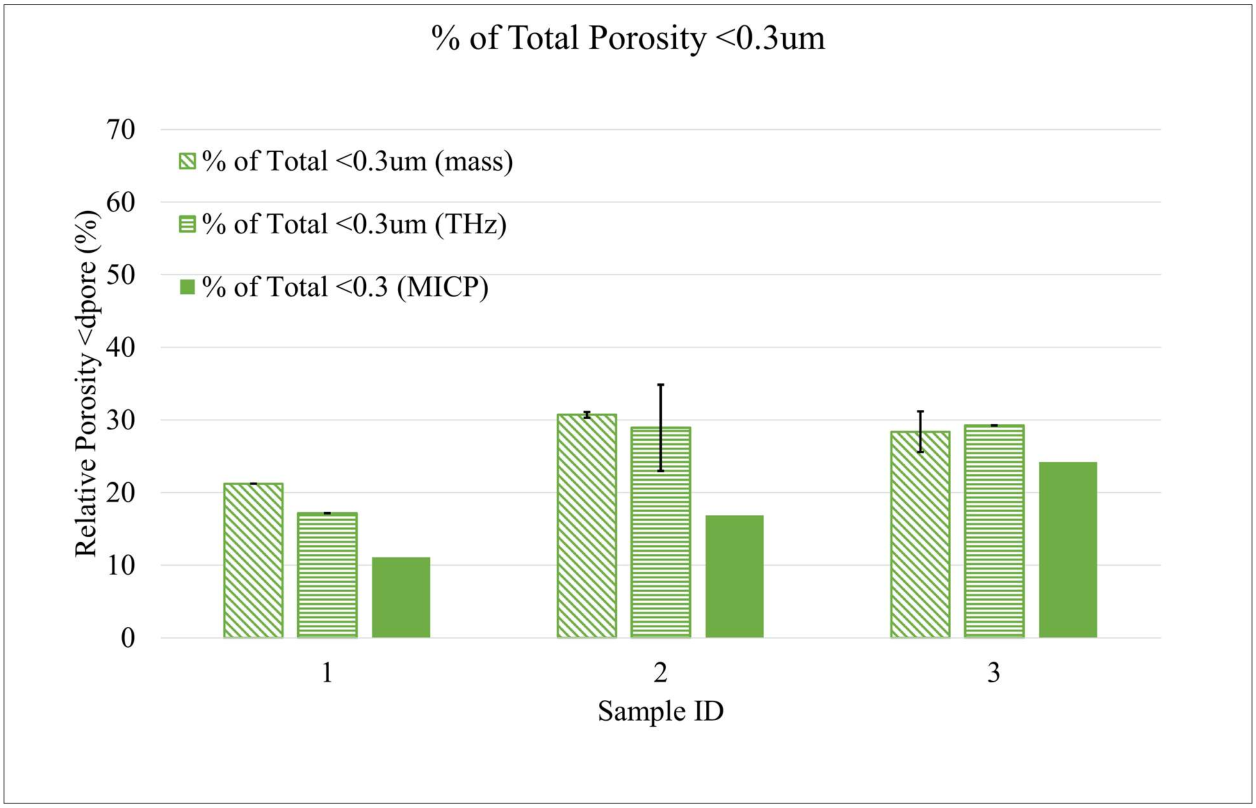

Figure 34. Relative amount of the total porosity to the microporosity for $d_p < 0.3$ µm.

In Figure 32, THz data in graph a comes from equation (74), while the data in graphs b and c are calculated from equation (76). Data from run #4 on sample 3 was excluded from analysis due to it fracturing during centrifugation.

Comparisons of the Porosity maps for $d_p < 1$ µm and $d_p < 0.3$ µm for the three 4 mm samples can be seen in Figure 35, Figure 36, and Figure 37.

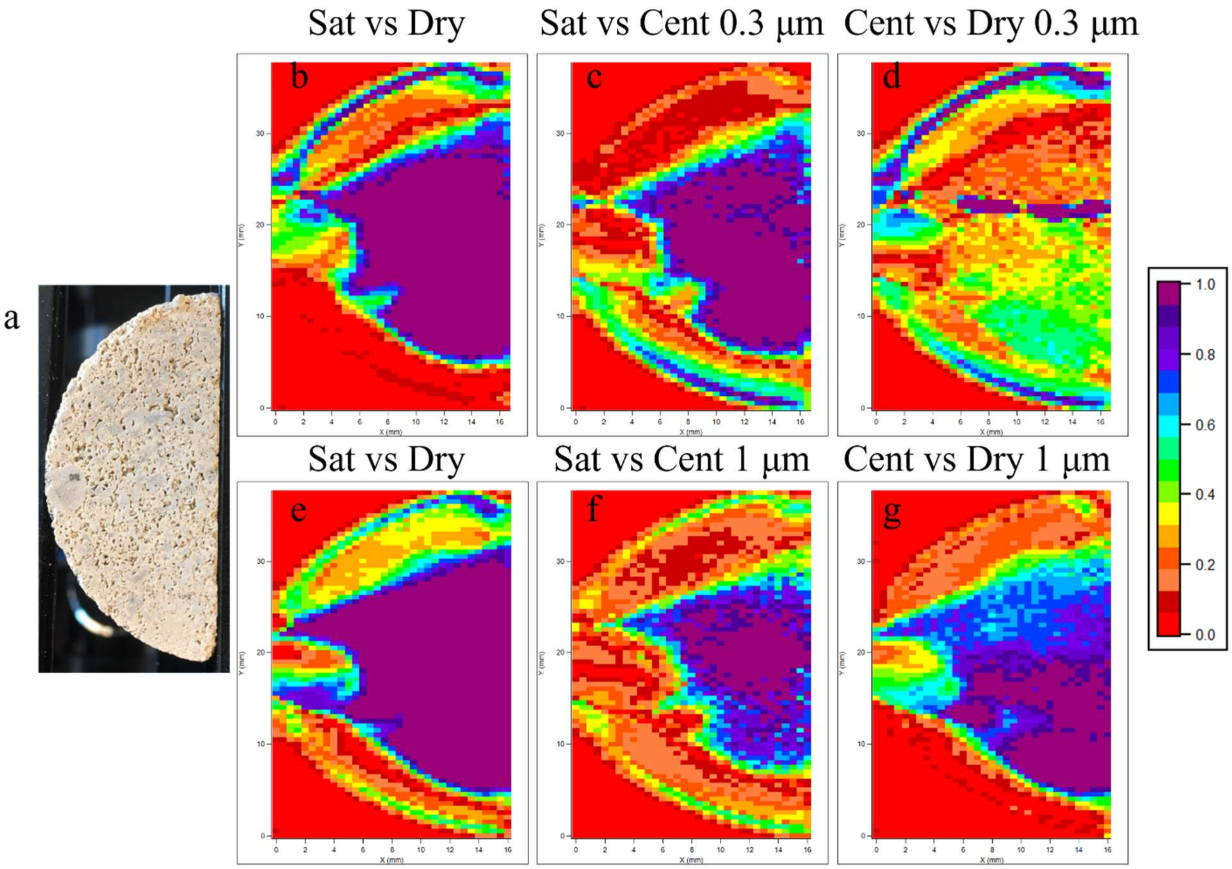

Figure 35. Porosity maps of pores with $d_p < 0.3\ \mu m$ and $d_p < 1\ \mu m$ for sample 1. Note the band of supposed high microporosity in (d) which shows up as a horizontal purple line about halfway up the sample, this is a fracture line where sample 1 broke during the higher speed centrifugation. This fracture was accounted for when setting ROI.

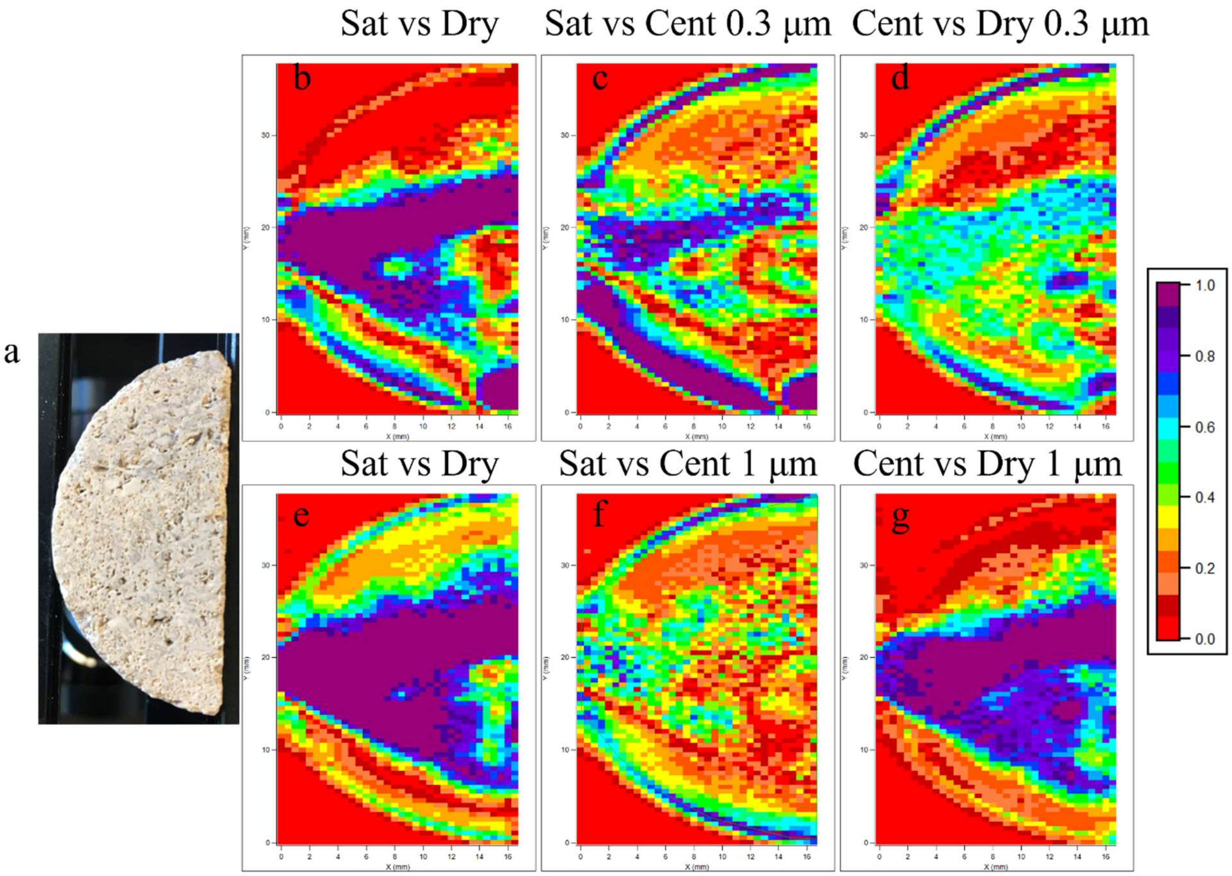

Figure 36. Porosity maps of pores with $d_p < 0.3\ \mu m$ and $d_p < 1\ \mu m$ for sample 2. Note the band of microporosity that appears in (c) but not in the corresponding 1μm image (f). Theoretically this should not happen as any pores picked up in (c) should be seen in (f). This may be due to internal structure breaking down at high centrifugation speeds.

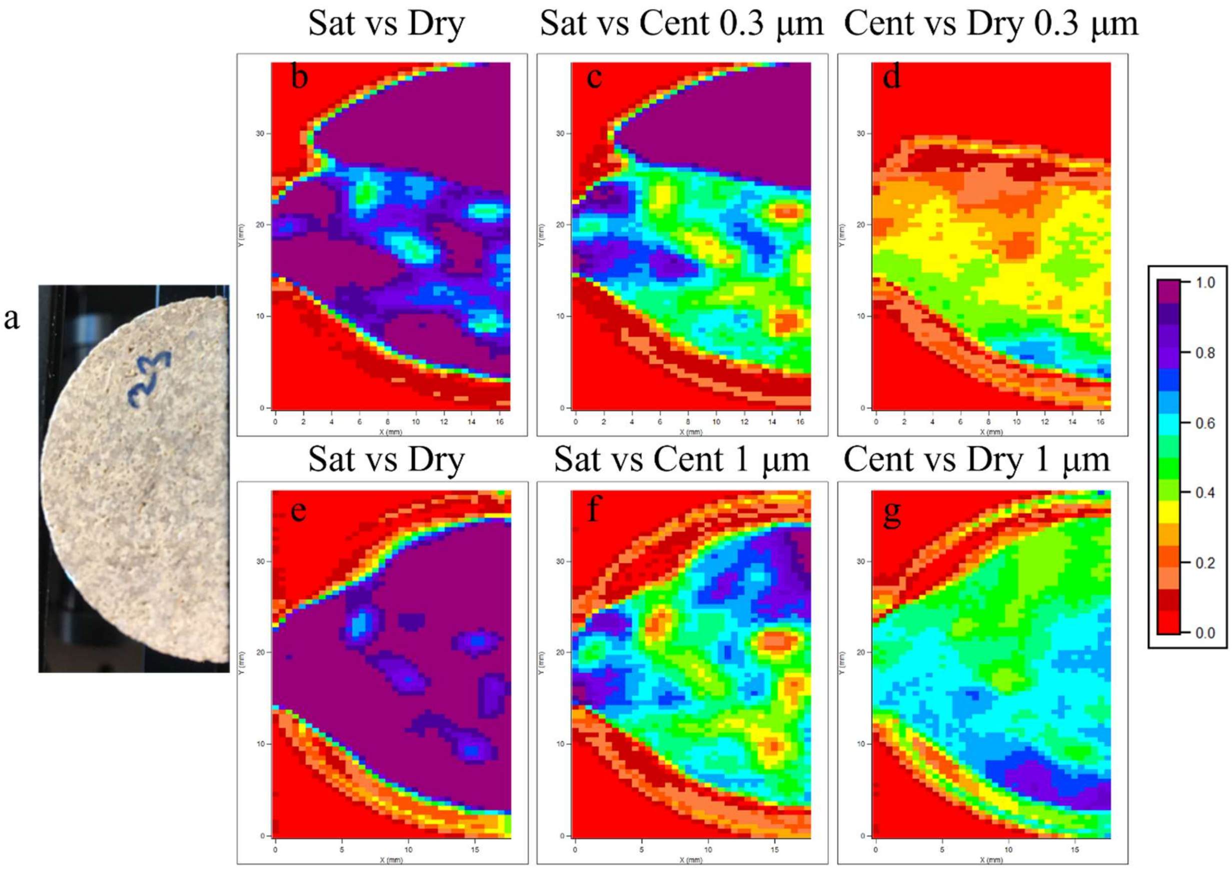

Figure 37. Porosity maps of pores with $d_p < 0.3\ \mu m$ and $d_p < 1\ \mu m$ for sample 3. Note that in (b), (c), and (d), the sample fractured during centrifugation and the top half was shattered so the images are only valid in the lower half.

3.4 CONCLUSIONS AND FUTURE WORK

This project extended previous work on quantifying porosity in carbonates using THz TDS, to include imaging and image analysis. The THz porosity images provide information on the lateral heterogeneity of porosity of different sizes within a sample while consuming little material and taking less than 3 days. The estimates of total and relative porosity from comparing the THz images are in good agreement with industry standard methods and could provide faster preliminary estimates to inform in the field decision making. Below, some limitations of this study are covered and recommendations for further work are given, finally some ideas for paths of possible development are covered.

3.4.1 Limitations of Current Study and Recommendations

The THz loss maps generated in the workflow and the subsequent THz porosity maps are only able to give information on the changes in porosity laterally, this simply the nature of transmission measurements. The effects on the THz radiation throughout the sample are additive, meaning that changes in porosity along the direction of propagation cannot be resolved. For the current application this is not seen as an issue but may become problematic in future applications. To possibly mitigate this issue, I recommend investigating imaging in reflection mode instead. Given that the index of refraction of the rock samples is approximately 1.8 [120] due to them being primarily $CaCO_3$, reflected pulses from water filled pores should be detected later enough in time that their depth can be calculated. This method will have the limitation that only the top layer of porosity will be measured, however.

This study also neglected to consider effects in images due to changes in minerology within the samples. Carbonate rocks are made up of a matrix of $CaCO_3$ with many inclusions of other minerals, to be classified as a carbonate a rock need only to be made up of at least 50% $CaCO_3$. Figure 38 contains a particularly interesting image of a carbonate which includes small fossils of ancient sea life. For this method to be adopted into a core analysis workflow, these variations must be accounted for. One possible way to do this is to carefully study the THz pulses used to construct the dry image. From these pulses the dielectric properties of the sample under measurement can be calculated and based on the spatial variations in the dielectric properties, mineralogical variations may also be measured.

Figure 38. A carbonate made up of spherical Ooids and containing a small, fossilized starfish.[121]

A notable limitation of this method is its sensitivity to sample thickness. This study looked at samples with thicknesses of 2 mm, 4 mm, and 6 mm. The 2 mm samples were not mechanically robust enough to withstand any centrifugation without fracturing, causing their images to be too inconsistent to be analyzed. The thinner samples do have the advantage that there should not be much variation in porosity along the direction of the beam propagation so I recommend trying to run 3 mm samples through this workflow and see if they can withstand centrifugation.

The 6 mm samples were at the functional limit of sample thickness with the transmission through them at the saturated state being just above the noise floor for the TDS system. This issue could be helped by increasing the number of averages at each pixel throughout the image, this will come at the cost of longer imaging times but if thicker samples are of more interest it will have to be done.

The 4 mm samples were a good balance in thickness, with their saturated state still having good transmission at 2 averages per pixel and they were thick enough to withstand the slower centrifugation speed. Samples 1 and 3 did fracture at the higher centrifugation speed, however.

Another concern with sample stability is the effect that repeated wetting and drying has on the structure of the samples. The $CaCO_3$ is soluble in water so with each subsequent run, the samples measured were slowly dissolving. The rate and location of this dissolution were not considered in this study and may account for some variability in the results.

The study also did not consider the effects that closed pores could have on the measurements. Closed pores are pores which exist within a sample but are not connected to the overall pore structure and as a result cannot be filled with water during the saturation step. These pores will still be measured when using MICP so this may explain some of the difference in porosity measured using THz and MICP.

With one possible advantage that this method of porosimetry has being fast turnaround times, focus should be placed on seeing what steps can be eliminated to save time. The preprocessing that takes place before even the precleaning step is one step that could possibly be eliminated. When the cores are taken from the well, they are muddy and filled with a mixture of oil and salt water and a complex cleaning process is employed before they are sent for testing [122]. With this method simply requiring the presence of some contrast material filling the pores of a thin sample, it may be able measure porosity in uncleaned core samples. Oil and saltwater present in the pores will still absorb the THz radiation stronger than the surrounding rock so their presence in a sample can still be mapped. This would be a significant development in core sample analysis and could lead to the adoption of this THz based porosimetry method by the oil and gas industry.

3.4.2 Application of Effective Medium Theory

As a recommendation for future studies working to further develop this method of porosimetry, I recommend building effective medium models to predict the transmission through these samples. To do this some of the core material would need to be pulverized into a powder and compressed into a pellet to get the relative permittivity ε of the rock. Using this and the known relative permittivity of air and the relative permittivity of liquid water from the 3D Debye model, a three-material effective medium can be modeled as a function of water content. This could help with the issue of the unresolvable porosity along the direction of propagation as the effective medium model will predict water volume filled pore and empty pore volume based on the measured transmission. So, in a case such as that in Figure 39 an effective medium model could predict the volume of water within the cross section. This could also increase sensitivity to smaller micropores such as those found in shale. An application similar to this is discussed in great detail in the following section.

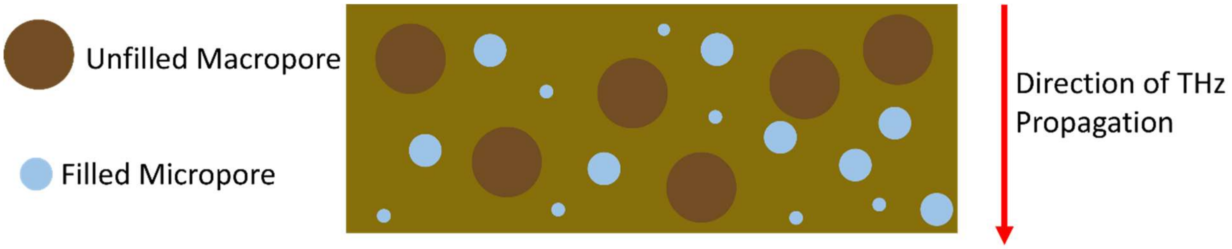

Figure 39. A depiction of the varying porosity within a sample along the direction of THz propagation.

4 TERAHERTZ FOR VOLUMETRIC MOISTURE SENSING

This section serves to introduce and cover one of the two main projects involved in this work. This project is part of a larger effort by the Center for Advanced Research in Drying at WPI and the University of Illinois at Urbana Champaign (UIUC) and sponsored by the United States Department of Energy (DOE). The goal of this work is to develop a novel volumetric moisture sensor based on low bandwidth THz spectroscopy, for implementation on the Smart Dryer testbed at WPI. The primary objective was to develop and implement a moisture sensor able to measure the moisture content of a sample within 2% accuracy. The samples of interest are hand sheets of paper made to the Technical Association of the Pulp and Paper Industry (TAPPI) standard T 205 [123]. The secondary goal of this project was to develop a model and corresponding workflow by which moisture calibration models for sensors operating over a larger bandwidth can be calibrated. If successful, this novel method of moisture sensing could offer benefits over current industry standard technology.

4.1 BACKGROUND

In the United States, industrial drying consumes approximately 12% of the total end-use energy used in manufacturing [124], this is equal to over 300 billion kilowatt hours (kWh). In their Quadrennial Technology Review in 2015 the Department of Energy found that through research and development of novel drying techniques, this energy consumption could be reduced by 40%. These drying techniques include infrared heating [125], specialized impinging jet nozzles [126], ultrasound [127], and dielectrophoresis [128].

4.1.1 The Smart Dryer at WPI

To study these technologies and their possible interplay in a setting analogous to that of an industrial dryer, the Center for Advanced Research in Drying (CARD) was sponsored by the DOE and the Massachusetts Clean Energy Commission (MassCEC) to construct a “Smart Dryer” testbed. This testbed would be based on a modified industrial oven from Reading Bakery Systems and would feature modifiable drying zones where different technologies could be placed within the oven, allowing for the oven to be configured in many ways and combining multiple drying techniques. Figure 40 shows a computer rendering of the smart dryer.

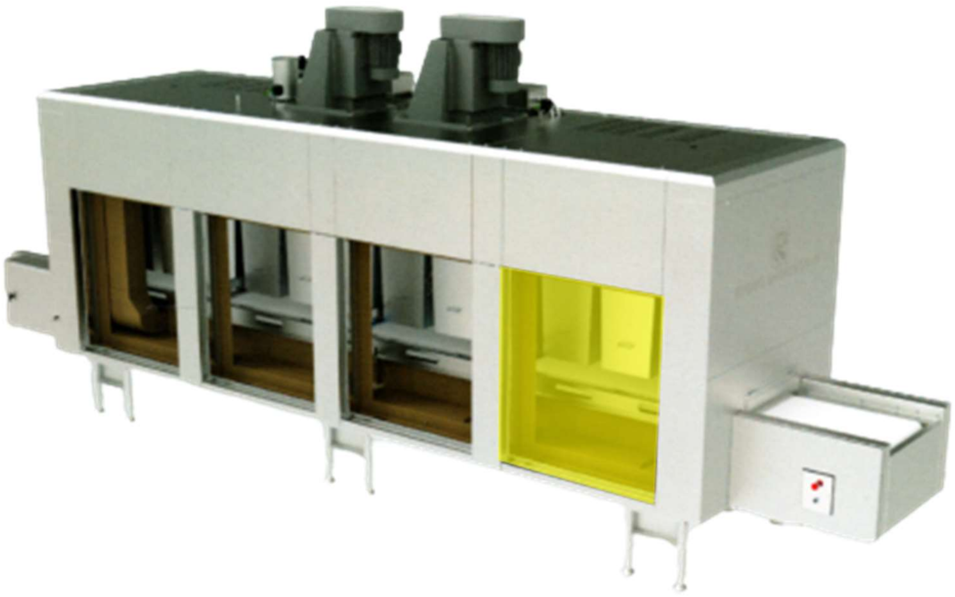

Figure 40. Computer rendering of CARD’s smart dryer at WPI. The area highlighted in yellow is one of 4 configurable drying zones within the dryer.

The vision for the smart dryer is that engineers and scientists from CARD and its member companies will be able to experiment with and develop novel, energy efficient drying methods. To aid in this development, an artificial intelligence built into the dryer, will be monitoring many parameters of the experiment such as dryer energy draw, belt speed, airflow, zone temperature, and the incoming and outgoing moisture content of the sample being dried. From these parameters, the AI will be able to measure the energy efficiency of an experiment and make recommendations for future experiments and predict their outcomes.

For the AI to function properly, it must have as accurate data as possible during an experiment. Most of the data that the AI needs can simply be measured using technology already built into the dryer but for sample moisture content measurements, other technology must be developed and incorporated. Ideally a moisture content meter would be non-contact so as to not influence the drying of a sample, it would be able to be operated in both line and batch processing modes, provide accurate volumetric moisture measurements, fit into the established layout of the dryer, be compatible with many samples, and work either throughout the dryer or at both the inlet and outlet. Three methods of moisture sensing are being developed as part of the smart dryer project; they are: A graphene field-effect transistor temperature and humidity sensor, a fiber optic humidity sensor, and a volumetric moisture sensor based on attenuation of a THz beam. This work is concerned with the theory behind, and development of the THz based moisture sensor and subsequent sections will cover this.

4.1.2 THz for Moisture Measurements in Paper

A review of the literature turns up many examples of THz being used to detect water or measure the change in a sample's transmissivity T as a function of moisture content [4, 60, 61, 78, 129-133]. All this work relies on a simple requirement, that the dry sample and water have distinctly different relative permittivities in the THz range. For paper, this requirement is met with $\varepsilon_{paper} = 1.56$ and $\varepsilon_{water} = 4.89$ at 1 THz. Therefore, even small inclusions of water will result in detectable changes in the paper's effective permittivity. THz offers a very attractive platform for the development of new moisture sensors as it balances the high moisture sensitivity of the NIR method with the high transmissivity of the microwave method. Resulting in a sensitive, volumetric moisture meter, which does not need to infer internal moisture content as a function of surface moisture. THz also has the benefit of not being significantly impacted by scattering due to the paper samples as scattering typically comes from features of the size 0.1 λ.

Many of the examples in the literature utilize THz TDS in transmission mode for measuring the moisture content of a sample due to the techniques ability to instantaneously provide broadband data which can be used to calculate the relative permittivity of a sample. These measurements can then be related to moisture content through either empirically derived look up tables or theoretically derived material models. In Banerjee et.al. [129] hand sheets of paper were measured with THz TDS and gravimetrically to relate the phase shift of the pulse and relative optical density, $\log_{10}\frac{P}{P_{ref}}$, to the moisture content of the sample. These two relationships are frequency dependent and were calculated at all the frequencies within the THz pulse. Figure 41 shows comparisons between the moisture content and the relative optical density measured at 0.6 THz. These experiments showed a close correlation between both phase shift and optical density to moisture content, with some deviation in the phase shift for high moisture content. This deviation may be caused by the significant top surface reflections from the sample which were not considered in the study which produced this graph.

Hattori et.al. [131] examines two types of premanufactured paper and checks the validity of the Clausius-Mossotti method in estimating the frequency dependence of the refractive index and attenuation coefficient of a moist sample. The results of this work are shown in Figure 42 and they suggest that the implementation of an effective medium theory could be used to predict moisture content based on THz measurements. The study does not, however, offer any analysis of the accuracy of the effective medium model as it only picks a moisture content which gives the best fit of the Clausius-Mossotti model.

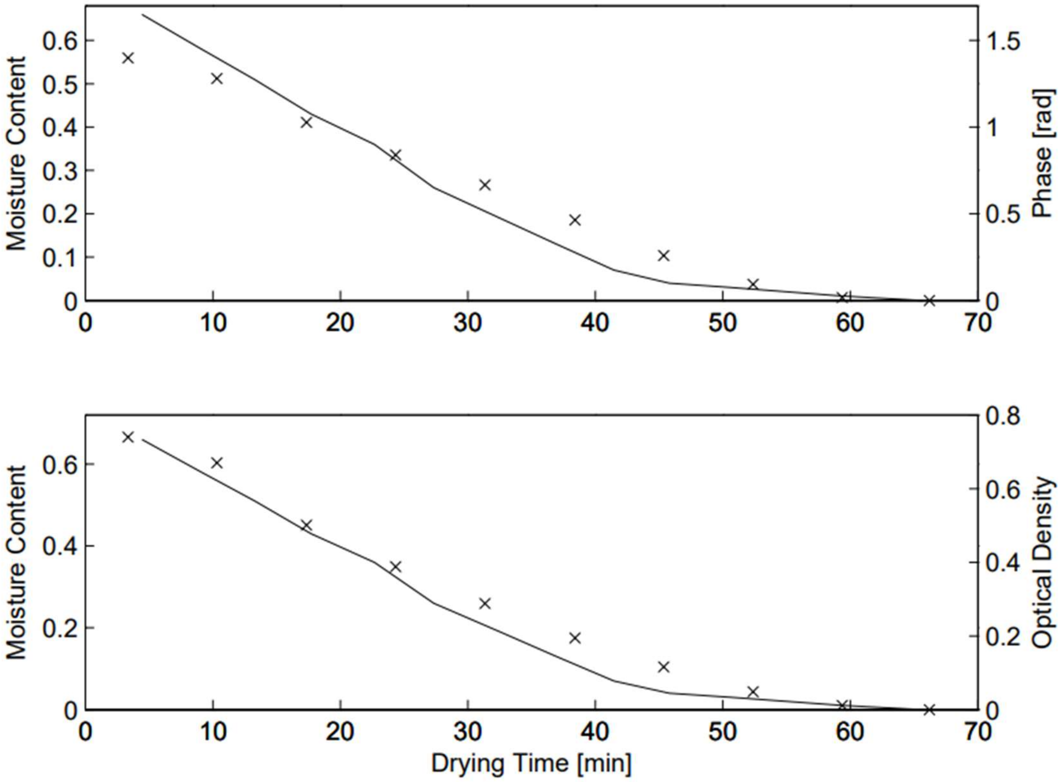

Figure 41. Measures of the gravimetric moisture content, shown as the solid line, the phase shift, shown as x's in the upper panel, and the relative optical density of the sample shown as x's in the lower panel. THz data was taken using TDS and phase shift and optical density were measured at 0.6 THz. Sourced from [129].

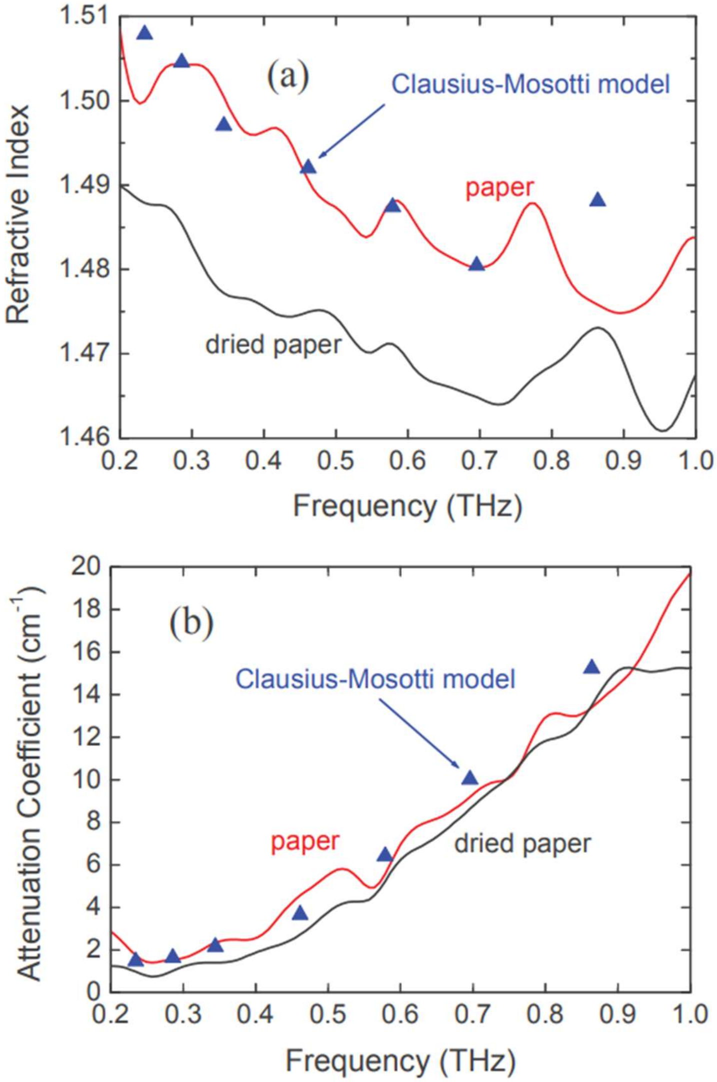

Figure 42. Spectra of the (a) refractive index and (b) attenuation coefficient of copy paper left in an ambient environment (red) and dried in an oven (black). Estimates of the refractive index and attenuation coefficient from the Clausius-Mossotti model assuming a water content of 1.7% are shown as triangles. Sourced from [131].

A more rigorous study by Mousavi et.al. [130] sought to measure both the moisture content and thickness of a paper sample. The authors applied Bruggeman's model to estimate the moisture content of a sample based on its transmission amplitude T. This study also introduces the use of a double Debye model to estimate the frequency dependent relative permittivity of liquid water ε_w.

These studies all provide a significant foundation for the development of implementable moisture sensors but lack some fundamental design considerations. The above work was all concerned with proving the feasibility of THz moisture sensors and consisted of measurements done in laboratory environments where measurement geometries could be designed for ease of measurement. To move this technology closer to the point where it can be adopted by industrial customers, work must be done to understand and design for industrial environments where optimal measurement geometries cannot always be achieved. Work must also be done to develop sensors operating on more cost-effective platforms than time-domain spectrometers. Although much of the previous work has been done using TDS, the complexity of these systems makes them impractical for implementation and the ultrawide bandwidth is not necessary when predetermined samples.

A report by Vassilev et.al [61] describes the development of an FMCW moisture sensor operating a 200 GHz with a bandwidth of 1 GHz, its overall design can be seen in Figure 43. It was designed for implementation in an industrial offset printing process where the paper is passed between printing and drying drums, allowing the sensor to have access to both sides of the paper. This allows the sensor to operate in transmission mode and monitor the attenuation of the transmitted signal as paper passes through the optical path. The measured attenuation is compared to a lookup table which relates attenuation to moisture content and the moisture content is reported. To construct the lookup table a sample was measured across the expected range of moisture contents in a laboratory. The development of this sensor marks an important step forward in THz moisture sensing. However, use of the lookup table lacks scientific rigor and could introduce errors in moisture measurements while artificially limiting the operable moisture range of the sensor.

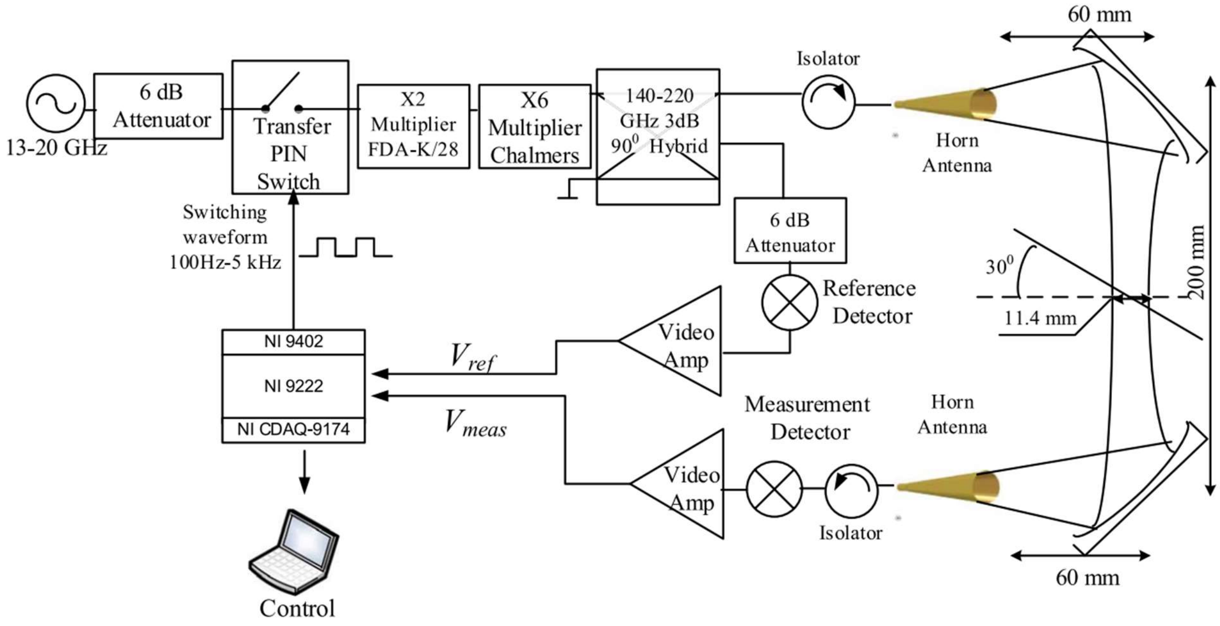

Figure 43. A block diagram of the moisture sensor presented in Vassilev et.al. based on a voltage-controlled oscillator combined with frequency multipliers and conventional microwave circuitry. The sensor is offset from the sample by an angle of 30° to prevent interference from standing waves. Sourced from [61].

4.1.3 Sensor Design Considerations

For the moisture sensor to be designed implemented on the smart dryer, an augmented version of the sensor presented by Vassilev et.al. will be used in conjunction with effective medium models to calculate moisture content from measured signals. The primary augmentation will be in the layout of the optical path. In all the previously covered papers, experiments were done in transmission mode which requires both sides of the sample to be accessible to the optical path. In the case of the smart dryer, hand sheet samples will be pressed onto couch plate made of 316 stainless steel, as described in the TAPPI standard [123], and run through the dryer on a chain mesh conveyor belt. This makes operation in transmission mode impossible, however the highly reflective couch plate allows for operation in reflection or two-pass transmission mode. This mode, shown in Figure 10, presents unique challenges which will be covered in later sections.

4.2 EXPERIMENTAL DESIGN

To begin the design of the moisture sensor for the smart dryer, an operating frequency must be chosen. This decision must consider the sensitivity to moisture content at a frequency as well as the cost and availability of components operating that frequency. The sensor will ideally consist of off the shelf components and not rely on costly and fragile laboratory equipment as well as having a small footprint and be easy to operate. Equipment cost and availability can be found by simply searching the catalogues of RF electronics suppliers, but understanding moisture sensitivity is much more involved. With the planned sensor operating in reflection or two pass transmission mode and its beam being incident to the sample, the measured signal will depend on both the transmissivity and reflectivity both of which depend on moisture content and frequency. In order to make an informed decision on the operating frequency, models for the reflectivity and transmissivity of a sample over a wide range of moisture contents and at many frequencies must be made. These models can be made through the application of effective medium theory.

4.2.1 Building the Effective Medium Models

At normal incidence, when an electromagnetic wave travelling through air encounters a medium, its reflectivity R can be written using the Fresnel equations in terms of the refractive index n and extinction coefficient κ [64] seen in equation (77).

$$R = \frac{(n-1)^2 + \kappa^2}{(n+1)^2 + \kappa^2} \tag{77}$$

The transmissivity is then found by combining the relation that $T + R = 1$ for lossless media with the beer lambert law for lossy media and a $\frac{1}{\sin^2(n\omega d/c)}$ term to account for interference, this is seen in equation (78). Where the absorption coefficient α is related to the extinction coefficient κ as $\alpha = \frac{2\kappa\omega}{c}$, c is the speed of light in a vacuum, d is the thickness of the sample, and ω is the angular frequency $\omega = 2\pi\nu$.

$$T = \frac{(1-R)^2 e^{-\alpha}}{(1-Re^{-\alpha}\ )^2 + 4Re^{-\alpha d}\sin^2\left(\frac{n\omega d}{c}\right)}$$

(78)

The refractive index and extinction coefficient are related to the real and imaginary components of the complex relative permittivity following equations (79) and (80) respectively.

$$\varepsilon' = n^2 - \kappa^2$$

(79)

$$\varepsilon'' = 2n\kappa$$

(80)

With the proposed sensor operating in reflection or two pass transmission mode (hereafter referred to as two pass transmission mode), equation (78) undergoes the following simple modification where the thickness of the sample d is replaced with twice the thickness of the sample $2d$. Neglecting the small contribution due to surface scattering which should not change with moisture content and assuming a constant reflection from the steel backing plate of the sample, the signal read at the sensor I is seen in equation (81).

$$I = I_0(T(\mathrm{MC}) + R(\mathrm{MC}))$$

(81)

Here I_0 is the signal read when the beam is just reflected off the steel plate and MC is the moisture content of the sample.

From a measurement of the relative permittivity of a sample in its bone-dry state i.e. $\mathrm{MC} = 0$ and with an estimate of the relative permittivity of liquid water at a particular frequency and temperature from the three-parameter Debye model seen in Figure *44*, models of the measured signal at the sensor as a function of frequency, temperature and moisture content can be made. As a weakly interacting, nonpolar, dielectric the complex permittivity is constant over most of the electromagnetic spectrum. Therefore, a fit can be made from measurements of the two components of the relative permittivity over a small bandwidth which can be used to estimate these values over a large bandwidth.

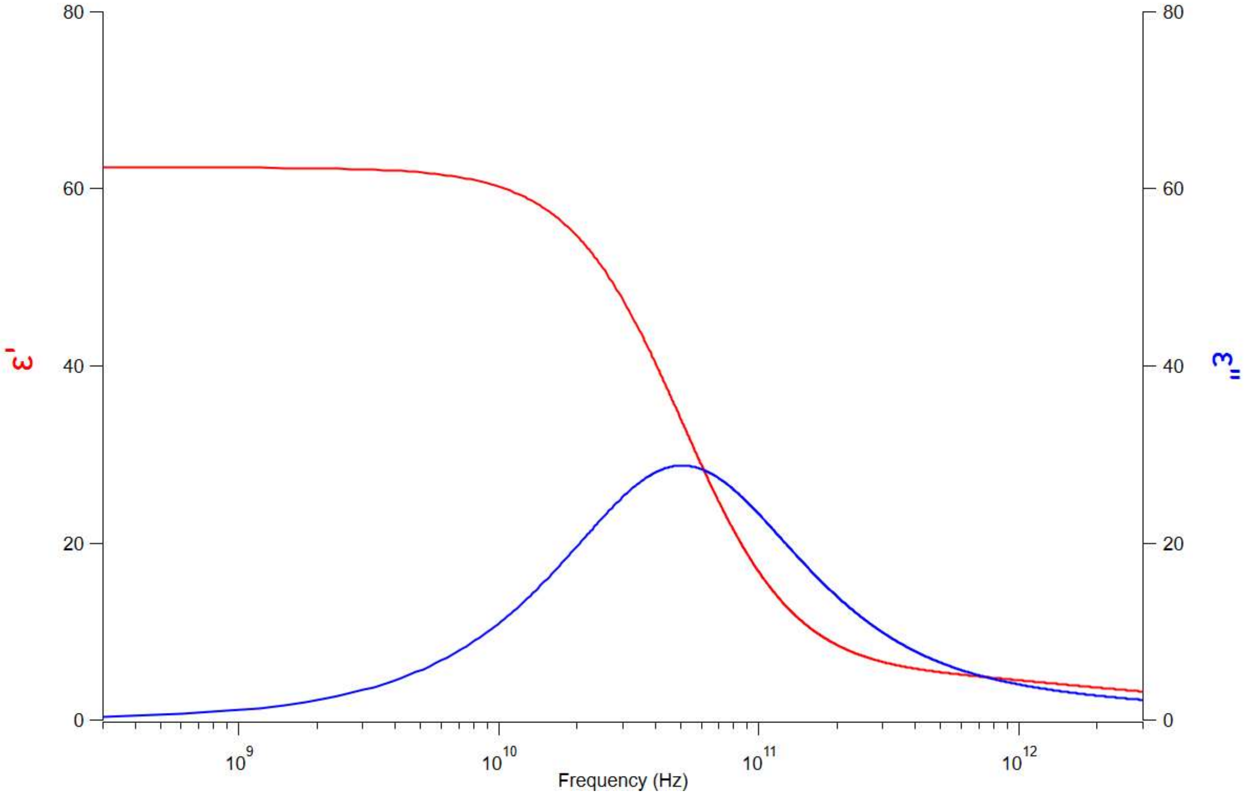

Figure 44. A graph of ε' (red) and ε'' (blue) of liquid water from the three-parameter Debye model.

The relative permittivity of a sample as a function of moisture content can be modeled using effective medium theory, which models a sample of wet paper as a mixture of liquid water and dry paper. These effective medium models, built for different frequencies and temperatures will provide input complex permittivity data for the sensor signal models. Both Bruggeman's and Looyenga's models were used to build material permittivity models.

The choice of using both models was made due to the geometrical assumptions made by both models. As covered in an earlier section, Bruggeman's model, seen in equation (46), assumes the mixture consists of a continuous host material with spherical inclusions of a second material. This model seems consistent with the case for paper with very high moisture content where the bulk of the water is present in relatively large inter-fiber pores. In these inter-fiber pores, the shape of the water will be governed mostly by surface tension, leading to mostly spherical inclusions. Looyenga's model on the other hand, seen in equation (57) assumes the material to be a continuous mixture of the host and intrusion material and makes no assumption on inclusion geometry. These assumptions seem consistent with low moisture content paper where the bulk of the water exists as so called "associated water" and is present in intra-fiber pores which are much smaller than inter-fiber pores. A simple diagram of these pores is present in Figure 45.

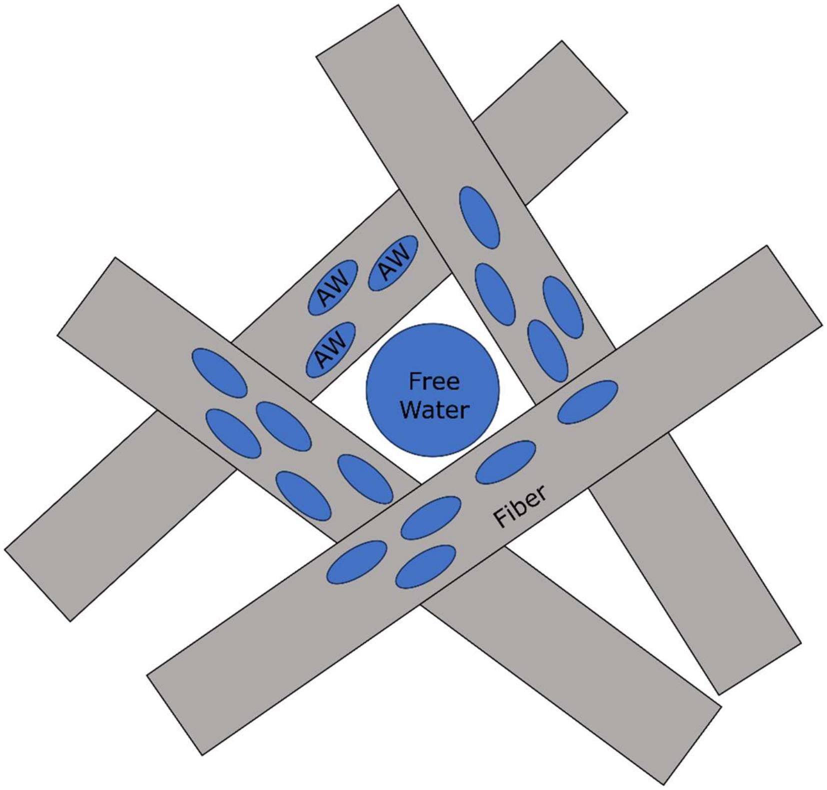

Figure 45. A simple diagram of the two pore domains and the phase of water present in those domains. In this diagram AW stands for associated water.

The models described above were built for copy paper within the frequency range from 60 GHz to 2 THz and for the temperature range from 10 °C to 100 °C. The lower bound of the frequency range was selected to be 60 GHz because interactions with samples was anticipated to be too low to be effective for sensing, 2 THz was selected as the high cut off due to the high cost of sources and the increased sensitivity to humidity at and above this frequency. The temperature range spans from lower than ambient room temperature to the expected limit of the temperature of liquid water. For the copy paper models the high limit of the moisture content was set at 150% DBMC, this was deemed sufficient as in experiments the paper was never observed reach moisture contents above 120% DBMC. The key assumption made in these models is that the sensor will be operating at standard atmospheric pressure, any significant changes in pressure will influence the properties of the liquid water and impact the accuracy of these models.

The data for the bone-dry sample was taken using a Toptica Teraflash time domain spectrometer from Toptica. The spectrometer has an effective bandwidth from 300 GHz to 2.2 THz. Samples were dried at 100 °C under vacuum in a vacuum oven and then quickly measured in transmission mode on the TDS. Data was then analyzed using nelly, an open source TDS analysis script for MATLAB [134]. From nelly, the terms of the complex relative permittivity were calculated for the paper over the range of the spectrometer. With the expectation that these values will not vary significantly outside of the range of the spectrometer, a fit was applied to both ε' and ε'' to get estimates outside of the measurement range. From the measured data, these values were found to have a sinusoidal variation around a centerline, so they were fit to a sine function, Figure 46 and Figure 47 show the data versus the fit, and equations (82) and (83) show the fitting functions.

$$\varepsilon'_{\text{copy paper}} = 1.5887 + 0.021669 * \sin(-5.5767 * f + 10.373) \tag{82}$$

$$\varepsilon''_{\text{copy paper}} = 0.12159 + 0.038464 * \sin(3.8245 * f + 0.0015464) \tag{83}$$

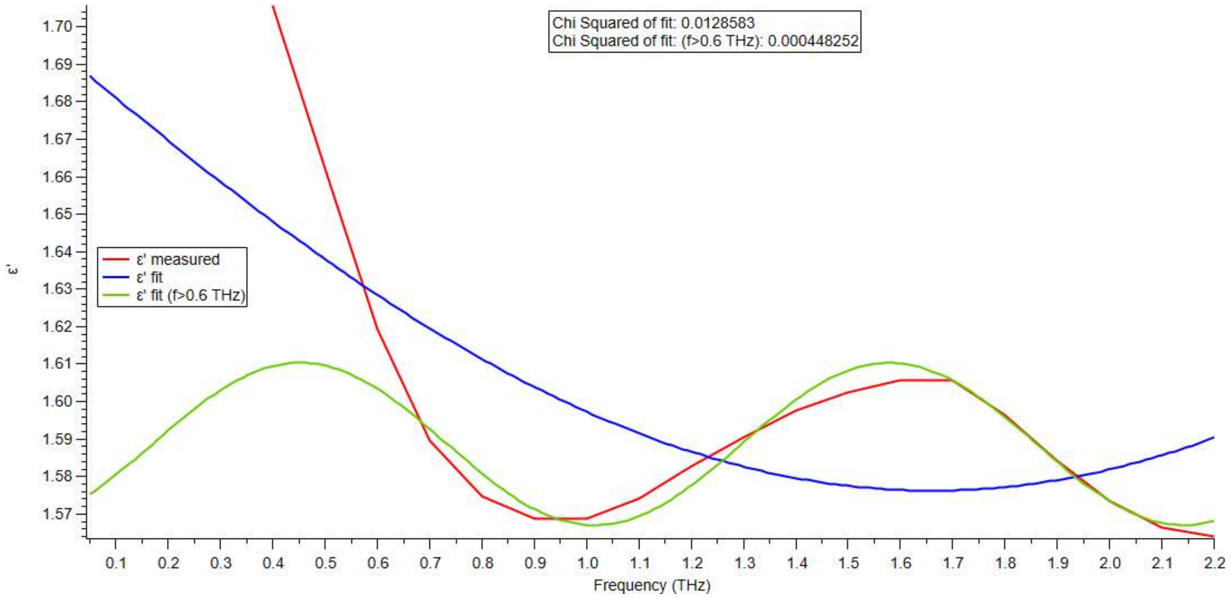

Figure 46. Comparison of measured data for ε' of copy paper shown as the red trace and two sine fits in blue and green. The blue trace is a sine fit applied over the whole range of data while the green trace is a sine fit applied only from 0.6 THz to 2.2 THz.

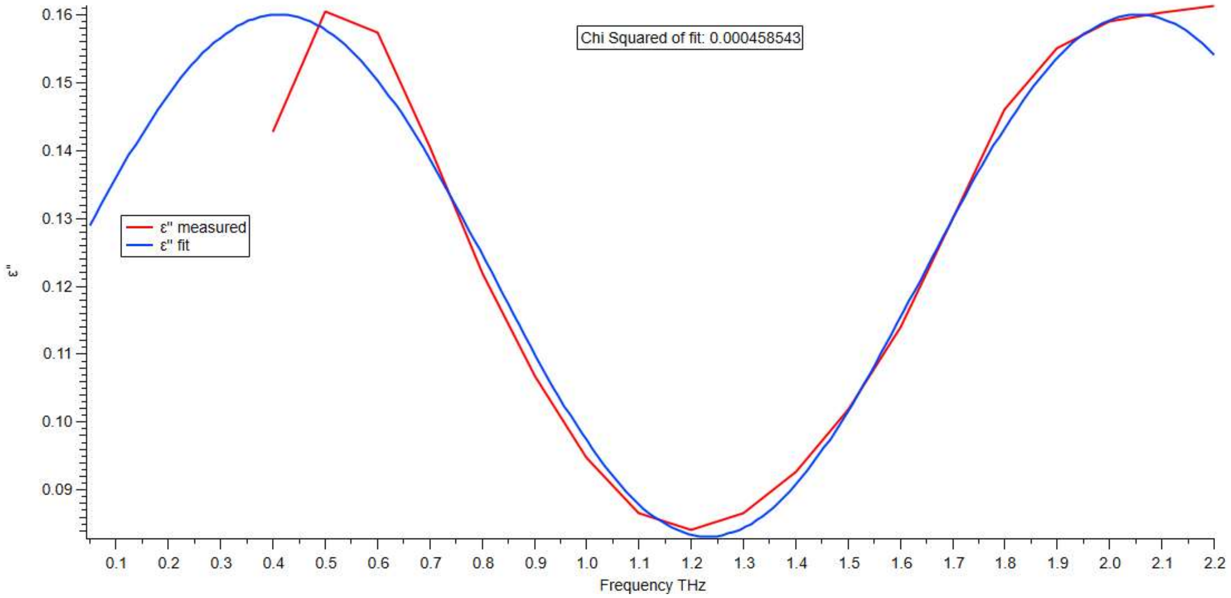

Figure 47. Comparison of measured data for ε'' of copy paper shown as the red trace and a sine fit in blue. This fit was applied over the whole range of data from 0.3 THz to 2.2 THz.

The fits were assessed for accuracy by checking their χ^2 values and observing their trend outside of the measurement area. For ε' the fit over the full frequency range was determined to be unsuitable as its amplitude was too large and its χ^2 was too high, the abbreviated fit looking only at data from 0.6 THz to 2.2 THz was chosen instead. This fit has reasonable amplitude and a much lower χ^2. For ε'' the sine fit over the full frequency range was found to be sufficient as its amplitude was reasonable and it had a very low χ^2. The sinusoidal behavior of the measured permittivity comes from the etalon effect. This effect comes from interference from multiple reflections within the sample. The small amplitude of the sine fit shows that this effect is not particularly strong but it can be factored into the transmission model. For the permittivity model, only the first term of both of the fits, which corresponds to the Y offset of the sine fit, is used.

The last input needed to model the transmission of a sample of copy paper from 60 GHz to 2 THz, from 10 °C to 100 °C, and from 0% to 150% DBMC, is a model for the temperature dependent model for the density of liquid water. This model comes in the form of the Kell equation shown in equation (84) with corresponding coefficients seen in Table 9.

$$\rho_{\mathrm{H_2O}} = \frac{\Big(\big(\big((A*t+B)*t+C\big)*t+D\big)*t+E\Big)*t+F}{1+G*t*1000} \tag{84}$$

Coefficient	Value
A	$-2.8054253 * 10^{-10}$
B	$1.0556302 * 10^{-7}$
C	$-4.6170461 * 10^{-5}$
D	0.007987040
E	16.945176
F	999.83952

G	0.01687985

Table 9. Coefficients for the Kell equation to predict the temperature dependent density of liquid water.

With this final input, the models can be built, and the moisture dependent performance of the sensor can be assessed to choose an operating frequency.

4.2.2 Selecting the Operating Frequency

From the comprehensive sensor model described in the previous section, the operating frequency of the sensor can be selected by analyzing the expected dynamic range of the sensor at different moisture ranges and balancing sensitivity with sensor cost. Two studies were conducted, one compared the expected performance at a fixed temperature over the band of considered frequencies. The other study looked at the effect of temperature at each frequency. Some graphs and a discussion of the results of both studies are found below.

4.2.2.1 Frequency Effect Study

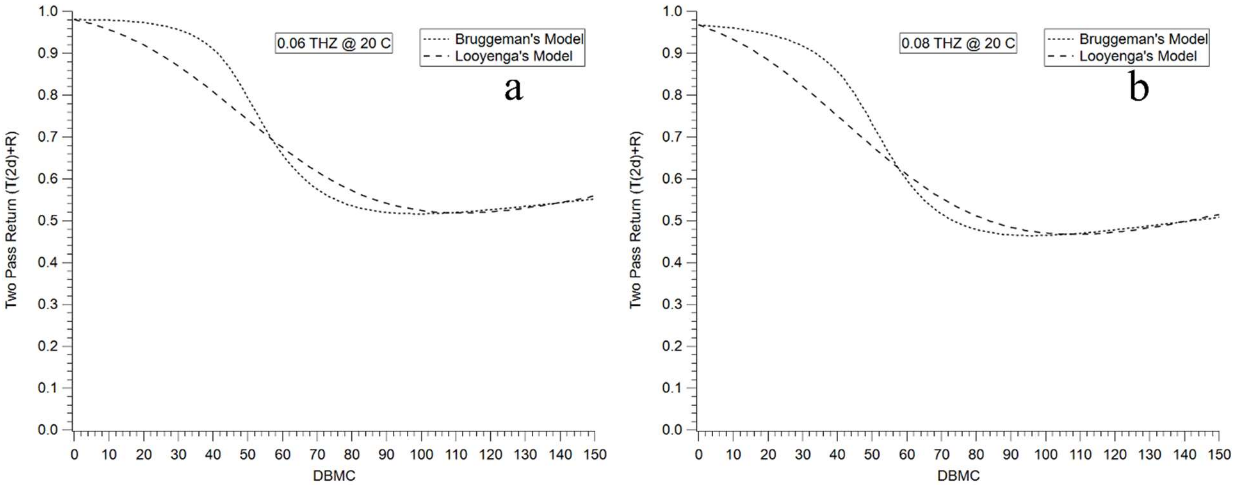

Figure 48. Comparison of 60 GHz and 80 GHz at 20 °C.

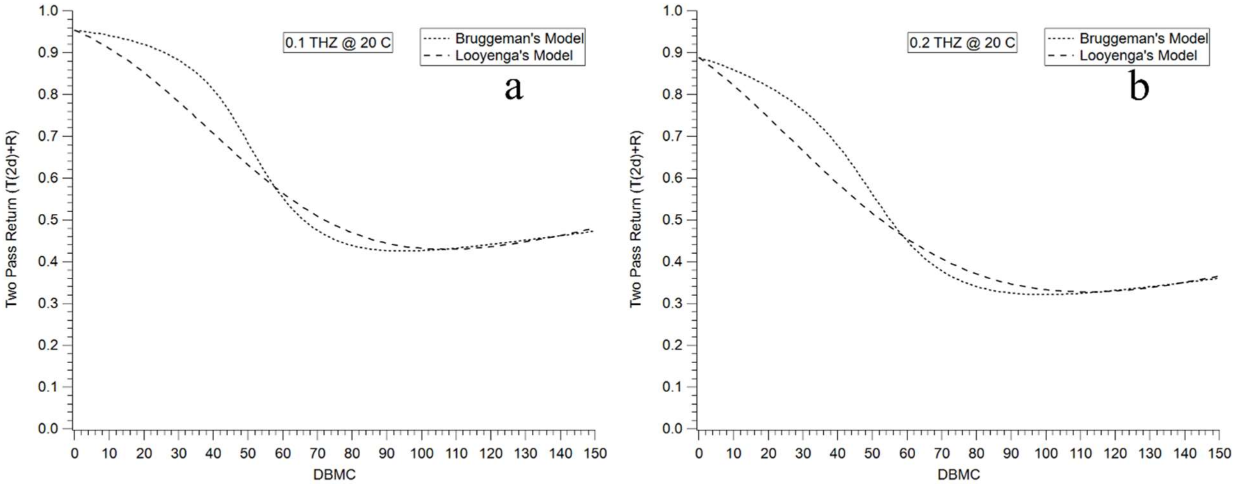

Figure 49. Comparison of 100 GHz and 200 GHz at 20 °C.

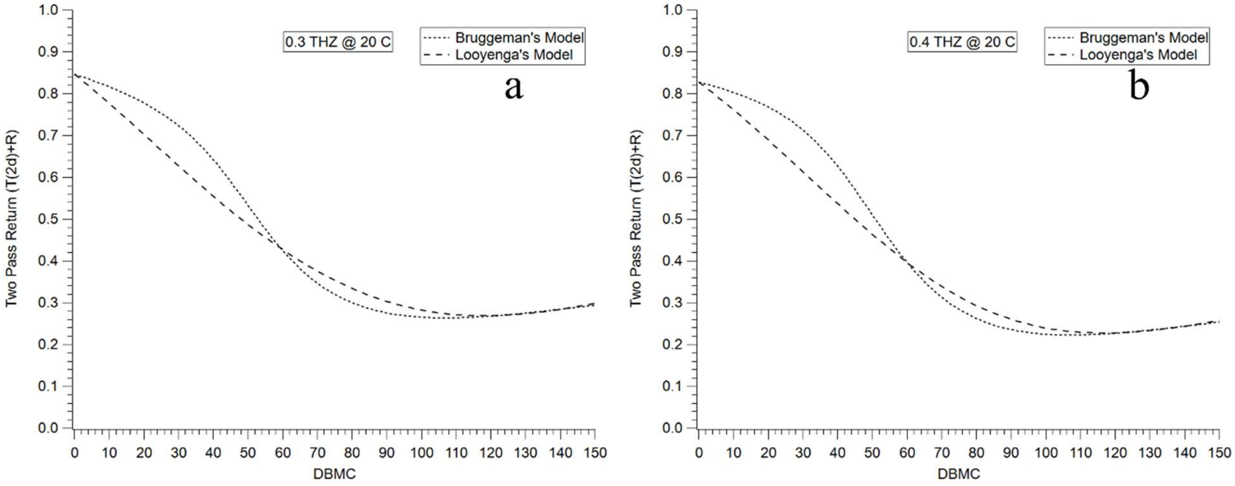

Figure 50. Comparison of 300 GHz and 400 GHz at 20 °C.

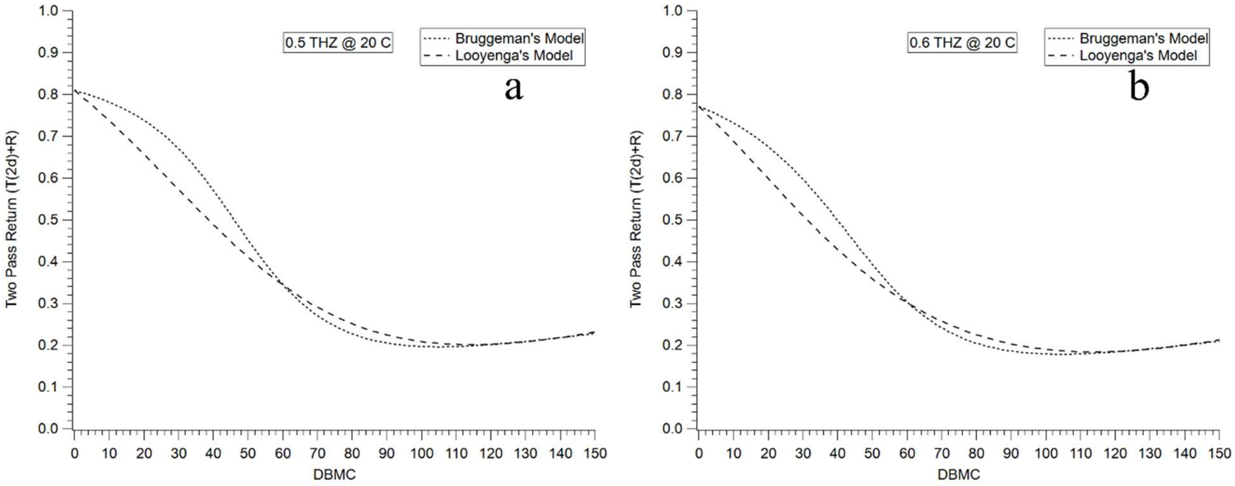

Figure 51. Comparison of 500 GHz and 600 GHz at 20 °C.

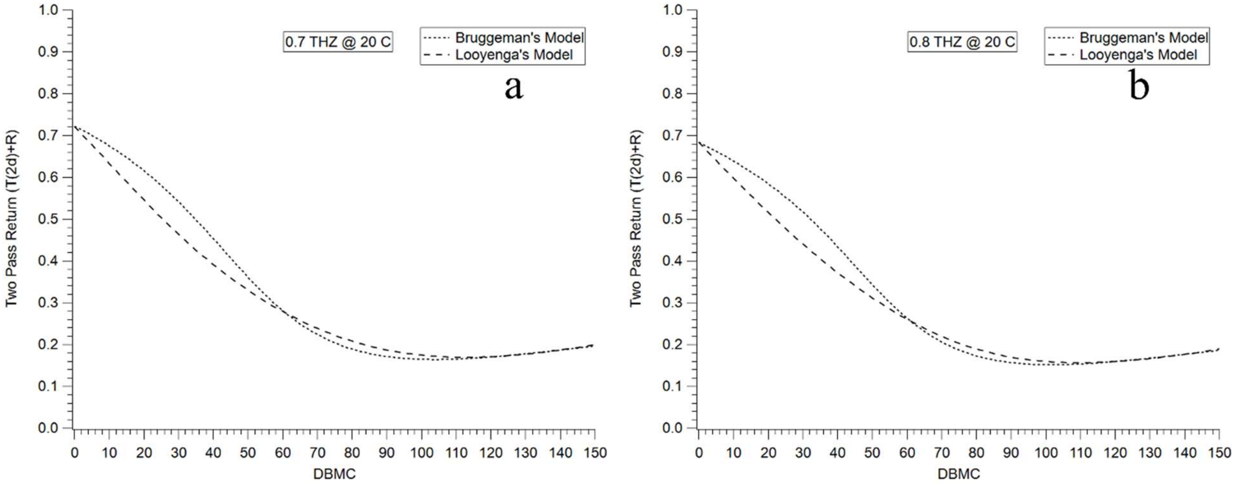

Figure 52. Comparison of 700 GHz and 800 GHz at 20 °C.

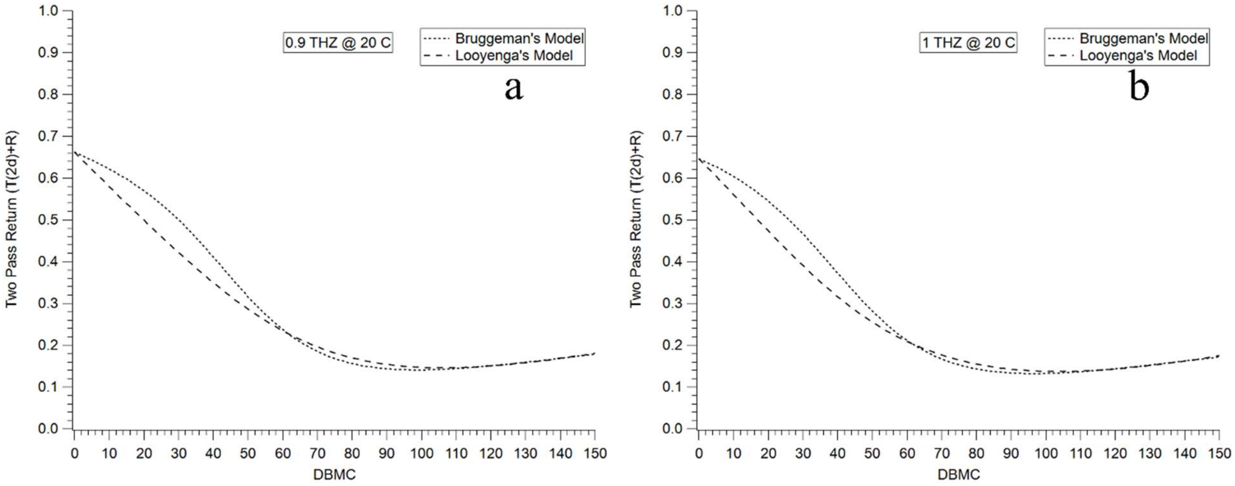

Figure 53. Comparison of 900 GHz and 1 THz at 20 °C.

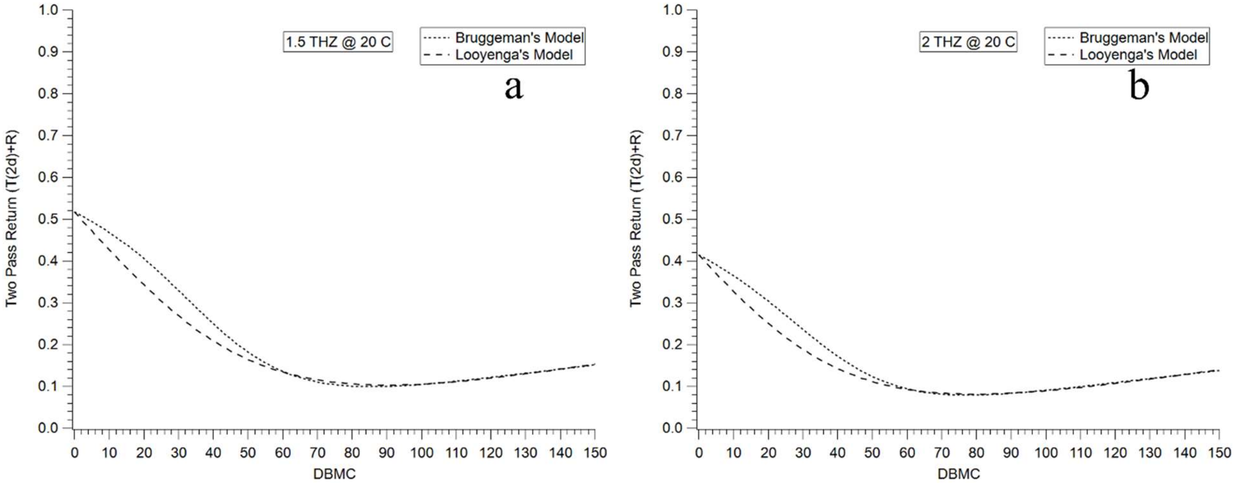

Figure 54. Comparison of 1.5 THz and 2 THz at 20 °C.

An initial qualitative analysis of the models turns up an interesting phenomenon which is the main drawback to operating in two pass transmission mode. As the relative permittivity of the sample increases, as function of moisture content, the transmission drops but the top surface reflection R_1 which is also measured at the sensor increases, as seen in Figure 55. With the proposed sensor, the signal reflected from the top surface of the sample and the signal which has transmitted through the sample and reflected off the backer plate cannot be separated. As such these two signals are functionally combined at the sensor and this results in the received power vs moisture content models having two distinct domains. Domain 1 is where the transmitted signal is dominant and the signal at the sensor is inversely proportional to the moisture content of the sample. Domain 2, which corresponds to high moisture content, is the region where the top surface reflection is the dominant effect measured and the signal at the sensor is proportional to the moisture content. From equations (*77*) and (*78*) domain 1 is expected to have a larger slope than domain 2 since transmission is changes more with permittivity than reflectivity, this change can be seen in the models. The boundary between the two domains is a frequency dependent variable and must be calculated by taking the derivative of a model built for a sample and frequency and looking for its zero.

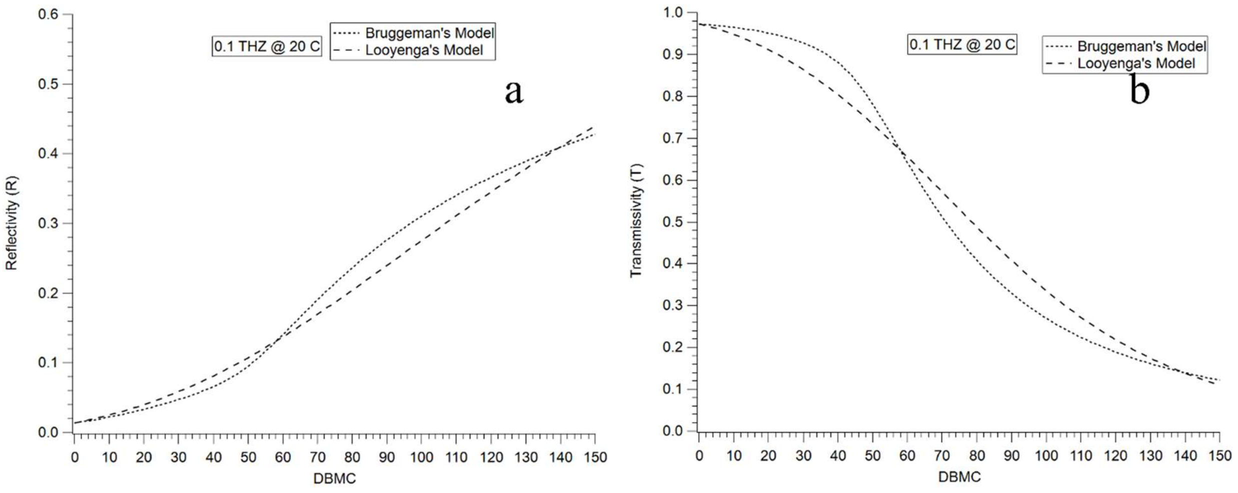

Figure 55. The modeled (a) reflectivity and (b) transmissivity as a function of moisture content for a sample of copy paper.

The existence of the two proportionality domains restricts sensor operation into one of the two domains since if the full range of moisture contents is considered, a signal could correspond to two different moisture contents. For the smart dryer application this limitation is not of great concern as the sensor will be mounted at either the inlet or the outlet so some assumptions can be made about the moisture content range. At the inlet samples will be at or close to their maximum moisture content, which for hand sheet samples is estimated to be around 250 DBMC while at the outlet samples will be close to 0 DBMC. As such, frequency selection will be made based on two aspects of the models; 1. The magnitude of the slope of the model in both domains to maximize the sensitivity at the high and low range. 2. The location of the boundary between the proportionality domains relative to the moisture contents of interest.

For the case of copy paper, 100 GHz was chosen as the optimal sensor frequency. As seen in Figure 56 by taking the derivative of the models built at 100 GHz, the domain boundary is found at around 100 DBMC for both models. This is far enough from the expected input range of 120 DBMC to allow for some moisture content variability in the samples without impacting sensor performance. The sensitivity in domain 1 is very good showing a maximum of -1.5% signal change per percent DBMC. The sensitivity in domain 2 is not as good, with a maximum of 0.2% signal change per percent DBMC, but out of all frequencies modeled this was standard. Operating in the 100 GHz range is also advantageous when it comes to selecting sensor hardware as it falls in the middle of the IEEE designated W-band [135]. The W-band, which spans from 75 GHz to 110 GHz has seen much development in recent years and as such sources and compatible equipment are becoming available at lower prices.

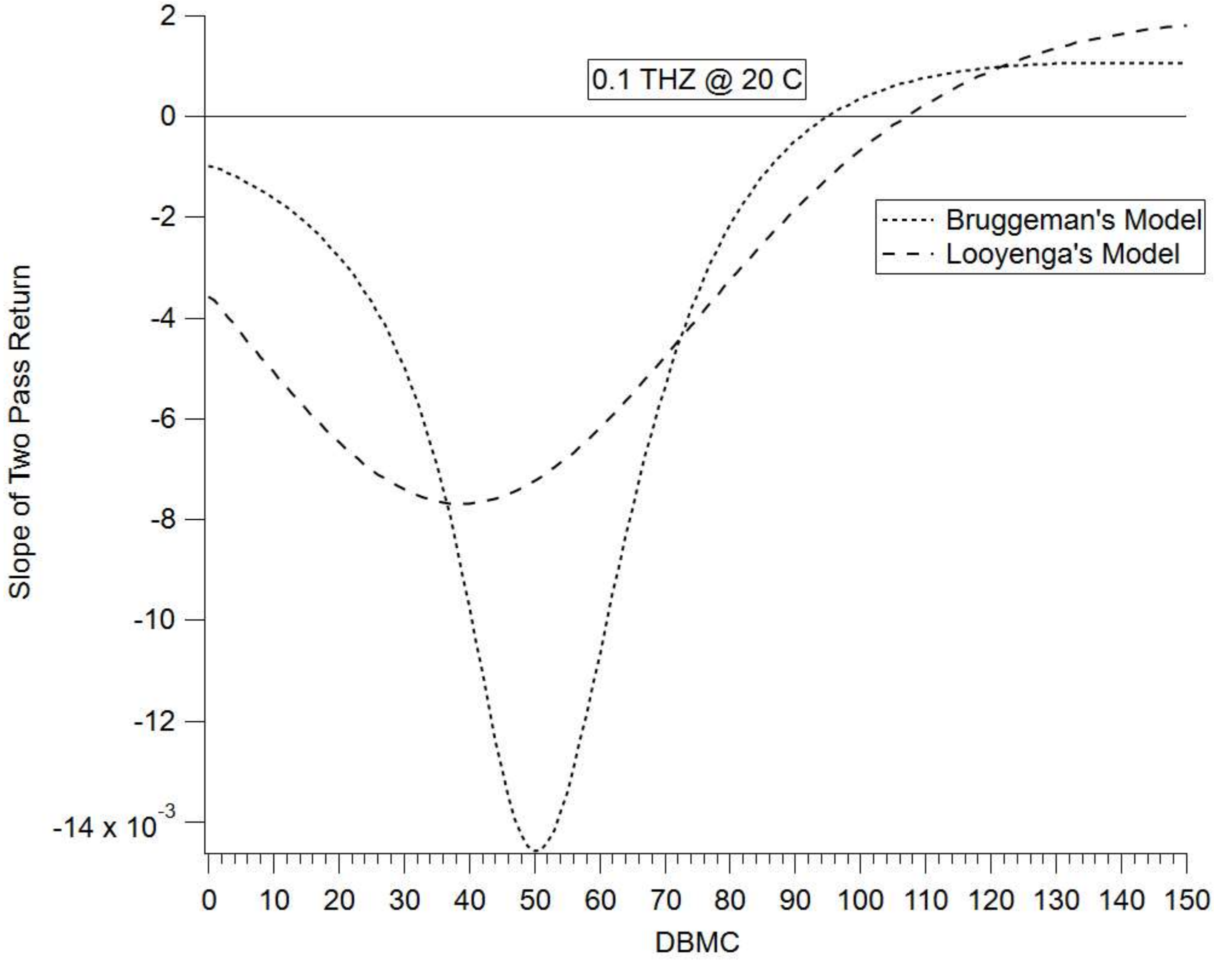

Figure 56. The derivative of the two pass transmission models for the copy paper at 100 GHz and 20 °C.

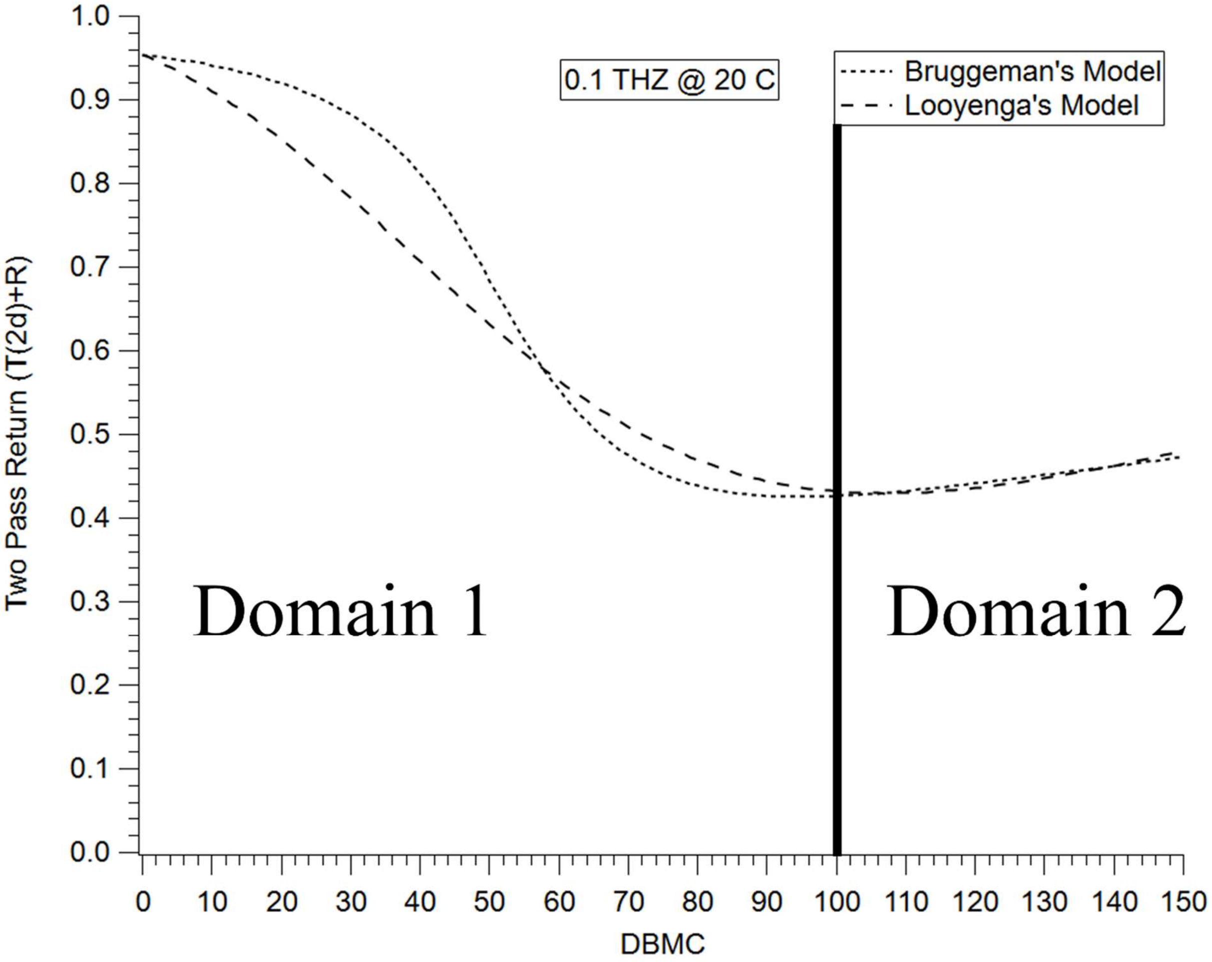

Figure 57. The two pass transmission models for the copy paper at 100 GHz and 20 °C showing the two proportionality domains.

4.2.2.2 Temperature Effect Study

The models in the previous section were all built assuming the sample temperature to be 20 °C. This assumption is fair when considering samples at the inlet of the smart dryer where samples will be around room temperature, but not at the outlet. During a drying run, samples can be exposed to temperatures of up to 230 °C, since the target final moisture content is approximately 5% DBMC the sample itself won't reach these temperatures but can reach up to the boiling point of water at 100 °C. As discussed previously, the sensor models also take in temperature as a variable which allows for temperature dependent studies to be carried out. Models built for copy paper at the frequency of interest 100 GHz and over the range of temperatures achievable by the model.

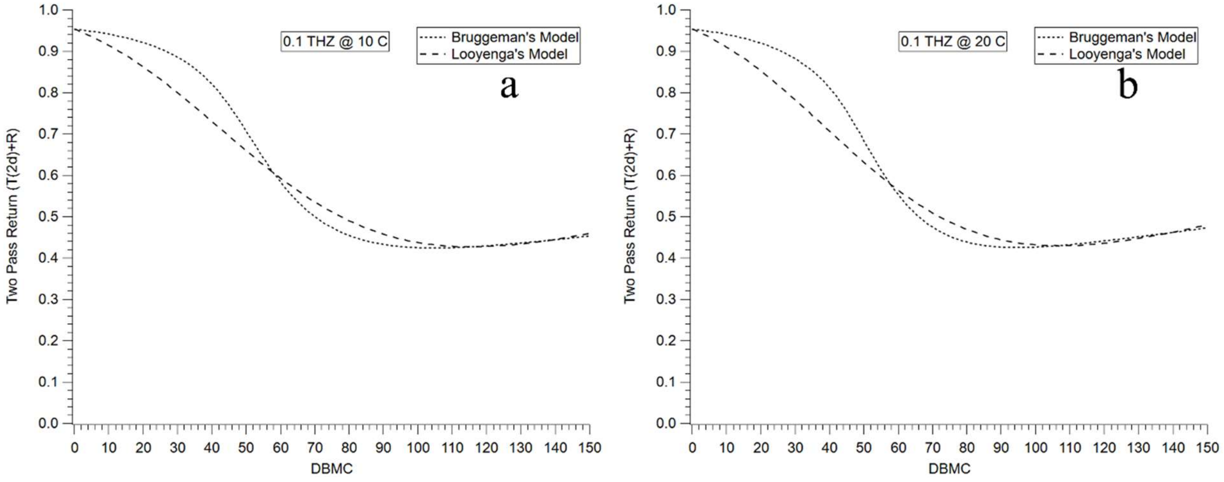

Figure 58. Models for moisture dependent two pass transmission at 100 GHz and (a) 10 °C (b) 20 °C.

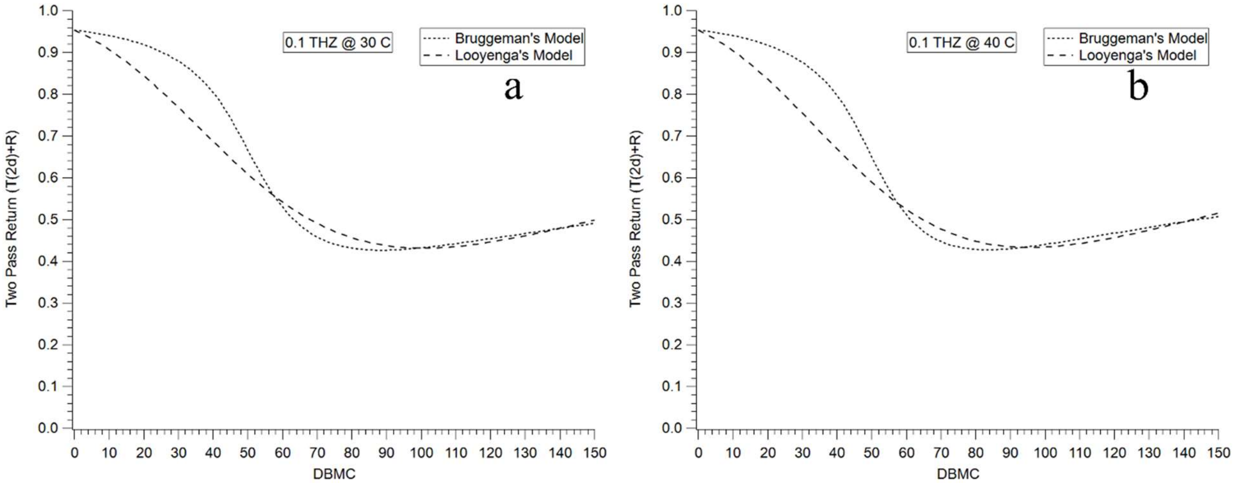

Figure 59. Models for moisture dependent two pass transmission at 100 GHz and (a) 30 °C (b) 40 °C.

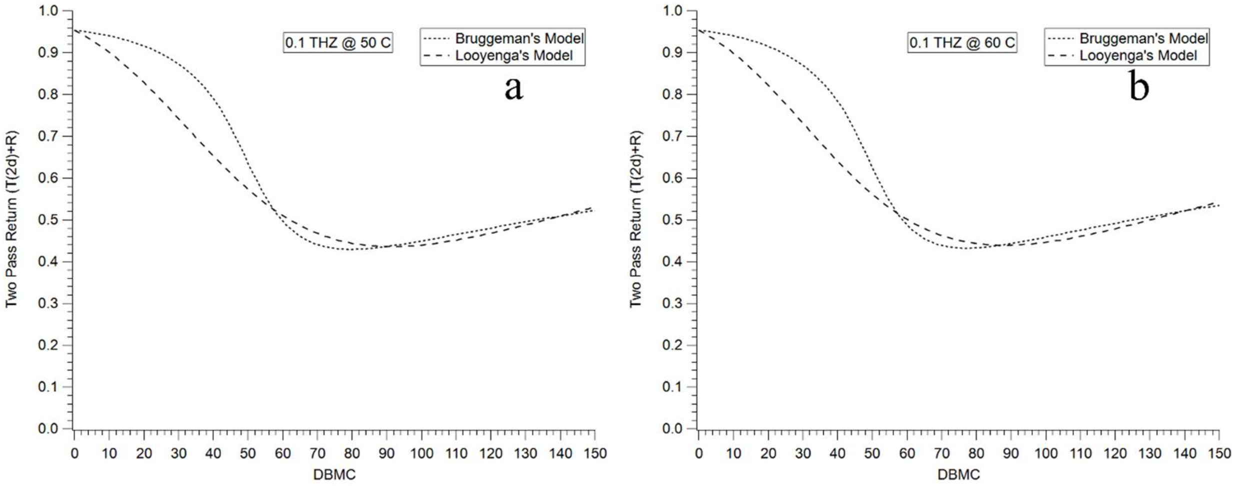

Figure 60. Models for moisture dependent two pass transmission at 100 GHz and (a) 50 °C (b) 60 °C.

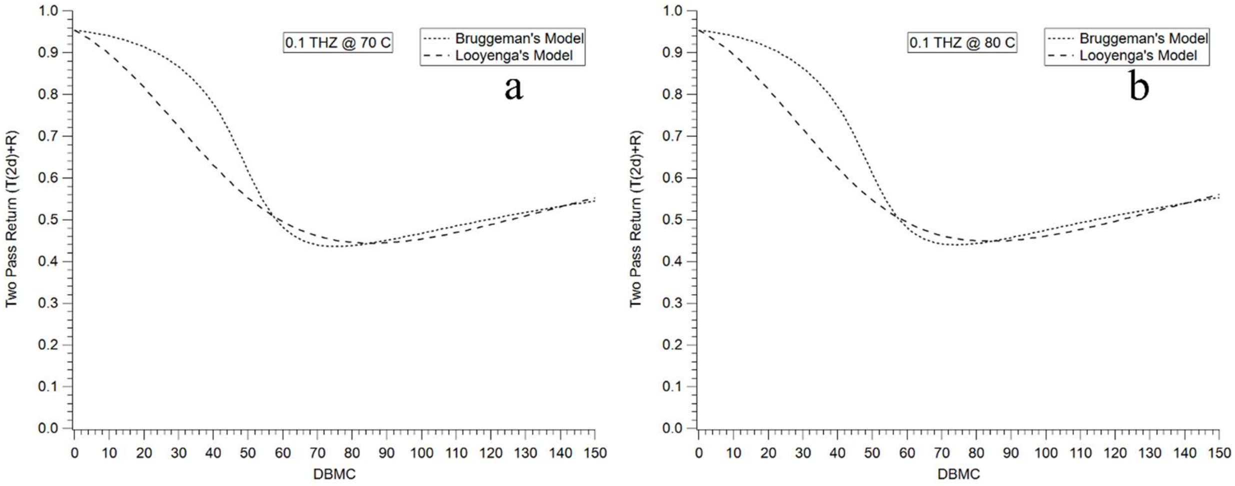

Figure 61. Models for moisture dependent two pass transmission at 100 GHz and (a) 70 °C (b) 80 °C.

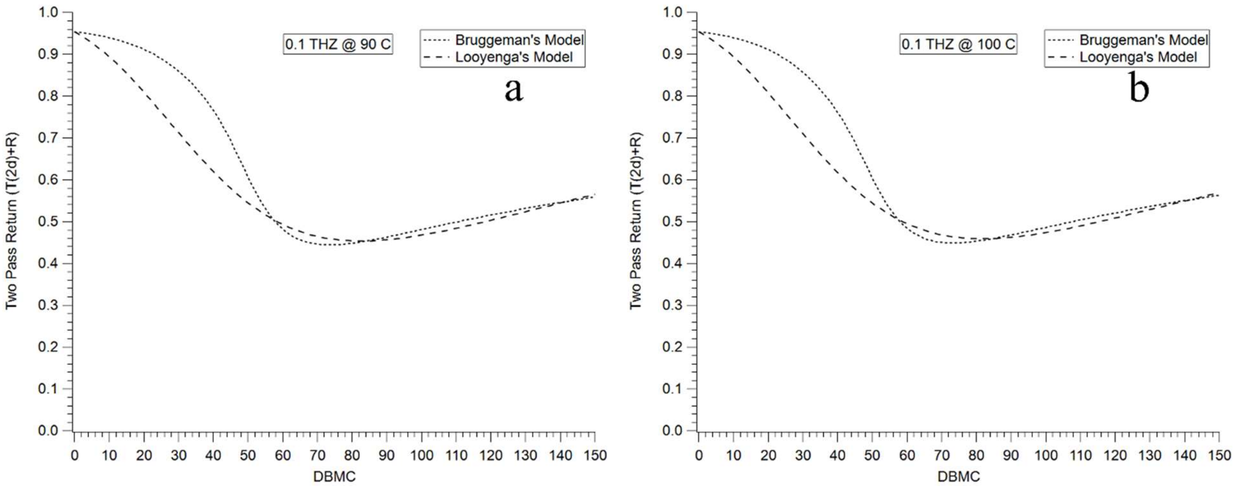

Figure 62. Models for moisture dependent two pass transmission at 100 GHz and (a) 90 °C (b) 100 °C.

From this temperature dependent study, it was found that the boundary moisture content is inversely related to temperature. At 10 °C the boundary occurs at approximately 110 DBMC while at 100 °C the boundary shifts to approximately 70 DBMC. The maximum sensitivity at this frequency occurs at 70 °C where Bruggeman's model has a maximum slope of 1.8 % change in received power per DBMC. At the outlet of the smart dryer, it can be assumed that the sample will be at or very near 100 °C, so the two temperatures of greatest interest are 20 °C and 100 °C. By analyzing the derivatives of the models at 100 °C (Figure 63), it can be seen that Looyenga's model predicts a far greater sensitivity in the low range with an average slope of 0.5% change in received power per DBMC for DBMC<10. For the same moisture range, Bruggeman's model predicts a much lower sensitivity 0.125% change in received power per DBMC for DBMC<10.

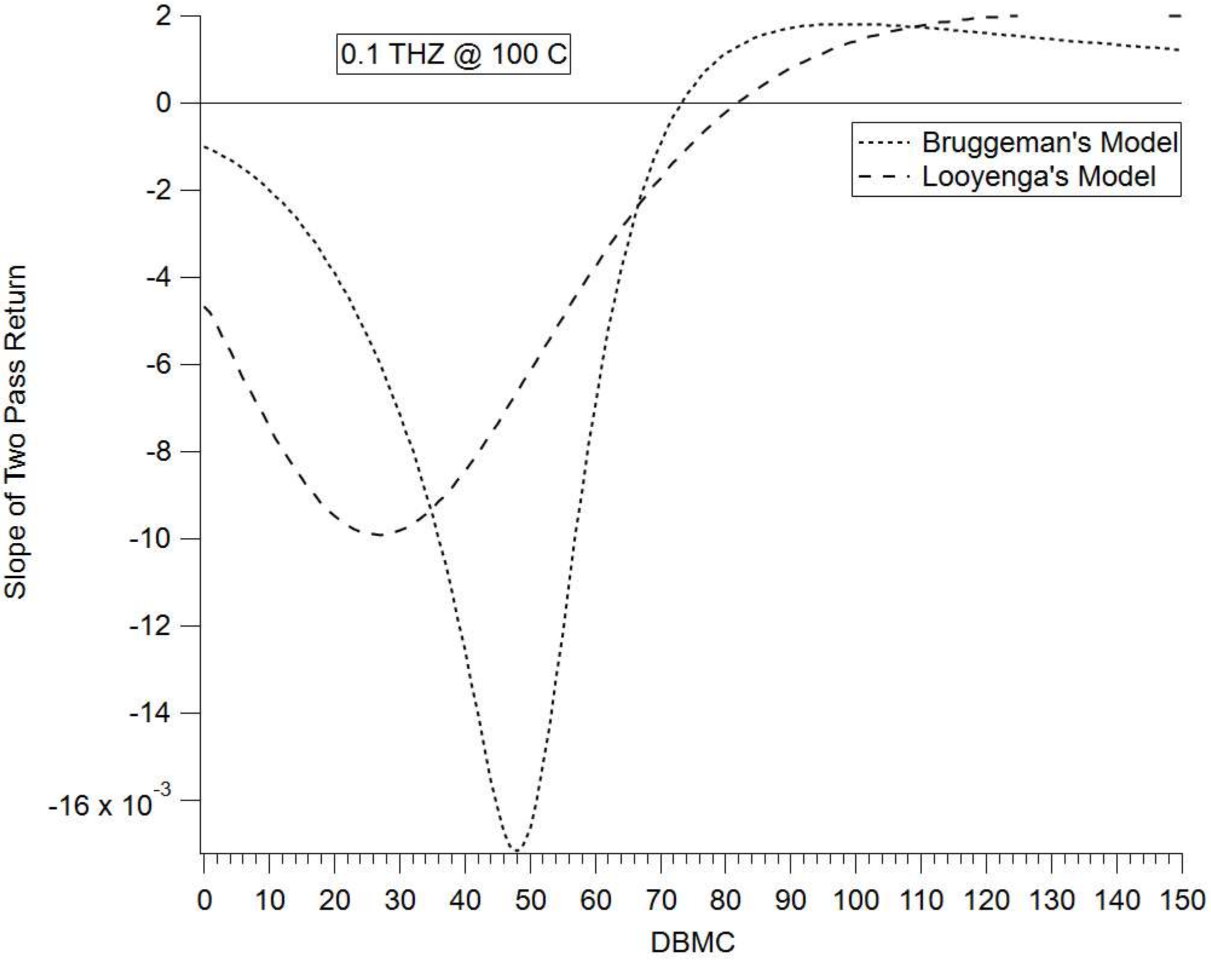

Figure 63. Modeled sensitivity of a 100 GHz moisture sensor at 100°C operating in two pass transmission mode.

With the development and analysis of these comprehensive sensor models, laboratory tests must be carried out to assess the accuracy of these models. Additionally, equipment must be selected for the development of the smart dryer moisture sensor and the sensor must be integrated into the dryer. This work is described below.

4.3 ANALYSIS AND RESULTS

This section covers experimental applications of the effective medium theory-based sensor models. Initial experiments are conducted on copy paper in transmission mode using THz TDS, then a sensor platform is chosen and developed, and the results are presented and analyzed.

4.3.1 THz TDS Experiments

To initially validate the sensor models, THz TDS was used as it can provide stable transmission data over a wide bandwidth, eliminating the need for many experiments with many different sources. The THz TDS system used was a Toptica Teraflash Pro with an imaging extension. Samples were measured in transmission mode due to the Teraflash imaging gantry's reflection mode having too wide of a reflection angle for the models to be valid. Samples were secured to a custom sample holder, seen in figure, which held them at the focus of the TDS system while also resting 4 legs on the weighing pan of a Sartorius Entris II balance.

In these experiments, copy paper was cut into circular samples 4.5 cm in diameter. The samples were baked at 100 °C and under vacuum to remove any moisture due to ambient humidity. After baking the samples were weighed to get their "bone dry" mass (BDM) and the samples were measured in transmission by TDS to measure the relative permittivity of the "bone dry" paper. The samples were then immersed in a bath of water and given 2 minutes to fully saturate. After 2 minutes samples were removed from the water, patted dry with a paper towel to remove excess surface moisture, and then placed onto the sample holder. The sample holder was placed onto the weighing pan of the balance, a plastic ring was placed over the samples to prevent curling of their edges during drying. Over the next 90 minutes, TDS measurements were made in tandem with mass measurements every 15 seconds.

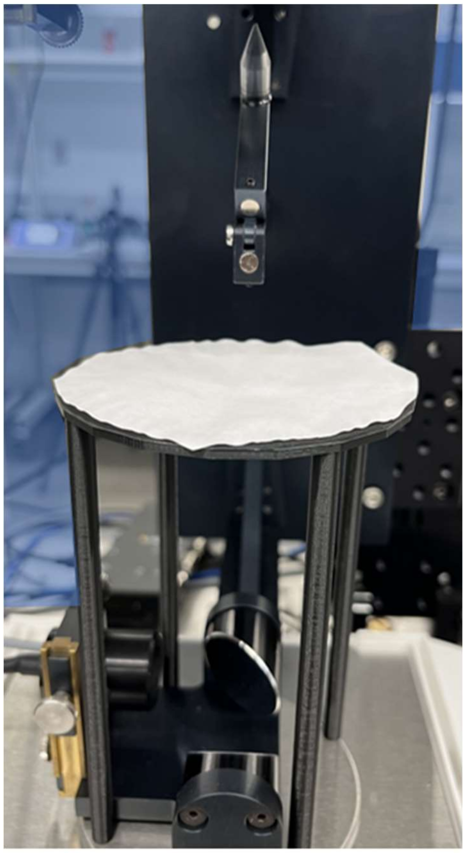

Figure 64. A sample of copy paper on black custom sample holder. The sample holder is standing on the weighing pan of a Sartorius Entris II balance.

Each experiment produced 360 TDS measurements which corresponded to sample DBMC. Processing the TDS pulses using nelly [134], gives moisture dependent relative permittivity data which can be used to calculate transmission as a function of DBMC. This can be directly compared with the sensor models to assess accuracy. A drawback of using the TDS system for this experiment is that the bandwidth of the Teraflash only practically goes down to 300 GHz. Although these experiments can’t capture the planned sensor development frequency, the results are still useful to give an idea of the accuracy of the model at 100 GHz.

A significant source of error in these experiments came from the sensitivity of the balance. To make the transmission measurements possible, the draft shield of the balance was removed which made it sensitive to any air currents in the lab. This was mitigated by putting an enclosure over the entire experiment. The enclosure eliminated the air current sensitivity, but the balance was still sensitive to any vibrations which would cause the mass reading to vary. Seen in Figure 65, the transmission data was quite smooth. When graphing it against DBMC as measured with the balance in Figure 66, the data becomes quite noisy.

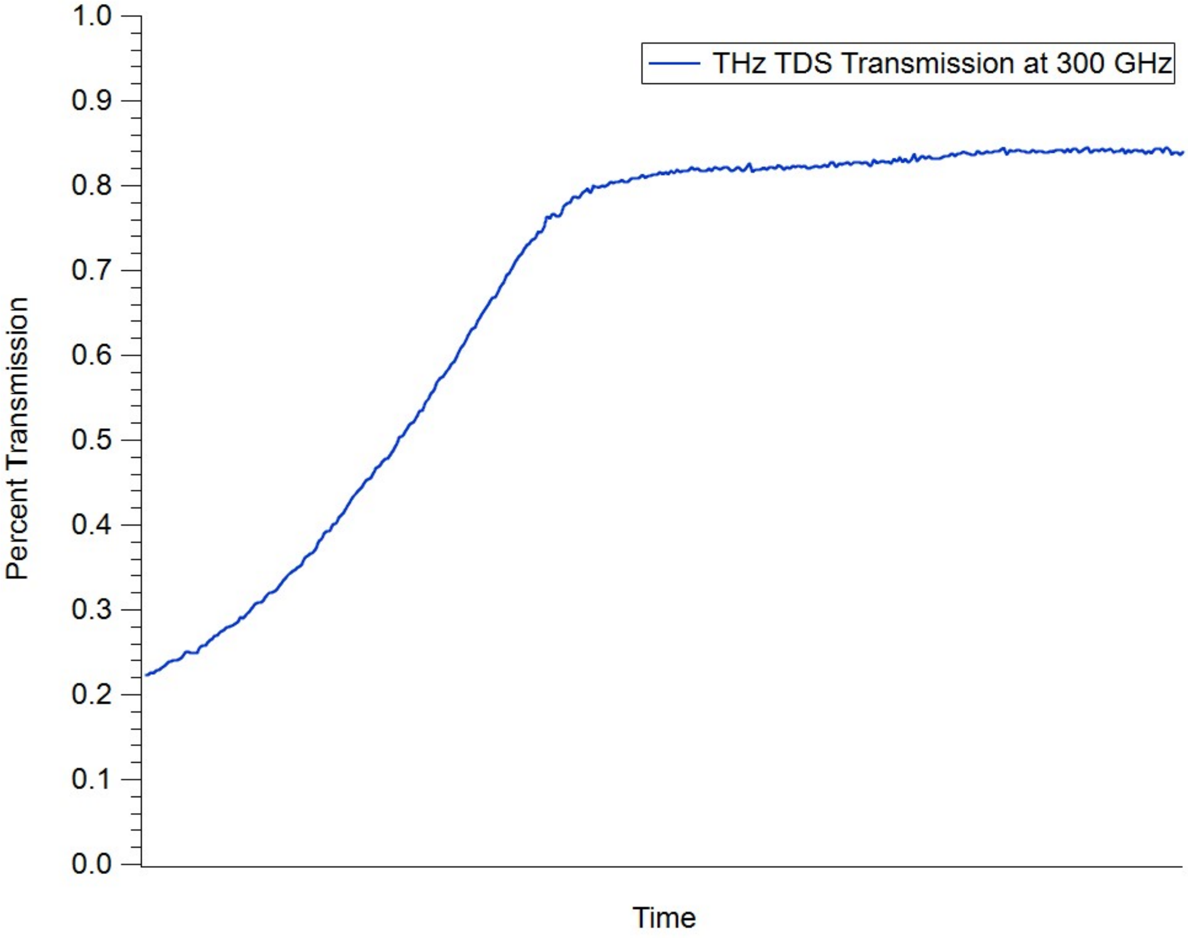

Figure 65. THz TDS transmission measurement taken of a drying sample of copy paper. Transmission was measured at 300 GHz. The time axis in this graph spans approximately 90 minutes.

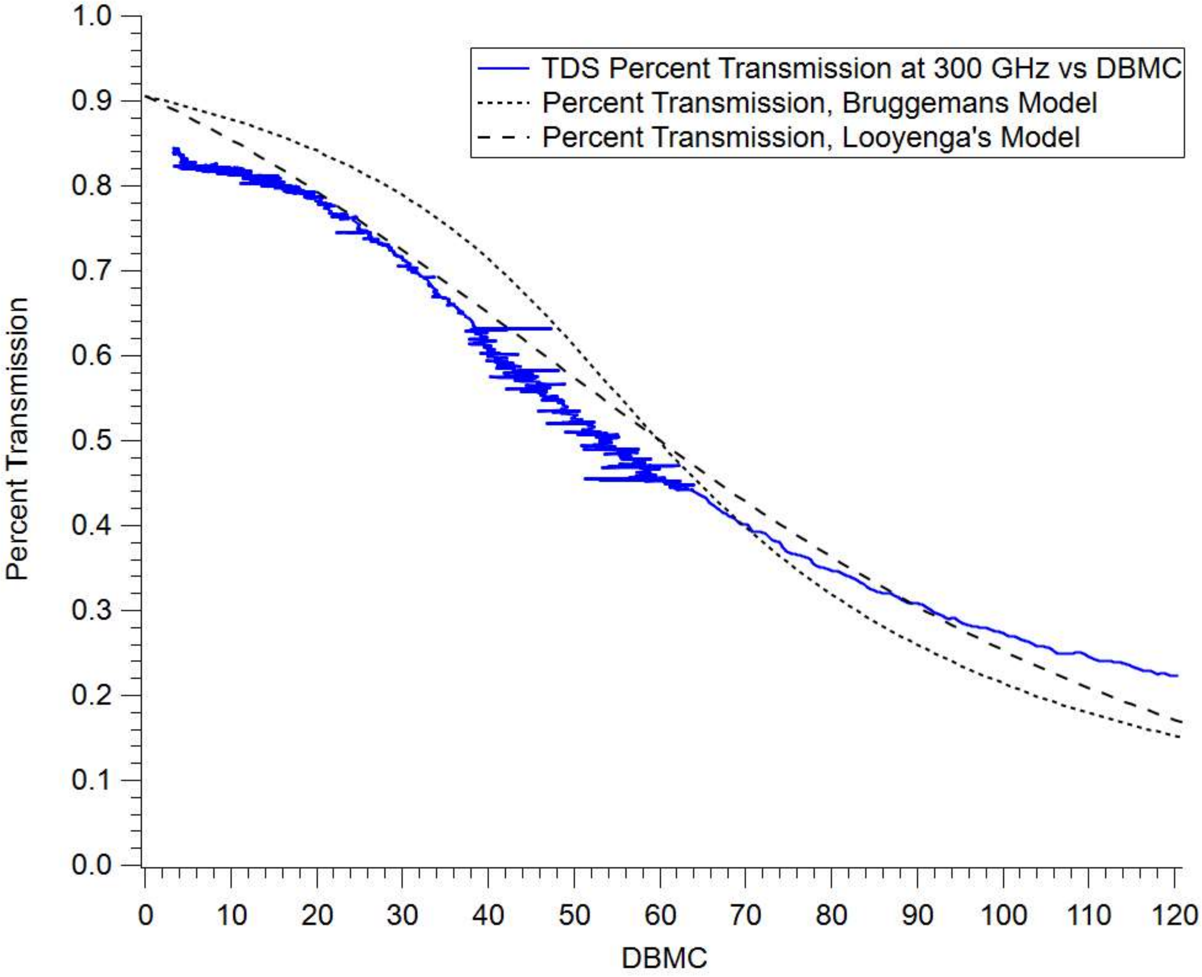

Figure 66. THz TDS transmission measurement taken of a drying sample of copy paper vs dry basis moisture content measured gravimetrically (blue) compared to transmission models using Bruggeman's (small dashes) and Looyenga's (large dashes) models. This experiment was conducted at ambient laboratory conditions, with a temperature of 20 °C and humidity of 30%.

To compensate for noise introduced from the gravimetric DBMC measurements and to create a waveform that would allow for further analysis, Igor Pro's Interpolate2 function was used. Interpolate2 takes in x and y data and performs linear interpolation to create a dataset from an x and y dataset. This interpolation retains the overall behavior of the above graph but by under sampling the DBMC data, can allow for smoothing out of variations. Any non-physical variations still present in the linear interpolation can be smoothed out using the Savitzky-Golay smoothing procedure [136] without affecting the overall shape of the curve. A comparison of the raw data, linear interpolation, and smoothed linear interpolation can be seen in Figure 67.

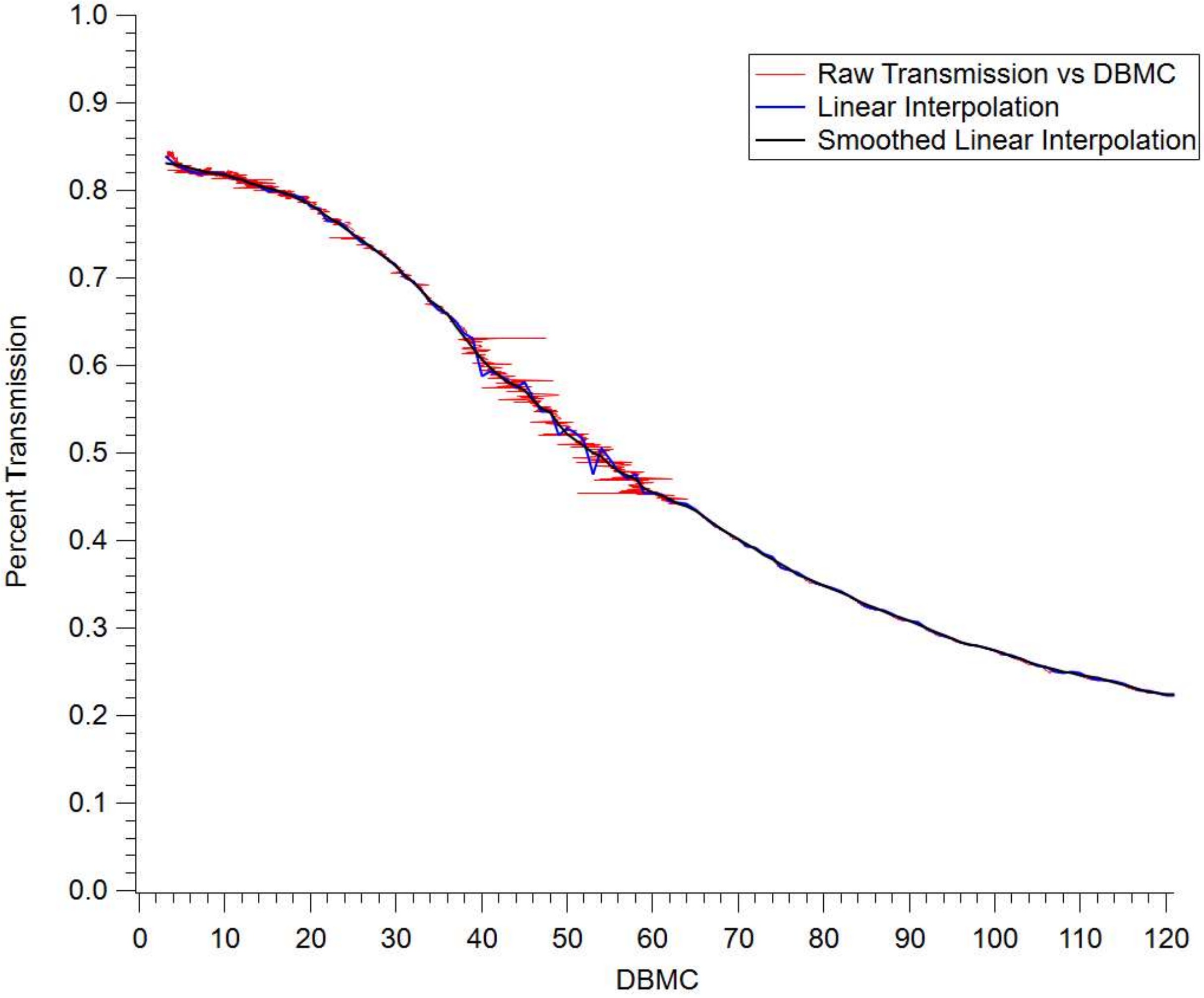

Figure 67. A comparison of raw transmission vs DBMC data (red), the under sampled linear interpolation of the data (blue) and the smoothed linear interpolation (black). It can be clearly seen that linear interpolation works well to describe the raw data while eliminating variations from the gravimetric DBMC measurement.

With the linear interpolation working as a representative of the raw data, the error of the models in estimating the transmission through the sample can be evaluated. Figure 68 shows the smoothed linear interpolation of the raw data and the models graphed together showing an overall good agreement between the models and the data. The efficacy of the models must be tested by finding their percentage error in estimating transmission and their error in estimating moisture content. The fractional error of the modeled transmission vs DBMC (model_T) and measured fractional transmission vs DBMC (raw_T), as described in equation (85) and shown in Figure 69.

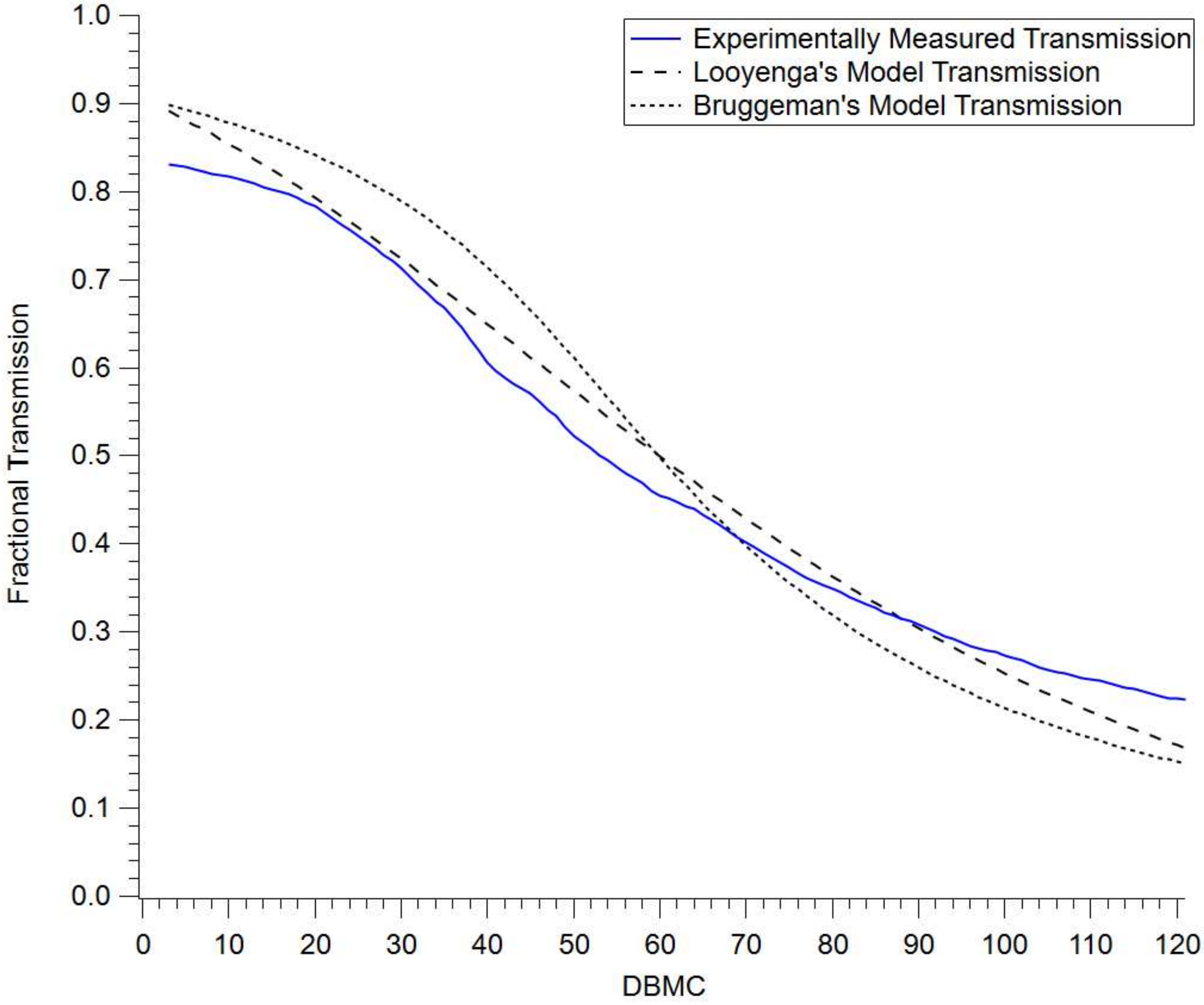

Figure 68. The linear interpolation of the raw TDS fractional transmission data at 300 GHz (blue) graphed along with the two effective medium models showing the good agreement the models have with the data.

$$\%\mathrm{error} = \frac{|\mathrm{model}_T - \mathrm{raw}_T|}{\mathrm{raw}_T} \tag{85}$$

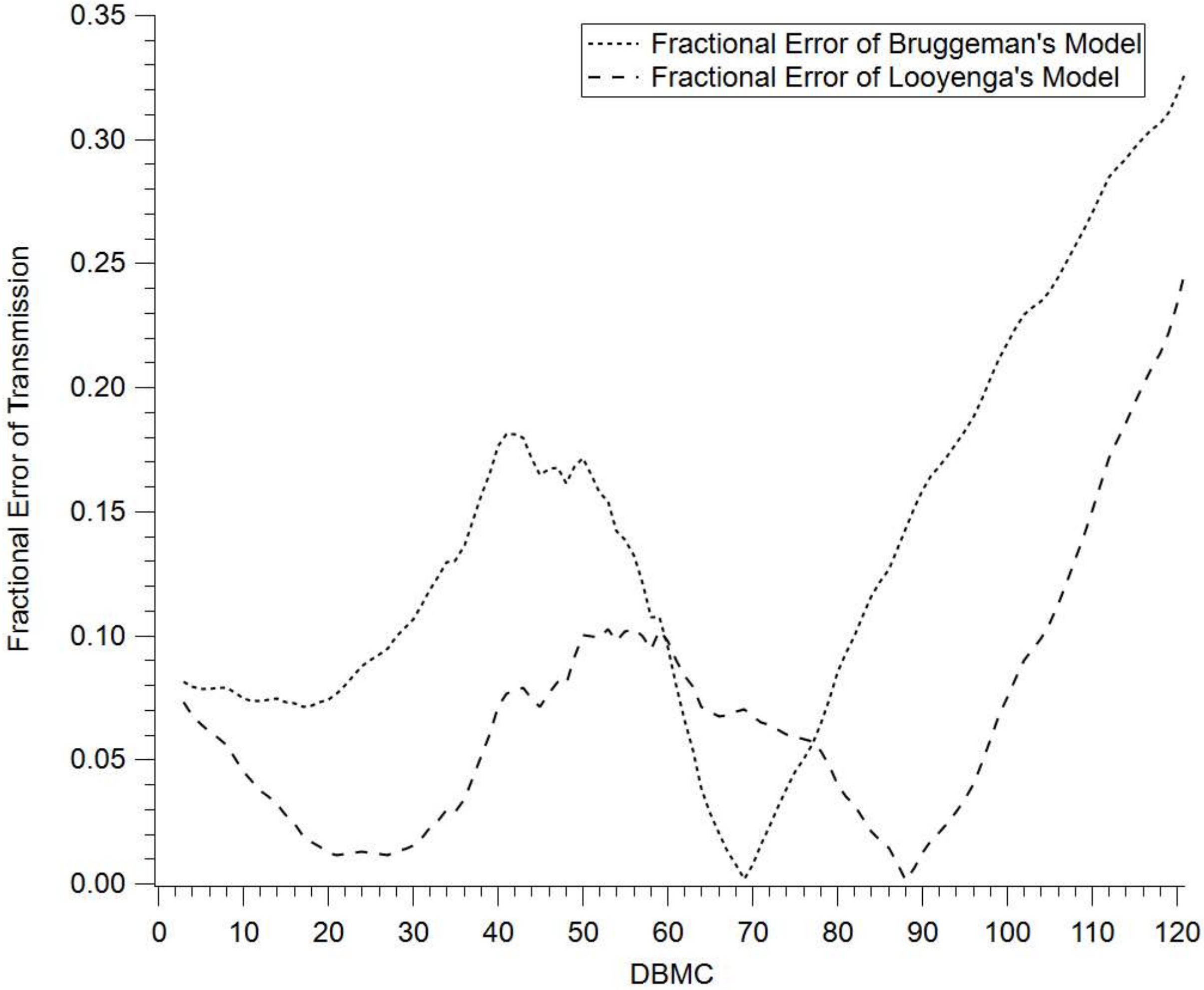

Figure 69. The fractional error of the models at predicting the percent transmission through a sample versus the moisture content of the sample.

The percentage error of the models at predicting transmission through a sample as a function of moisture content is very promising with Looyenga's model having an average percentage error of 6% and Bruggeman's model having an average percentage error of 13%. The large percentage error in the high moisture content range comes from (85) where the percentage error is inversely proportional to the percent transmission which shrinks as moisture content increases. Here it is more interesting and informative to look at the absolute difference between the model's predicted transmission as a function of moisture content versus the experimental data. This can be seen in Figure 70.

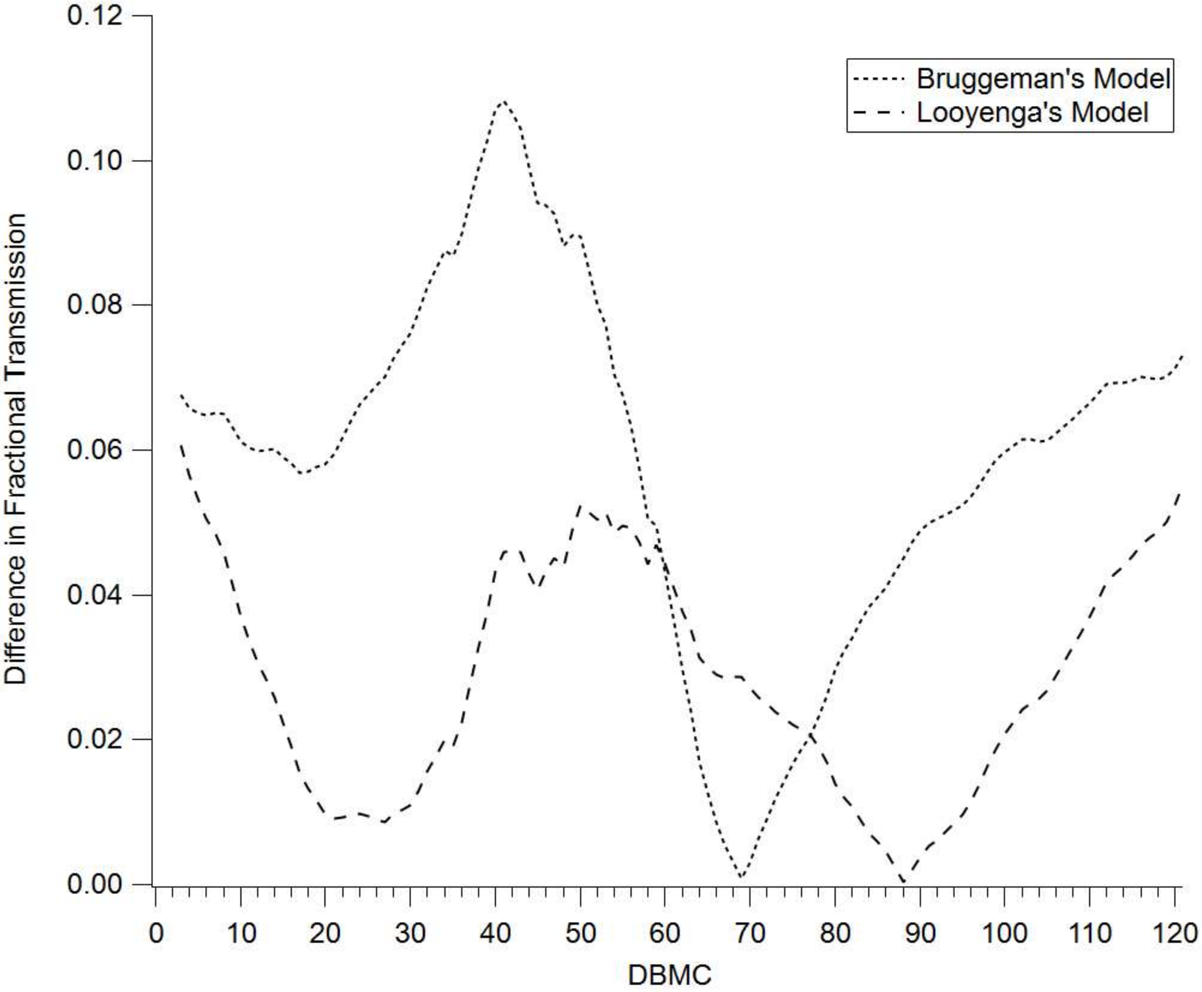

Figure 70. The absolute difference between the predicted fractional transmission through a sample as a function of moisture content from Bruggeman's and Looyenga's models and the experimental data at 300 GHz.

Here we can see that the error in the models does begin to grow in the high moisture range but not as dramatically as in Figure 69. The average difference between the predicted transmission from Looyenga's model and the experimental data was 2.8% while Bruggeman's model was off by 5.8%. We can see that the performance of the models assessed using the absolute difference and percentage error have the same approximate difference with Bruggeman's model have about double the error as Looyenga's model.

The final and most important bit of the analysis of the models is quantifying their effectiveness at predicting moisture content. The previous analyses have looked at their error in predicting percent transmission when moisture content is known but the actual sensor will need to estimate moisture content from measured signal strength. To do this analysis, Igor Pro's Interpolate2 function was used again to swap the X and Y axes of the models and measured data, giving moisture content vs percent transmission waveforms, these can be seen in Figure 71. These waveforms will ultimately be what the sensor uses to estimate moisture content so the quantification of the error of the models in this form is crucial.

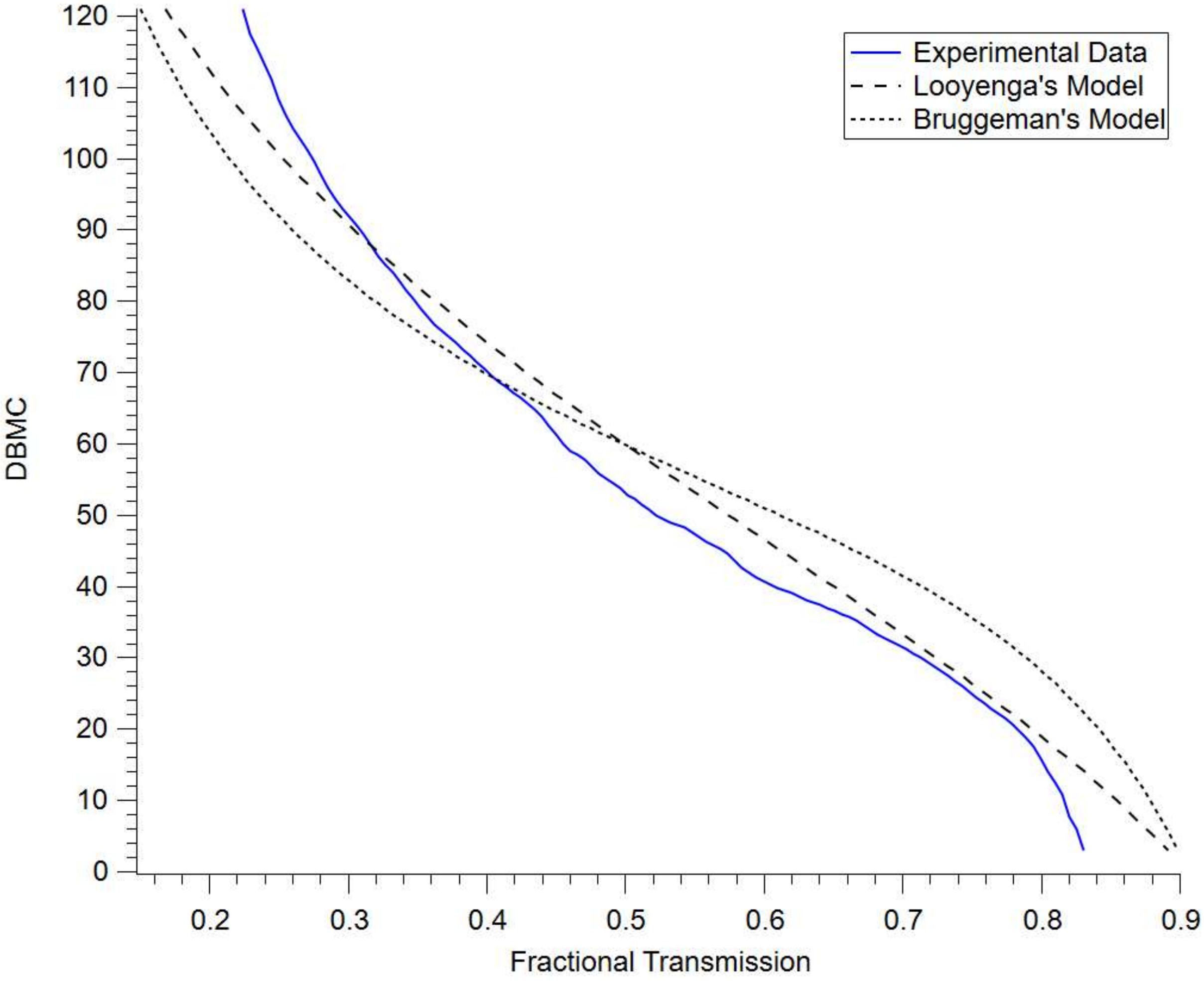

Figure 71. The experimental data (blue) and models (black dashed) reinterpolated to be in terms of DBMC vs fractional transmission.

Here the error in moisture content prediction can be found as the difference between the models and the experimental data. This error can be seen in Figure 72.

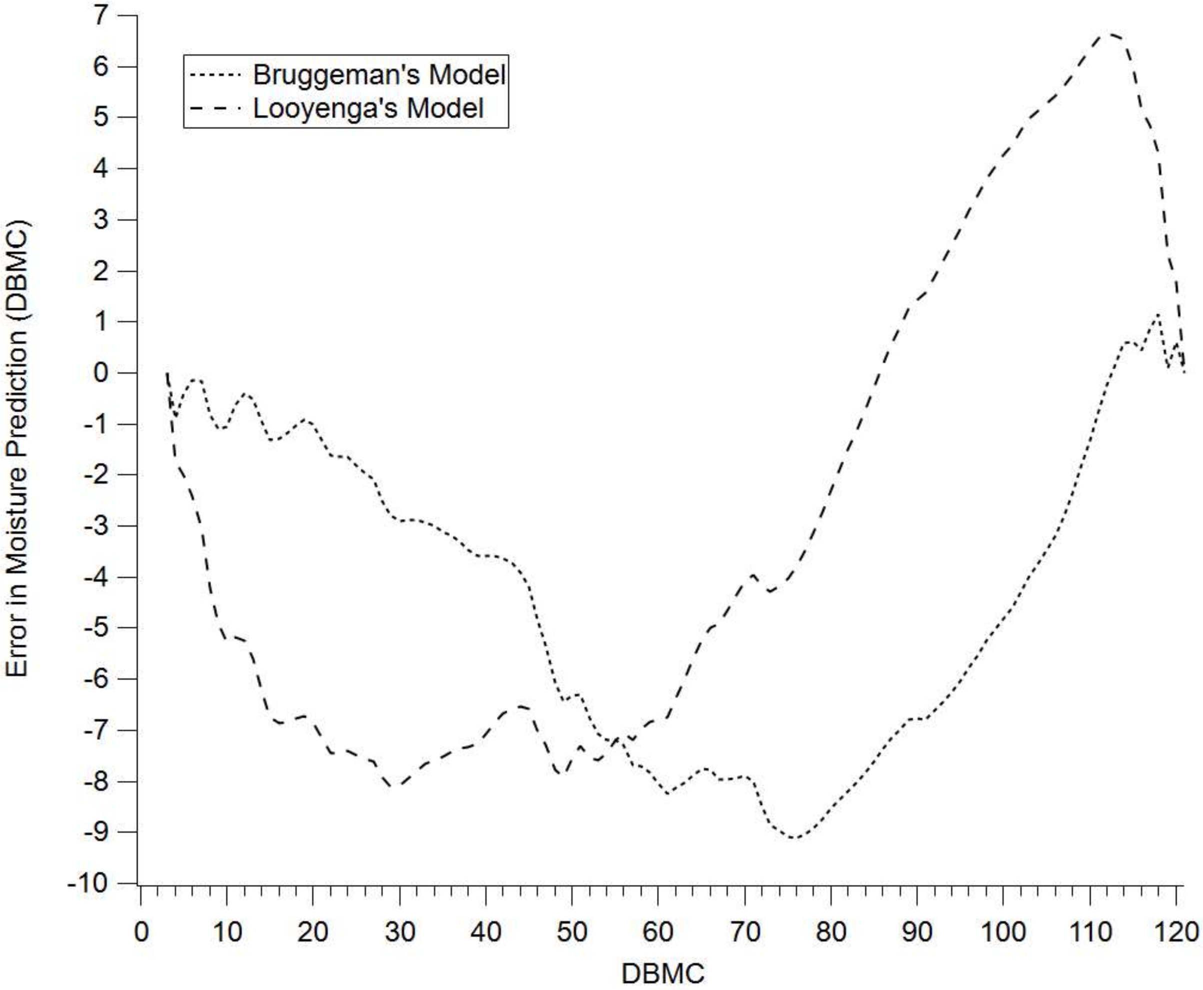

Figure 72. The error of the models in predicting moisture content of a sample as a function of the moisture content.

To find the average error in the moisture content prediction, the average of the absolute difference (Figure 73) is taken. The average moisture content error from Looyenga's model is 5.1% and the average moisture content error from Bruggeman's model is 4.4%.

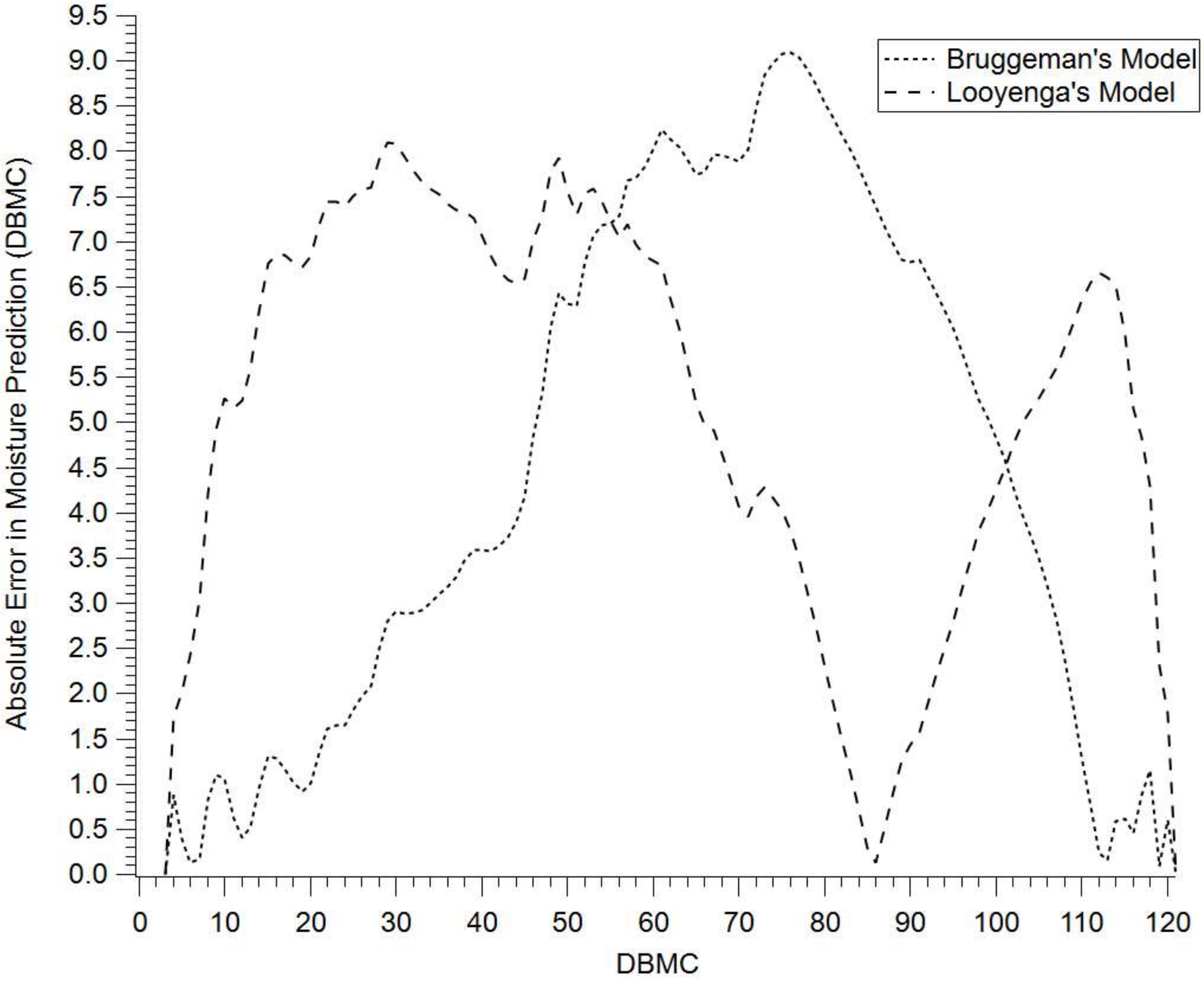

Figure 73. The absolute error in the moisture content predictions from the two models, showing that Bruggeman’s model has a lower average error.

From this analysis, it can be seen that Bruggeman’s method does a better job predicting moisture content even though it does a worse job predicting percent transmission. This may seem rather puzzling, but this effect was expected. The effective medium models are built assuming that the moist paper hybrid material is made up of only two materials, liquid water and bone-dry paper. While this assumption may seem sound, the water in this hybrid material actually exists in two forms as described in Figure 45, free water which is equivalent to normal liquid water, and associated water. The associated water is hydrogen bonded to the host material (bone dry paper in this case) which causes its relative permittivity to change. This effect is not well studied, with only a few observations of it described in literature [137-139]. Due to the hydrogen bonding reducing the dipole moment of the water molecules in the associated water, its relative permittivity is lowered. This causes the two-parameter effective medium models to underpredict the transmission through a wet sample in the high moisture content range. This is because the models assume the volume of water in the sample to be purely free water, the presence of the associated water lowers the effective permittivity of the water in the sample.

From literature, the magnitude by which the permittivity of the associated water is lowered is entirely sample dependent, making it difficult to model. The associated water in the models could be accounted for by adding a third material, representing the associated water, and sweeping possible values of permittivity until a permittivity value is found that results in models that best fit experimental data. This expansion of the models is outside of the scope of this work, however.

With the effect of the associated water in mind, the slopes of the models predicting moisture content versus percent transmission will give the best insight as to which effective medium theory best describes the system.

4.3.2 Sensor Selection and Design

4.3.2.1 Sensor Platform

After a thorough review of commercially available sources and detectors in the W-band that could be used for the moisture sensor, the Texas Instruments IWR1642BOOST mmWave evaluation board coupled with a Texas Instruments DCA1000EVM real-time data-capture module, was selected. The IWR1642 and DCA1000EVM represent a significant cost reduction over other commercially available systems, with a combined price of $900 compared to other systems at $10,000 and above. This cost reduction was important not only to stay within the budget of the larger smart dryer project, but to aim for a price point which could be attractive to industrial customers. The IWR1642BOOST board will allow for easy integration as it features both transmit and receive antennae laid out coplanar, seen in Figure 74.

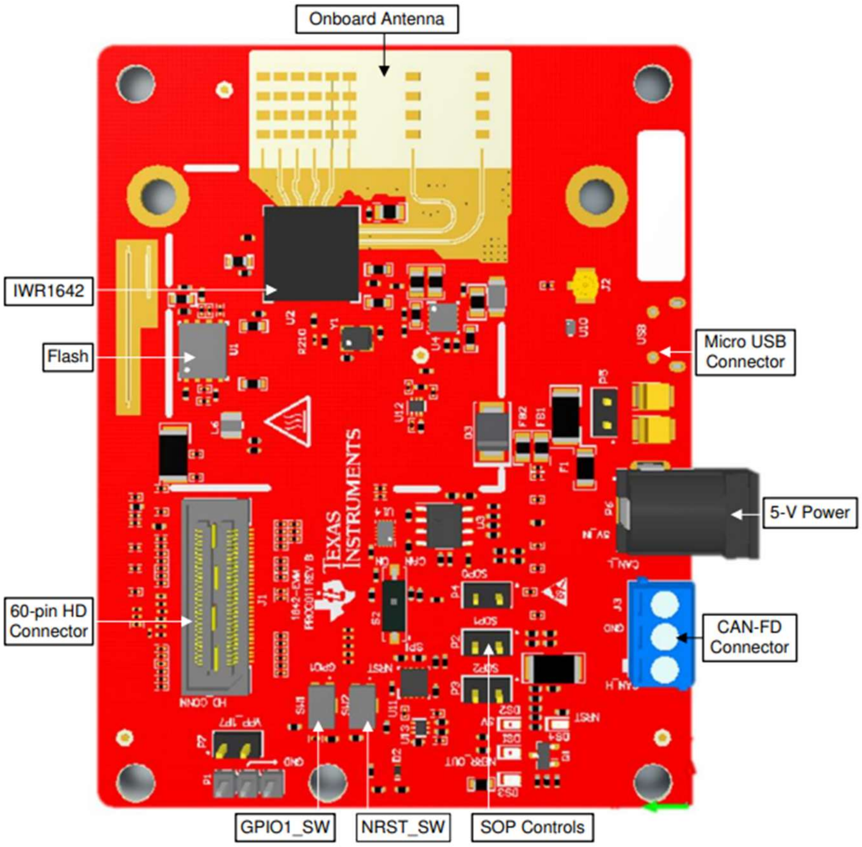

Figure 74. A rendered image of the TI IWR1642 BOOST evaluation board showing various IO ports as well as the coplanar transmit and receive antennae. Image sourced from [140].

The board is sold as an evaluation platform for the IWR1642 automotive radar module operating in the 77 GHz to 81 GHz bandwidth as a frequency-modulated continuous-wave (FMCW) radar. A simple block diagram of the RF circuitry of the IWR1642 can be seen in Figure 75. When combined with the DCA1000EVM, the system can be configured using TI’s mmWave Studio and then controlled through MATLAB scripts. The intended application of this module is to detect objects within a wide field of view and measure their range and relative velocity, with some modifications however, it may be useful as a moisture sensing platform.

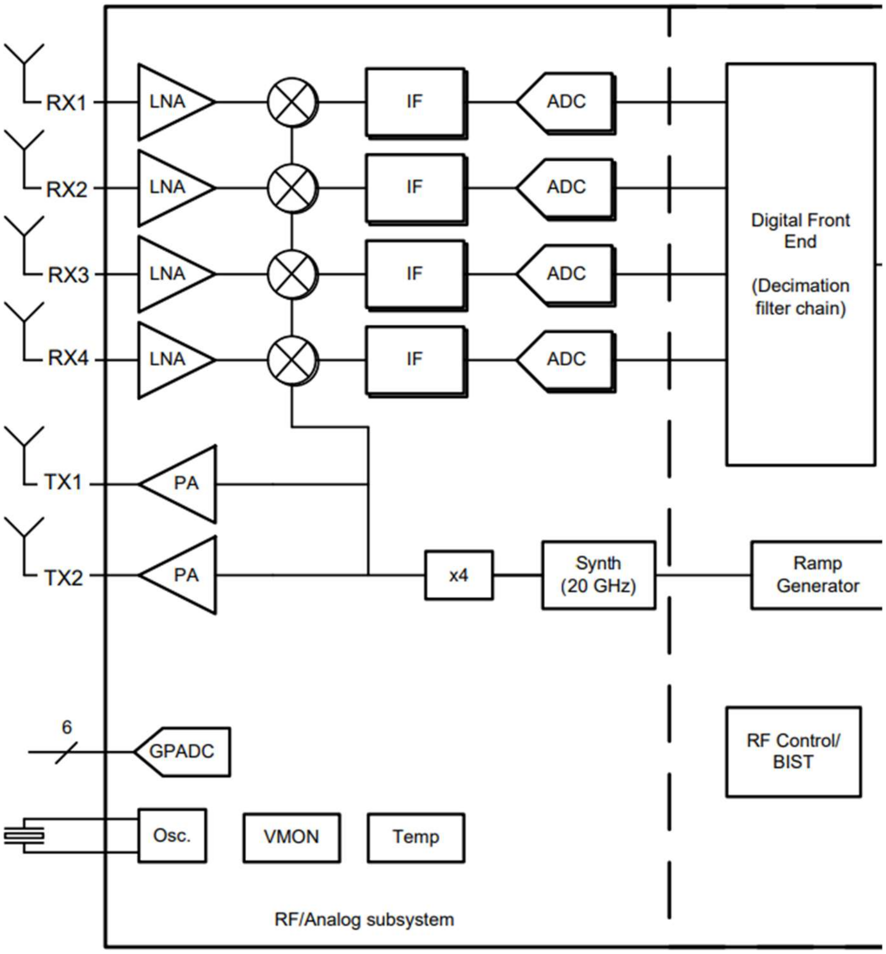

Figure 75. A simple block diagram of the RF circuitry of the IWR1642. Sourced from [141].

As an FMCW radar, the IW1642 sweeps or “chirps” its output frequency using the ramp generator on the block diagram. This swept signal is then split between the transmit antennae and LO ports of IF mixers in the receiver paths. These IF mixers take in the received signal from the receiver antennae at their RF ports and mix it with the LO signal. The mixers then output the frequency difference between the transmitted and received signal on their IF ports which is then digitized by analogue to digital converters (ADC) for further processing, the FMCW radar method is described in greater detail in section **2.3.1.2**. The resulting output data from the radar is a raw time varying signal from the analog to digital converter and a power versus range profile resulting from a fast Fourier transforming the ADC data. In typical operation, this range profile would be used to detect objects at ranges of up to 84 meters with a range resolution of up to 36.6 centimeters.

To be used as a moisture sensor, ideally the frequency of the radar would be held constant, but this would result in the IF mixers outputting a DC signal on their IF ports and the presence of DC blocking filters before the ADCs would filter this out. As the radar was never intended to operate in this fashion these DC blocking filters cannot be disabled. The smallest possible bandwidth to operate the radar at was found to be 1.5351 GHz. From analysis of the variance of the moisture models from 77 GHz to 78.5351 GHz, this sweep range was not anticipated to cause significant issue. This chirp bandwidth was set as the default for the radar with a sweep rate of 29.982 MHz/µs and period of 51.2 µs. The range resolution of the radar, or the range over which single objects can be detected, while using this sweep configuration was 97.7 cm which proved to coarse to provide a defined peak caused by the presence of a sample. The range variance observed when trying to monitor single peaks to correspond to the sample was far too high to make this method viable. Instead, it was found that by measuring the change in average power over the expected measurement range of the sensor, which was set by default at 25 meters, could provide accurate measurements of the returned signal strength and attenuation caused by the samples.

The feature of the IWR1642BOOST anticipated to cause the most issues is the antennae. Since the board is designed to operate as a radar and detect objects within a large area, the patch antennae on the board were designed to have wide gain patterns. These gain patterns, shown in Figure 76, tell how the radiation is spread out from the emitter and what angles the receiver will detect radiation from. To quantify directional gain of an antenna, the point at which the gain pattern drops below 3 dB is often quoted, known as the 3 dB beamwidth. For the antennae on the IWR1642BOOST board, they have a 3 dB beamwidth of 90° in the horizontal plane and 40° in the elevation plane. This wide 3 dB beamwidth is anticipated to cause the effect of the sample on the detected wave to be lessened as the radar will be illuminating an area wider than the sample and all previous models have assumed that the sample will be larger than the beam. This effect can be mitigated by positioning the radar close enough to the sample to allow most of the emitted power to interact with it.

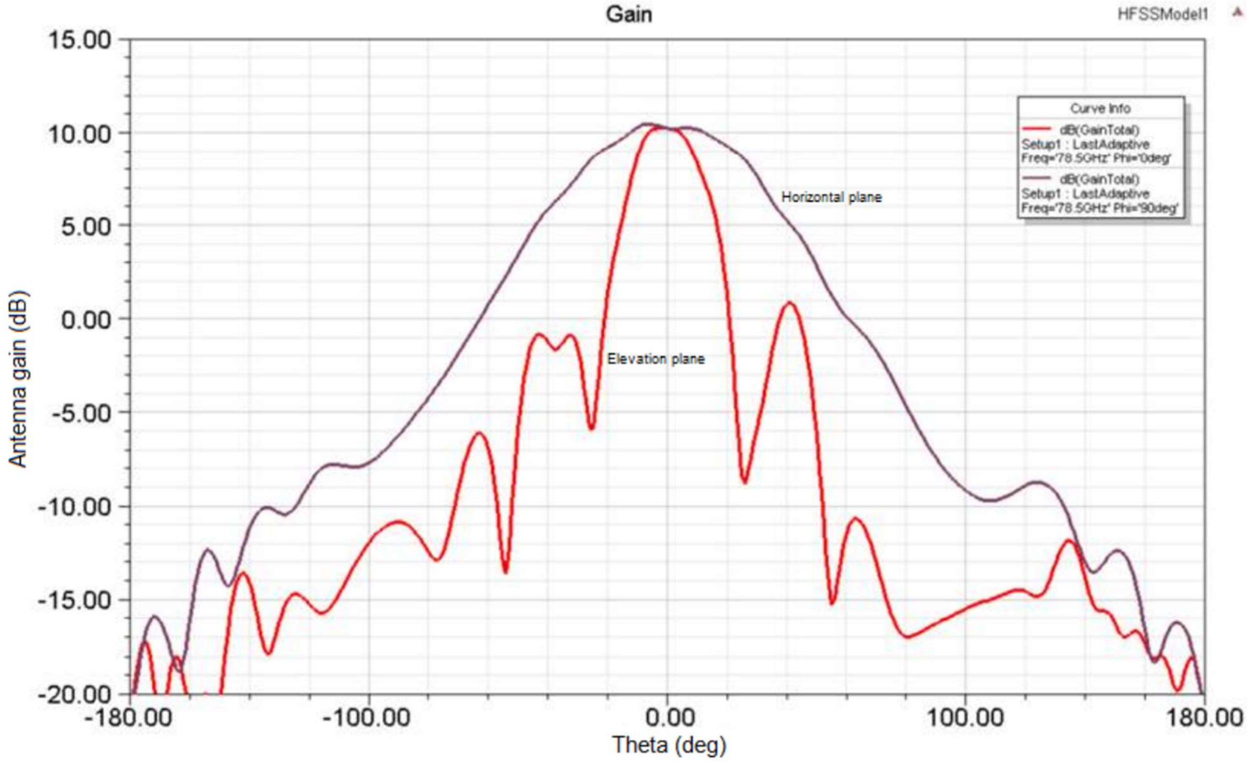

Figure 76. The gain patterns of the antennae on the IWR1642BOOST board, with the gain in the horizontal plane in purple and the gain in the elevation plane in red. Sourced from [140].

4.3.2.2 Sensor Models

All previous models have been built assuming a constant frequency which is not possible with the IWR1642. Due to limitations of the control software of the IWR1642, it is not possible to know what frequency is being measured at any one time and with the signal strength analysis being done on an FFT, a model must be built for an average frequency. This average frequency was chosen as the midpoint of the frequency sweep which is 77.76755 GHz. With this frequency only being 767.55 MHz off from the high and low frequencies of the chirp, it was not anticipated that this would cause significant error in the moisture content and a study of the models was conducted to confirm this.

The models used for this study were built using density and permittivity data of TAPPI hand sheet samples made from unrefined hardwood pulp. These samples were prepared by collaborators in the Multi-Scale Heat Transfer Laboratory at WPI. This study focused on the accuracy of the models at the high range of moisture content from 110 DBMC to 300 DBMC as this is the range of moisture contents that samples could reach at the inlet of the smart dryer where the sensor will be installed.

Figure 77 shows the moisture content models built for the IWR1642 based moisture sensor relating the fraction of the reference signal, from 0 to 1, to the moisture content of a sample of unrefined hardwood hand sheet paper of thickness 590 µm at 77 GHz, 78.5351 GHz, and 77.76755 GHz. The variation in the models between these frequencies is very low with the average difference in predicted moisture content between the 3 frequencies for both models shown in Figure 78. This shows that the error in predicted moisture content due to the averaging of the sweep frequency is less than 1 DBMC, with Bruggeman's model having a maximum difference of 0.053 DBMC and Looyenga's model having a maximum difference of 0.069 DBMC. These errors are predicted to be insignificant compared to other uncertainties and systematic errors.

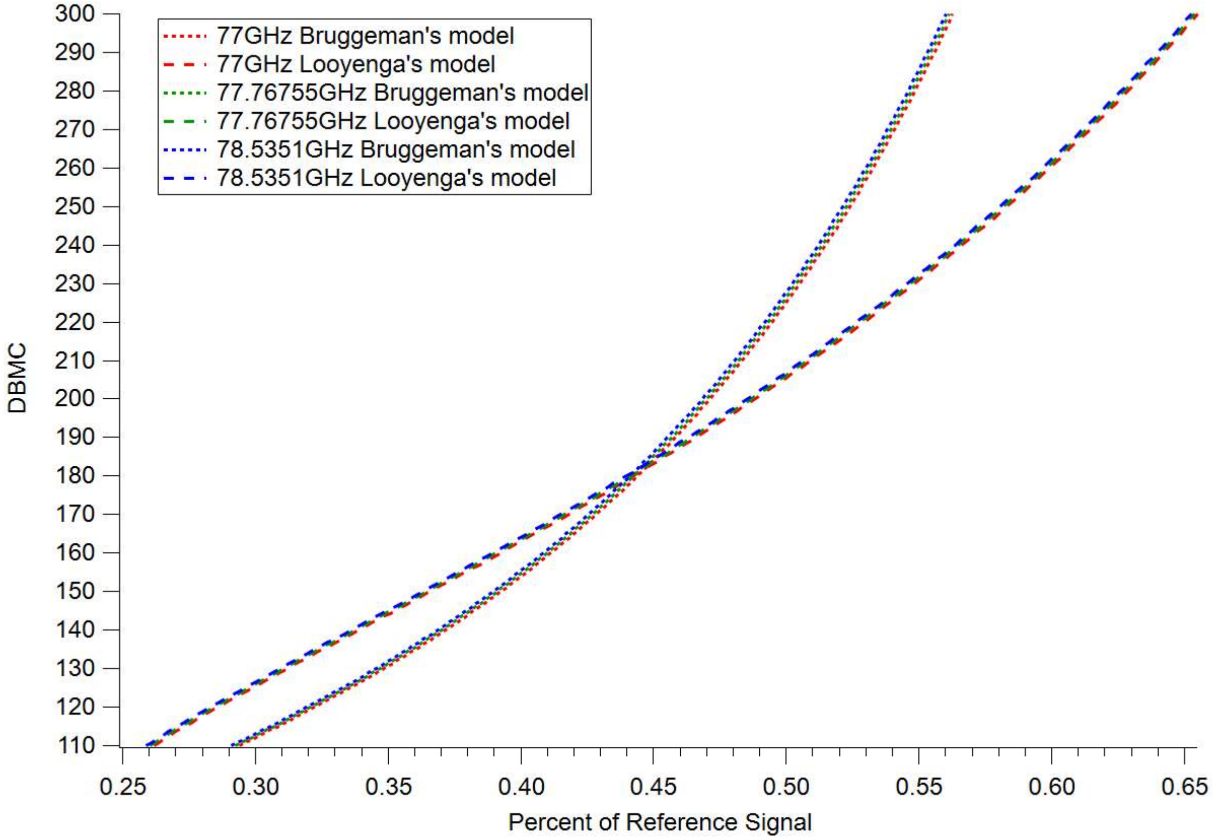

Figure 77. Moisture content models built for the IWR1642 based moisture sensor at 77 GHz, 78.5351 GHz, and 77.76755 GHz.

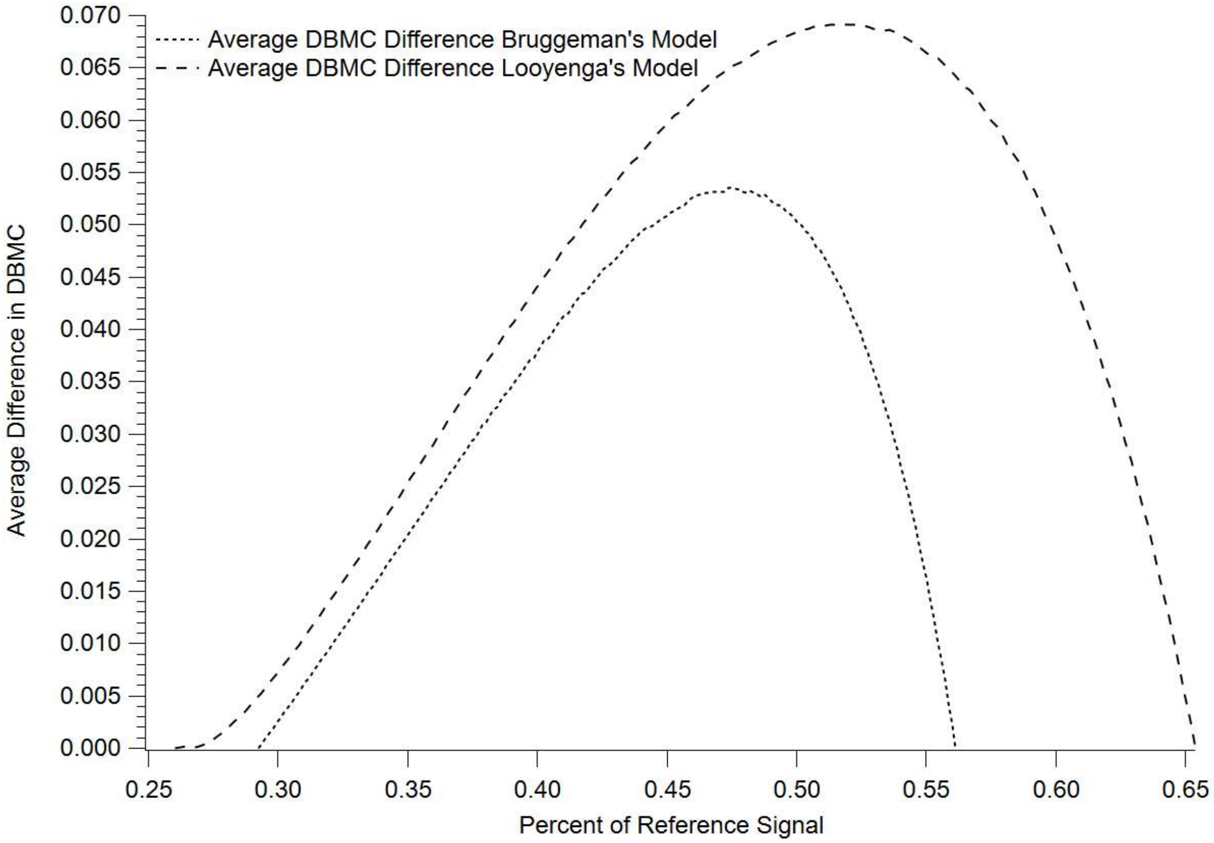

Figure 78. Average difference in the moisture content models built for the IWR1642 based moisture sensor built at the minimum, maximum, and average frequency.

4.3.2.3 Sensor Software

To effectively implement the IWR1642 board as a moisture sensor, a package of MATLAB scripts was written. These scripts control the collection and processing of the raw radar signal to measure the returned signal strength as a percentage of the reference signal, as well as building sample moisture models and producing moisture content estimations. When ran the script will prompt the user to specify if the data being collected is a reference or sample measurement, the script expects that the user will take a reference measurement when running the script for the first time and failing to do so will cause an error in the moisture estimates.

Once the user has specified the type of measurement they will be making, they are asked to provide a file name for the data. This file name will be the basis for names of all the data produced during a measurement, for example if the user takes a reference measurement and gives the filename “11-22_Reference”, all data produced from that measurement will have names of the form “11-22_Reference_XX” with XX being a placeholder for the data type identifier. After being supplied with a filename, the script will send Lua commands to mmWave studio to initialize the IWR1642BOOST and DCA1000EVM and prompt a data collection.

In the case of a reference measurement, the stainless-steel couch plate to which the hand sheet paper will be bonded to will be placed centered below the antennae of the IWR1642BOOST board and the user will set the sample parameters in the header of the MATLAB script. Then they will run the script, indicate that this is a reference measurement, and provide an appropriate file name. The script will then prompt the radar to run a data collection and save the raw data produced as “filename_rawADC.csv” and “filename_Raw_0.bin” in the current file directory. The script then runs this raw data through a processing script supplied by Texas Instruments which processes the raw data and provides signal power versus range information. This power and range information are saved as “filename_Power.csv” and “filename_Range.csv” respectively. The power data, which is in units of dB, are then averaged and stored locally as “ReferenceAvg” for comparison with sample measurements.

It is anticipated that then the user will use the couch plate measured as the reference in the preparation of a hand sheet paper following the TAPPI 205 standard [123]. The user will then need to measure the thickness, temperature and provide an estimate of the density of the sample when dry, this estimate will primarily depend on the type of pulp used. The user will then set the thickness, temperature, density, and pulp type in the script. After setting the sample parameters, the user will then position the sample below the antennae of the IWR1642BOOST board, taking care to position the sample in roughly the same orientation and position as in the reference measurement. The user will then rerun the control script this time indicating that they are making a sample measurement and providing an appropriate filename.

As before, the script will collect, process and save the data from the radar. Once the sample data is collected and processed the script will call the transmission model function, supplying the sample parameters set by the user. This function builds the percent signal strength vs sample DBMC model as discussed before using the 3-parameter Debye model, estimates of the permittivity of the dry sample obtained from TDS measurements, and using both Bruggeman's and Looyenga's models of effective medium theory. The script will then reinterpret this model as sample DBMC as a function of percent signal strength in the high range of moisture contents. This moisture content range can be set by the user, but care must be taken that the range is fully within one of the two domains of the model as described in section 4.2.2.1. A high order polynomial fit is then taken of the abbreviated DBMC vs percent signal strength function and the coefficients of this fit are returned to the control script. These polynomial fits can be seen in Figure 79. The models were fitted to 7th degree polynomials which generated 8 function coefficients, $C_1 \rightarrow C_8$, which plug into equation (86). The maximum deviation in moisture content estimates generated by these fits were found to be 0.114 DBMC for Looyenga's model and 0.0011 DBMC for Bruggeman's model. These errors can be reduced by increasing the terms of the fitted polynomials.

$$\begin{aligned}\text{DBMC} = {} & C_1 * \%_{\text{ref}}^7 + C_2 * \%_{\text{ref}}^6 + C_3 * \%_{\text{ref}}^5 + C_4 * \%_{\text{ref}}^4 + +C_5 * \%_{\text{ref}}^3 + C_6 * \%_{\text{ref}}^2 + C_7 * \%_{\text{ref}} \\ & + C_8\end{aligned} \tag{86}$$

After obtaining the moisture model coefficients the script will then subtract the average of the power of the reference measurement from the average power of the sample measurement to get the average loss in dB. This loss in dB ($\mathrm{dB_{loss}}$) is then converted to percent of reference ($\%_{\mathrm{ref}}$) following equation (87).

$$\%_{\mathrm{ref}} = 10^{\frac{\mathrm{dB_{loss}}}{10}} \tag{87}$$

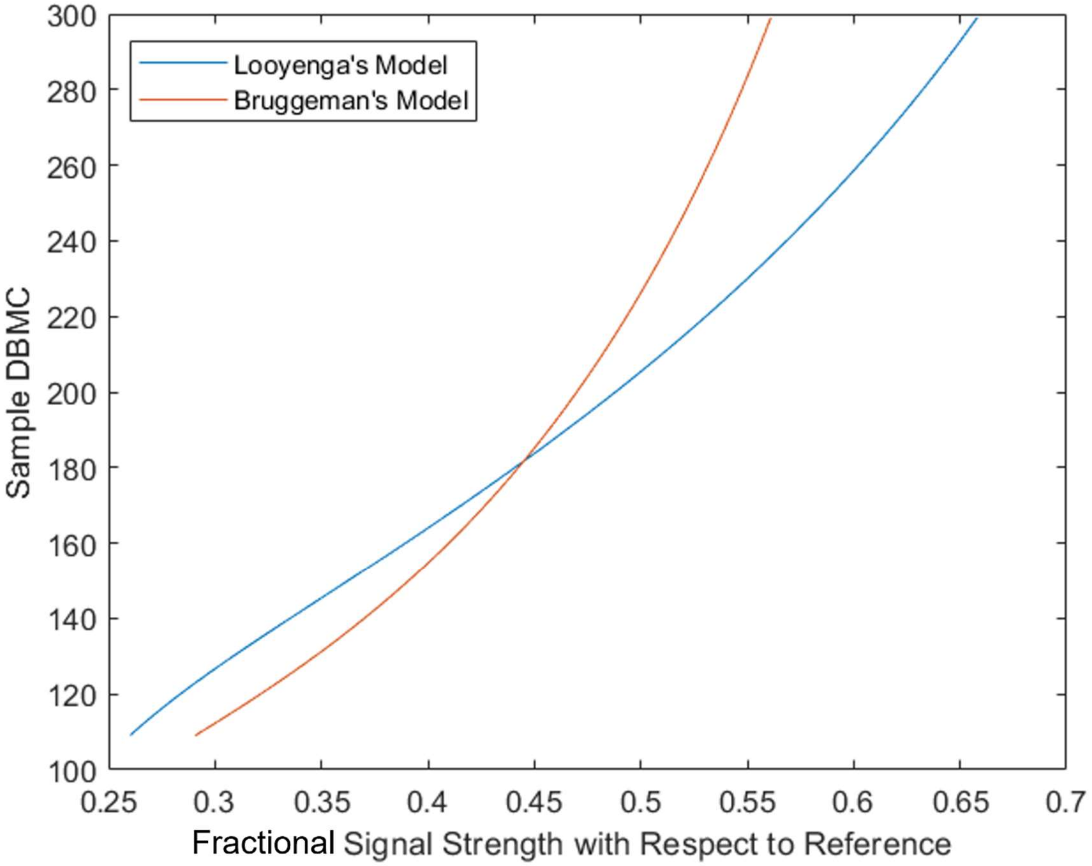

Figure 79. The 7th order polynomial fits of the moisture models used to estimate sample moisture content from measurements of fractional signal strength with respect to a reference measurement.

With this measured $\%_{\mathrm{ref}}$ and the coefficients from the transmission model, the script gives estimates of the moisture content of the sample and prints them to the command line and saves them to a text file.

4.3.3 Sensor Performance

To validate the efficacy of the IWR1642 based moisture system, measurements of a known sample were needed. A block diagram of the experimental setup used to make these measurements can be seen in Figure 80. The dry-basis moisture content of the sample was measured gravimetrically using a Sartorius Entris II balanced connected to the control computer, and the moisture sensor was secured using optical posts and positioned over the balance at a distance of 12 cm. The sample used was a 550 μm paper hand sheet made of unrefined hardwood pulp which had been previously dried in other experiments. The sample was hydrated using MilliQ deionized water to a starting DBMC of 215 DBMC. The moisture sensor control script was modified to read the output of the balance and calculate the true DBMC and calculate the error in the moisture content estimates from both the Bruggeman and Looyenga based moisture models. The sample was allowed to dry in the ambient conditions in the laboratory (20 °C, 15% Humidity) for approximately 1 hour, with measurements taken every 5 minutes.

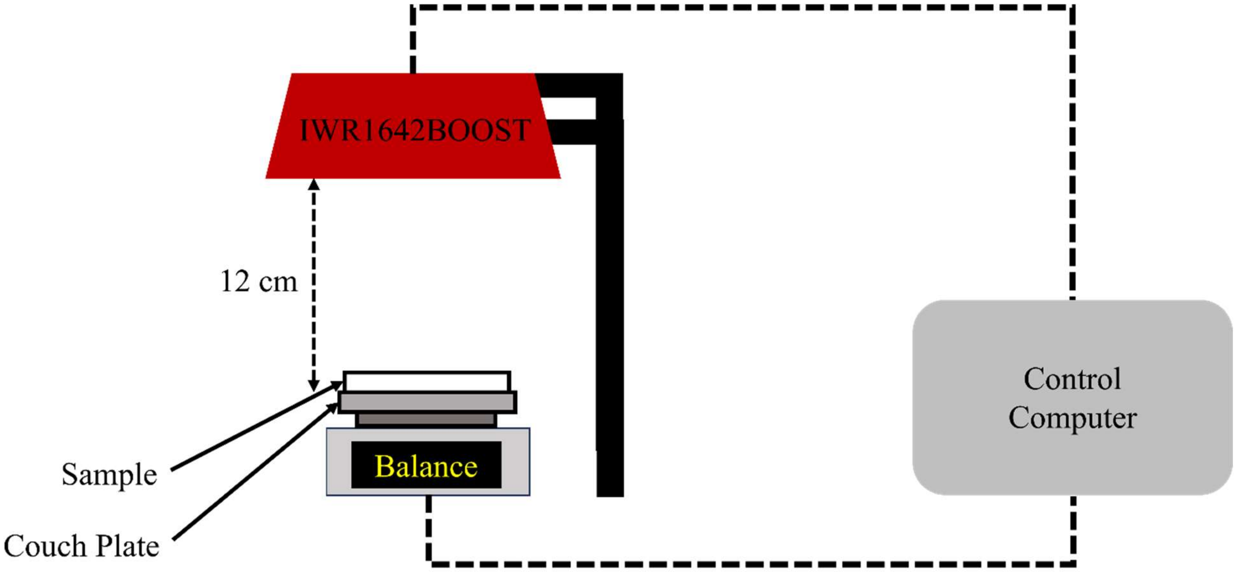

Figure 80. A block diagram of the setup used to test the IWR1642 based moisture sensor.

Over the course of the 1-hour experiment, the sensor began to heat up which affected the output power. This caused significant error in the moisture estimations and approximately 30 minutes into the experiment, the sensor had to be recalibrated by taking a new reference measurement. Figure 81 shows the results from this experiment while Figure 82 shows the percent error of the two models used by the moisture sensor.

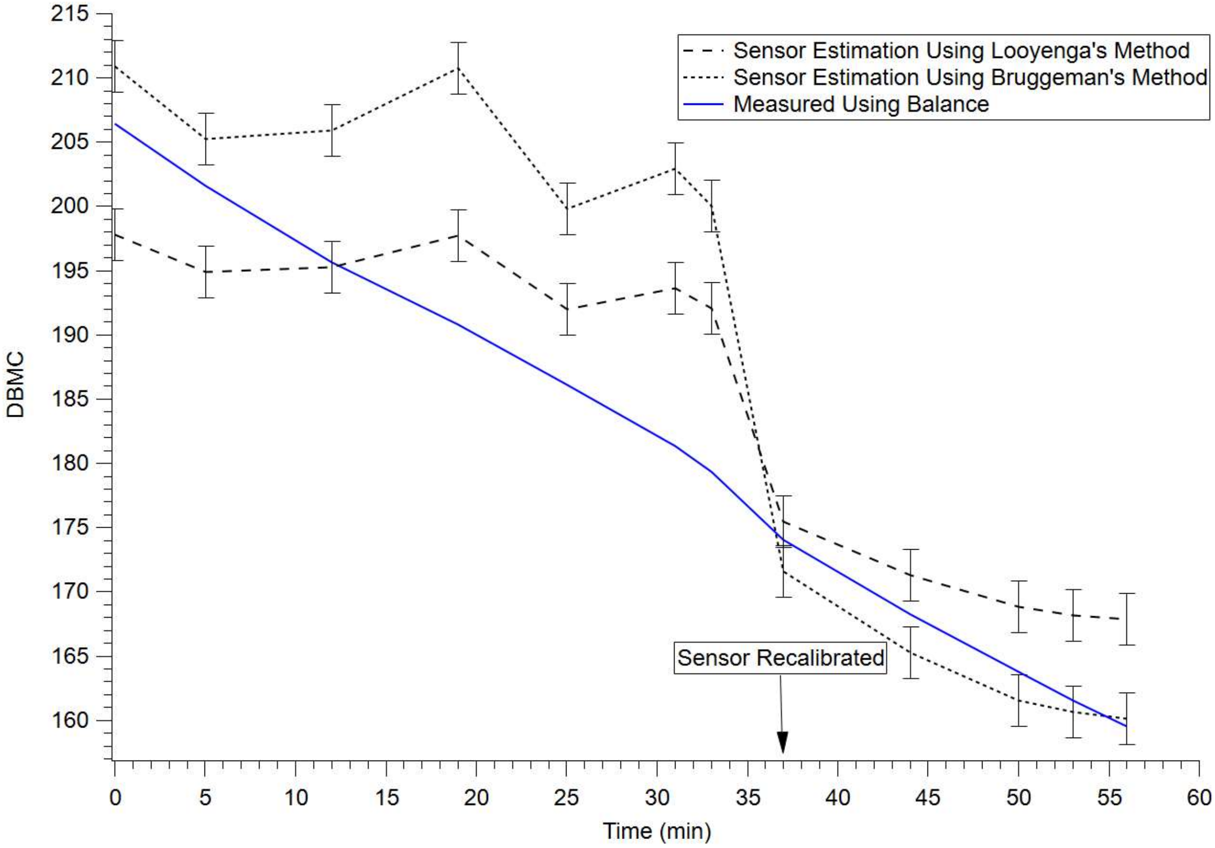

Figure 81. A comparison of measurements of the dry-basis moisture content of a sample using the gravimetric method (blue) and the IWR1642 based moisture sensor (black). With the two effective medium models presented. Note the increase in the accuracy of the moisture sensor after recalibration. The error bars of the two models represent a range of ±2 DBMC.

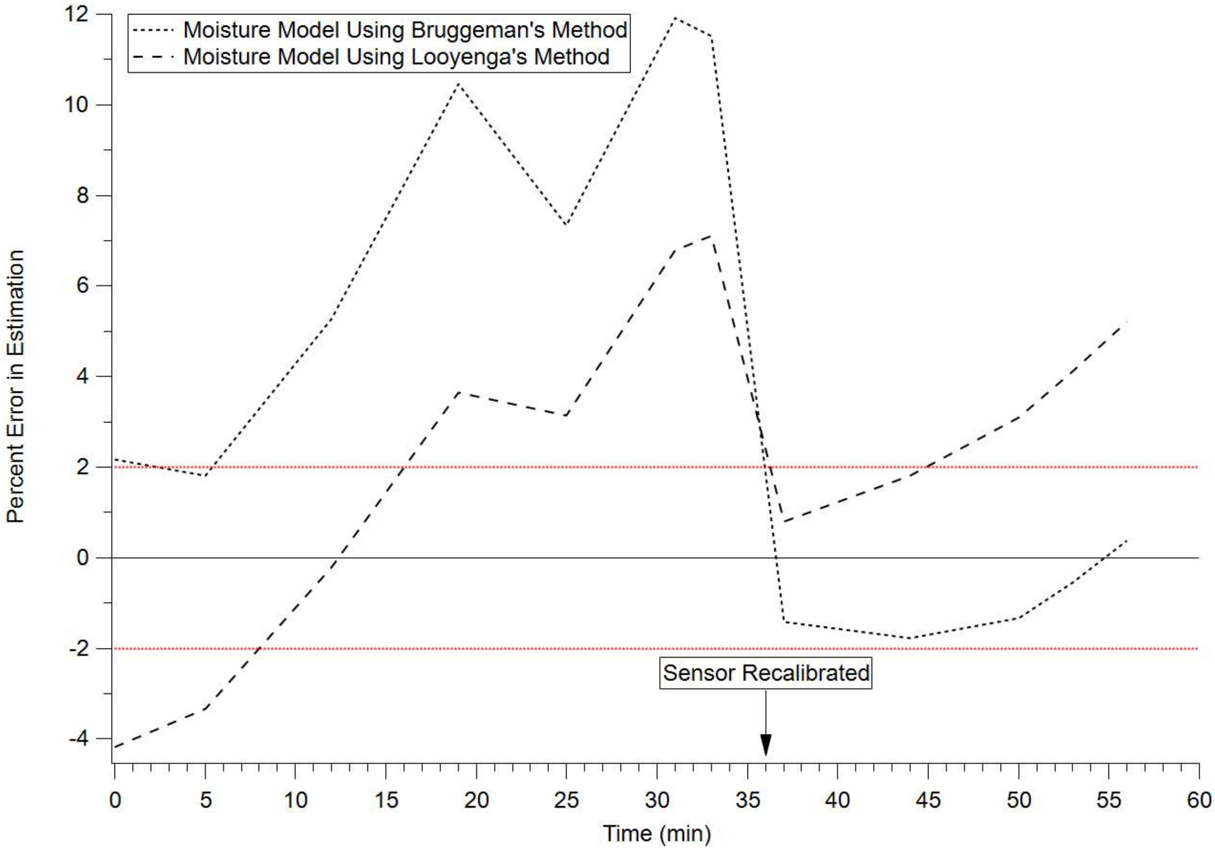

Figure 82. A comparison of the percent error in the estimates from the IWR1642 moisture sensor using the two effective medium models. Note the significant decrease in percent error of both models after sensor recalibration. The two red lines represent the desired accuracy of ±2%.

Reviewing the data, a clear trend can be seen beginning between minute 5 and 10 where the estimates from the moisture sensor begin to vary significantly from the real value. This variance is most likely due to drift in the output power of the radar. This drift could be caused by heating of the components during long-term use or may simply be a drift inherent to the radar. In either case this should not seriously impact the sensors effectiveness on the smart dryer as it will be recalibrated right before a sample is measured. Looking at the data after the sensor recalibration at minute 37, it can be seen that the sensor performs quite well at estimating the moisture content of the sample. The moisture model built using Bruggeman’s effective medium model does particularly well, with an average percent error of only -0.95%.

4.3.4 Sensor Integration

With the performance of the IWR based moisture sensor proved in the laboratory, the sensor could be integrated into the smart dryer testbed. To mount the sensor at the inlet of the dryer, a simple frame was assembled from extruded aluminum channel. The channel allowed for the height of the sensor relative to the dryer's conveyor belt to be adjusted easily, the frame was also made to be easily dissembled and reassembled at the outlet in the case that future work sought to apply the sensor there. A computer with the appropriate control software and scripts was given to the team of smart dryer operators and demonstrations of the sensor were made. Figure 83 shows the sensor installed on the smart dryer and measuring a hand sheet of paper. Upon installation, hand sheet samples made from refined hardwood and unrefined softwood pulp were collected. These samples were measured using TDS and their bone dry relative permittivities were calculated. This data was used to expand the sample compatibility of the sensor.

With its installation on the smart dryer complete, the IWR based moisture sensor can now be used as a complimentary moisture measurement method in conjunction with other novel methods. These sensors will support the overall goal of the smart dryer, to develop innovative and efficient drying methods and techniques.

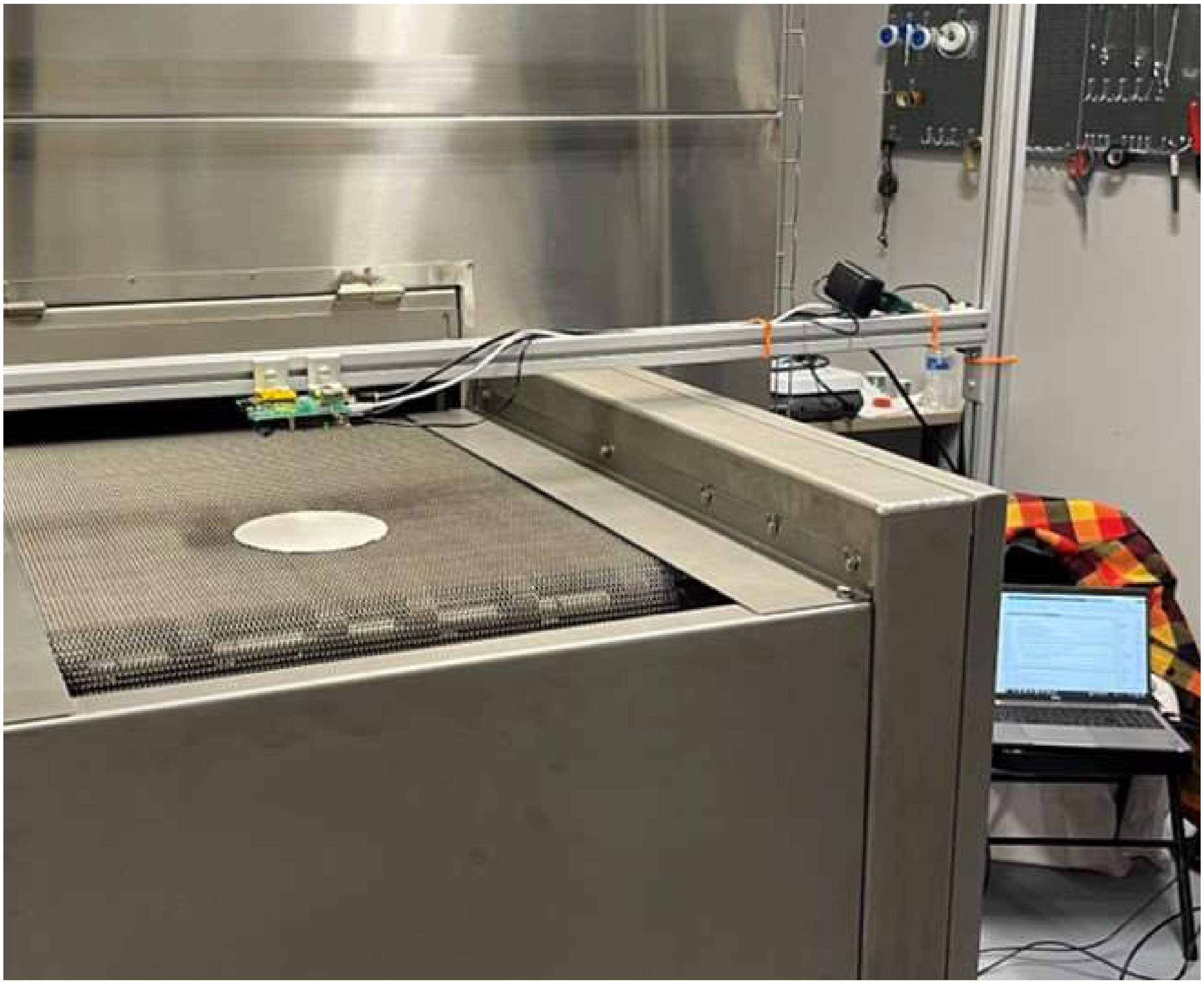

Figure 83. A photo of the sensor installed on the smart dryer testbed with the control computer in the background and a hand sheet of paper on a couch plate below the sensor.

4.4 CONCLUSIONS AND FUTURE WORK

This work has provided the theoretical background and calibration models for the development of non-contact moisture sensors using THz electromagnetic radiation, for thin, non-conductive samples with a focus on paper. The calibration models were made by combining the Debye relaxation model for the relative permittivity of liquid water with effective medium models and experimentally measured sample data. The anticipated accuracy of the calibration models was measured using THz time domain spectroscopy and found to be suitable for industrial needs.

Finally, this work has detailed the development and implementation of such a moisture sensor using a Texas Instruments IWR1642 automotive radar development board operating at approximately 77 GHz. This moisture sensor achieved an average percent error in moisture measurements of less than 1% when appropriately calibrated, exceeding the stated accuracy goal of 2%. This work should provide the basis for the development of new commercializable moisture sensors utilizing THz electromagnetic radiation.

The moisture models developed and presented here should allow for the development of frequency or time domain electromagnetic moisture sensors operating in transmission, reflection, or two-pass transmission mode and within the bandwidth of 50 GHz-3 THz. These models should also provide the framework for significant development of sensors operating outside of this bandwidth.

4.4.1 Sensor Limitations and Recommendations

Despite meeting the stated accuracy goal of 2% error, the sensor and models developed in this work still have some limitations that affect the accuracy of moisture measurements. One fundamental limitation that exists in sensor moisture models comes from the 3-parameter Debye model. As mentioned in section 2.5, there is no theoretical explanation which accounts for the third relaxation time, and although it provides a good estimate of the permittivity of liquid water at high frequencies, it may be revealed in future work that some other estimate provides a more theoretically sound and accurate description. In this case the models will need to be updated. This 3-parameter Debye model also limits the validity of the sensor models to the bandwidth from DC to 3 THz.

Another limitation of the sensor models comes from the effective medium models. The models used, Bruggeman’s and Looyenga’s models, allow for the modelling of hybrid materials made up of an infinite number of constituent materials. The models developed in this work use only two constituent materials to describe wet paper. While on the surface, it seems that this should be sufficient, it is predicted that the associated water in the wet sample should behave differently than liquid water and should be modelled separately. This effect was not directly observed during the sensor operation, but this is most likely due to operating at high moisture contents where the ratio of liquid water to associated water is high. It is anticipated that this will become relevant when operating at low moisture contents.

The measurements of the relative permittivities of the dry samples by TDS necessary for the models, also imposes some limitations. The TDS system available at WPI provides useful permittivity data from 300 GHz to 2.2 THz. This limitation limits the bandwidth over which the models can be built if it cannot be assumed that the dry sample has a nonvarying permittivity over a large bandwidth. If it can be assumed that the permittivity does not significantly vary with frequency, operating outside of the bandwidth of the TDS system still may have extra inaccuracies caused by extrapolating the permittivity. This issue could be avoided by using other methods to measure the permittivity of samples, such as by network analyzer.

The final key model limitation comes from the data that must be supplied by the operator when using the moisture sensor. The operator must supply accurate measurements of the sample thickness, dry density, and temperature. Any errors in these measurements will seriously impact the accuracy of the models and subsequently the sensor.

The IWR1642BOOST board chosen as the platform to develop a moisture content sensor for implementation on the smart dryer comes with its own limitations which affect performance. As a radar evaluation board meant to show off the multi-object tracking capabilities of the IWR1642 radar, the antennae on the board have a very large gain pattern resulting in a quickly diverging beam. This quickly diverging beam means that the sensor must be placed very close to the sample to not over illuminate the area around the sample and degrade its sensitivity. This could possibly be fixed by developing some horn style antennae to attach to the board to improve directionality. More practically, a new board should be developed and manufactured which is more tailored to the moisture sensing application with more narrow patch antennae. This new board could also possibly deal with another limitation of the IWR1642BOOST board which is its long-term power stability. As seen in section 4.3.3, the output power of the board is only stable for approximately 25 minutes. While this is not anticipated to be an issue when operating on the smart dryer, it should be dealt with. The exact source of the power drift was not found during the course of this work, but it is suspected that it may have to do with the heating of the board during operation.

A limitation of the sensor that is inherent to its method of comparative measurements is its sensitivity to its reference or calibration measurement. If there is significant variation in the optical path between reference and sample measurements, the sensor can only attribute these changes to the moisture content of the sample. These changes can also be caused by deviations in the placement and orientation of the reference plate and the sample. Due to this limitation, the sensor in its current form is most suited for the batch drying process used in the smart dryer.

4.4.2 Future Applications

As stated before, the models developed in this work should be applicable to over a wide bandwidth and should be valid for many samples and measurement schemes. This leaves the field of future applications quite open. Some applications of particular interest that this work could be applied to are in the development of moisture sensors for a wide range of industry relevant samples, and in the development of a THz based water activity meter.

Being a part of the Center for Advanced Research in Drying (CARD) gives WPI unique access to industrial partners who work with a variety of materials which need to be dried. As such, future studies continuing this work should focus on qualifying these models to be used with samples relevant to these industrial partners. This work could possibly lead to the eventual adoption of THz moisture sensors by industry.

Another area where this work may be applied is in the study of water activity in samples. Water activity is the ratio of the partial vapor pressure of a sample and the partial vapor pressure of pure liquid water. It is a metric used in food science to ascertain the amount of free water in a sample and is important in predicting shelf stability and spoilage rate. Currently there are few inline water activity sensors on the market, with production facilities typically taking samples of products periodically during production and measuring their water activity in a laboratory. The THz moisture content method presented in this work may be used to develop a new in line method of measuring water activity. If the associated water in a sample has an anomalously low permittivity, as shown in literature, and if this low permittivity is known, a 3-material moisture model could be developed to measure the volume of both the free and associated water in a sample. From this measurement, the ratio of the two states of water can be calculated and the water activity can be calculated. If successful, such a sensor could be invaluable to industrial food production, especially in the production of exceptionally long shelf life items such as rations or emergency foods.

5 CONCLUSIONS

This dissertation reports the measurement of water in porous, nonconductive materials with electromagnetic radiation in the THz band. Two studies were detailed, one focused broadband imaging of moisture distribution in carbonate sample for porosity imaging which produced first of their kind lateral porosity maps from time-domain spectroscopy as well as accurate measurements of porosity ratios. The other project focused on the development of moisture dependent transmission models using effective medium theory, these models were developed to support the development of moisture content sensors based on THz spectroscopy for high accuracy high range moisture measurements on CARD's smart dryer test bed. This project resulted in the development and implementation of a non-contact moisture sensor able to achieve accuracies of within 2% error. The work from these two projects marks a step forward in the commercialization and implementation of THz as a sensing technology and should provide an adequate basis for the development of industry adoptable sensors for moisture measurements. As THz sources and detectors become more widely produced and their price decreases, fundamental studies such as the ones presented here will become increasingly useful to realize the promise of THz sensors.

6 PUBLICATIONS, POSTERS, AND PRESENTATIONS RESULTING FROM THIS WORK

Peer Reviewed Journal Publications:

1. Eichmann, S., Bouchard, J., Ow, H., O'Mullan, P., Petkie, D., Poitzsch, M. (2021). Terahertz Imaging to Map the Microporosity Distribution in Carbonate Rocks. Microscopy and Microanalysis, 27(S1), 2746-2748. DOI: 10.1017/S143192762100965X
2. Bouchard, J., Eichmann, S. L., Ow, H., Poitzsch, M., Petkie, D. T. (2022). Terahertz imaging for non-destructive porosity measurements of carbonate rocks. Scientific Reports, 12(1), 18018. DOI: 10.1038/s41598-022-22535-z
3. Eichmann, S., Bouchard, J., Ow, H., Petkie, D., Poitzsch, M. (2023). THz Imaging to Map the Microporosity Distribution in Carbonate Rocks. Petrophysics, DOI: 10.30632/PJV64N3-2023a8

Conference Presentations:

1. Bouchard, J., Petkie, D. T. (2020). Using Effective Medium Theory to Develop a Narrow-Band Terahertz Drying Monitor for Paper Manufacturing 22nd International Drying Symposium
2. Bouchard, J., Petkie, D. T. (2023). Investigation of Effective Medium Theories in the Far Infrared for Pulp and Paper Applications
   8th European Drying Conference

Conference Posters:

1. Bouchard, J., Petkie, D. T. (2022). Non-Contact Moisture Sensing for Pulp and Paper Manufacturing. 47th IRMMW-THz Conference

7 FUNDING ACKNOWLEDGEMENTS

The study of porosity in carbonate samples was sponsored by Aramco Americas

The study and development of the THz moisture models, and moisture sensor was financially supported by the U.S. Department of Energy, Office of Advanced Manufacturing, under Award Number DE-EE0009125

Data was collected using the LEAP@WPI/QCC core facility funded in part by a grant from the Massachusetts Manufacturing Innovation Initiative program

8 REFERENCES

1. Dieter, C.A., *Water availability and use science program: Estimated use of water in the United States in 2015*. 2018: Geological Survey.
2. Miao, P., et al., *Report on literature review of recent development in loss on drying method for moisture determination.* 2014.
3. Curcio, J.A. and C.C. Petty, *The near infrared absorption spectrum of liquid water.* JOSA, 1951. **41**(5): p. 302-304.
4. Leblon, B., et al., *A review of near-infrared spectroscopy for monitoring moisture content and density of solid wood.* The forestry chronicle, 2013. **89**(5): p. 595-606.
5. Tsuchikawa, S., K. Hayashi, and S. Tsutsumi, *Nondestructive measurement of the subsurface structure of biological material having cellular structure by using near-infrared spectroscopy.* Applied Spectroscopy, 1996. **50**(9): p. 1117-1124.
6. Tsuchikawa, S., et al., *Near-infrared spectroscopic study of the physical and mechanical properties of wood with meso-and micro-scale anatomical observation.* Applied Spectroscopy, 2005. **59**(1): p. 86-93.
7. Sykes, R., et al., *Prediction of loblolly pine wood properties using transmittance near-infrared spectroscopy.* Canadian Journal of Forest Research, 2005. **35**(10): p. 2423-2431.
8. Yasushi, I., et al., *A High-precision IR Moisture Sensor for the B/M9000VP System.* 2013.
9. Analytics, K., *NIR 6000 Series Sensors*. 2023, KPM Analytics: https://www.kpmanalytics.com/products/nir-6000-series.
10. Achata, E., et al., *A study on the application of near infrared hyperspectral chemical imaging for monitoring moisture content and water activity in low moisture systems.* Molecules, 2015. **20**(2): p. 2611-2621.
11. Sensors, F., *OMNIR Brochure*. 2023, Finna Sensors.
12. Hinz, T., et al., *Development of a microwave moisture sensor for application in the food industry.* LWT-Food Science and Technology, 1996. **29**(4): p. 316-325.
13. Kraszewski, A., *Microwave aquametry: an effective tool for nondestructive moisture sensing.* Subsurface sensing technologies and applications, 2001. **2**: p. 347-362.
14. Trabelsi, S., A.W. Kraszewski, and S.O. Nelson, *New calibration technique for microwave moisture sensors.* IEEE Transactions on Instrumentation and Measurement, 2001. **50**(4): p. 877-881.
15. Bogart, J., *Learn the Six Methods For Determining Moisture. Advantages, Deficiencies and Who Uses Each Method*, ed. Kett. 2023, www.kett.com: Kett.
16. Bose, J.C., *Jagadish chandra bose.* A Life Sketch, 1958.
17. Van Exter, M., C. Fattinger, and D. Grischkowsky, *Terahertz time-domain spectroscopy of water vapor.* Optics letters, 1989. **14**(20): p. 1128-1130.
18. Hu, B.B. and M.C. Nuss, *Imaging with terahertz waves.* Optics letters, 1995. **20**(16): p. 1716-1718.
19. Dang, S., et al., *What should 6G be?* Nature Electronics, 2020. **3**(1): p. 20-29.
20. Le, H., et al. *A 77 GHz CMOS low noise amplifier for automotive radar receiver*. in *2012 IEEE International Symposium on Radio-Frequency Integration Technology (RFIT)*. 2012. IEEE.

21. Gresham, I., et al., *A compact manufacturable 76-77-GHz radar module for commercial ACC applications.* IEEE Transactions on Microwave Theory and Techniques, 2001. **49**(1): p. 44-58.
22. Maxwell, J.C., *VIII. A dynamical theory of the electromagnetic field.* Philosophical transactions of the Royal Society of London, 1865(155): p. 459-512.
23. Appleyard, R., *Pioneers of electrical communication*. 1968: Books for Libraries Press.
24. Capri, A.Z., *Quips, quotes, and quanta: an anecdotal history of physics*. 2011: World Scientific.
25. Ganguly, B., *Microwave Apparatus*, MicrowaveApparatus.jpg, Editor. 2011: wikipedia.org/wiki/Spark-gap_transmitter.
26. Ramaseshan, S., *The centennial of the discovery of millimetre waves by Jagadis Chandra Bose (1858–1937).* Current Science, 1996. **70**(2): p. 172-175.
27. Fitzgerald, G.F., *The scientific writings of the late George Francis FitzGerald*. 1902: Hodges, Figgis, & Company, Limited.
28. Brodsky, I. *How Reginald Fessenden put wireless on the right technological footing*. in *IEEE GLOBECOM 2008-2008 IEEE Global Telecommunications Conference*. 2008. IEEE.
29. Fleming, J.A., *The principles of electric wave telegraphy*. 1910: New York.
30. Hull, A.W., *The magnetron.* Journal of the American Institute of Electrical Engineers, 1921. **40**(9): p. 715-723.
31. Nicolson, A.M., *Generating and transmitting electric currents*. 1940, Google Patents.
32. Marrison, W.A., *The evolution of the quartz crystal clock.* The Bell System Technical Journal, 1948. **27**(3): p. 510-588.
33. Crecraft, D. and S. Gergely, *Analog Electronics: circuits, systems and signal processing*. 2002: Elsevier.
34. Sullivan, D. *Time and frequency measurement at NIST: The first 100 years*. in *Proceedings of the 2001 IEEE International Frequncy Control Symposium and PDA Exhibition (Cat. No. 01CH37218)*. 2001. IEEE.
35. Burman, R. *Summary of magnetron development*. in *2010 International Conference on the Origins and Evolution of the Cavity Magnetron*. 2010. IEEE.
36. Dorf, R.C., *The Electrical Engineering Handbook-Six Volume Set*. 2018: CRC press.
37. Turner, L.W., *Electronics engineer's reference book*. 2013: Butterworth-Heinemann.
38. Dunster, I., *Diagram of a resonant cavity magnetron*, D.o.a.r.c. magnetron, Editor. 2008, Wikipedia: https://commons.wikimedia.org/wiki/File:Resonant_Cavity_Magnetron_Diagram.svg.
39. Epsztein, B., *Backward flow travelling wave devices.* French Patent FRD1, 1953. **35**(379): p. 19.
40. Kompfner, R. and N. Williams, *Backward-wave tubes.* Proceedings of the IRE, 1953. **41**(11): p. 1602-1611.
41. Howard, F.S.R.S. and C.H.D. Vaughan, *Navy Electricity and Electronics Training Series*. 1998.
42. Johnson, H.R., *Backward-wave oscillators.* Proceedings of the IRE, 1955. **43**(6): p. 684-697.
43. Gunn, J.B., *Microwave oscillations of current in III–V semiconductors.* Solid State Communications, 1963. **1**(4): p. 88-91.

44. Gružinskis, V., et al. *Gunn effect and THz frequency power generation in n+-n-n+ GaN structures*. in *Materials Science Forum*. 1999. Trans Tech Publications.
45. Diodes, V., *Zero Bias Detectors - VDI Model: WR0.65ZBD/WR0.65ZBD-F* 2023, Virginia Diodes: https://www.vadiodes.com/en/products/detectors?id=220.
46. Pierret, R.F., *Semiconductor device fundamentals*. 1996: Pearson Education India.
47. Liddiard, K., *Thin-film resistance bolometer IR detectors.* Infrared Physics, 1984. **24**(1): p. 57-64.
48. Wang, F., et al., *A high-efficiency regime for gas-phase terahertz lasers.* Proceedings of the National Academy of Sciences, 2018. **115**(26): p. 6614-6619.
49. Weiss, C., et al., *Tuning characteristics of narrowband THz radiation generated via optical rectification in periodically poled lithium niobate.* Optics Express, 2001. **8**(9): p. 497-502.
50. Dai, J., J. Liu, and X.-C. Zhang, *Terahertz wave air photonics: terahertz wave generation and detection with laser-induced gas plasma.* IEEE Journal of selected topics in Quantum Electronics, 2010. **17**(1): p. 183-190.
51. Burford, N.M. and M.O. El-Shenawee, *Review of terahertz photoconductive antenna technology.* Optical Engineering, 2017. **56**(1): p. 010901-010901.
52. Naftaly, M., N. Vieweg, and A. Deninger, *Industrial applications of terahertz sensing: State of play.* Sensors, 2019. **19**(19): p. 4203.
53. Guillet, J.-P., et al., *Art painting diagnostic before restoration with terahertz and millimeter waves.* Journal of Infrared, Millimeter, and Terahertz Waves, 2017. **38**: p. 369-379.
54. Yang, Z., et al., *Study on an artificial phenomenon observed in terahertz biological imaging.* Biomedical Optics Express, 2021. **12**(6): p. 3133-3141.
55. Zhang, Y., et al., *Continuous-wave THz imaging for biomedical samples.* Applied Sciences, 2020. **11**(1): p. 71.
56. Federici, J.F., et al., *THz imaging and sensing for security applications—explosives, weapons and drugs.* Semiconductor science and technology, 2005. **20**(7): p. S266.
57. Pickwell, E. and V. Wallace, *Biomedical applications of terahertz technology.* Journal of Physics D: Applied Physics, 2006. **39**(17): p. R301.
58. Amenabar, I., F. Lopez, and A. Mendikute, *In introductory review to THz non-destructive testing of composite mater.* Journal of Infrared, Millimeter, and Terahertz Waves, 2013. **34**: p. 152-169.
59. Stanze, D., et al., *Multilayer thickness determination using continuous wave THz spectroscopy.* IEEE Transactions on Terahertz Science and Technology, 2014. **4**(6): p. 696-701.
60. Kashyap, M., et al. *Quantifying relative moisture content in dielectric models using CW-THz spectroscopy and supervised machine learning regression*. in *Terahertz Emitters, Receivers, and Applications XII*. 2021. SPIE.
61. Vassilev, V., et al., *A mm-wave sensor for remote measurement of moisture in thin paper layers.* IEEE Transactions on Terahertz Science and Technology, 2015. **5**(5): p. 770-778.
62. Systems, S.R., *Lock-In Amplifier Basics*. 2020, Stanford Research Systems: thinksrs.com.
63. Kurtz, S.R. *Mixers as Phase Detectors*. The Communications Edge, 1978.
64. Roggenbuck, A., et al., *Coherent broadband continuous-wave terahertz spectroscopy on solid-state samples.* New Journal of Physics, 2010. **12**(4): p. 043017.

65. Auston, D.H., et al., *Cherenkov radiation from femtosecond optical pulses in electro-optic media.* Physical Review Letters, 1984. **53**(16): p. 1555.
66. Van Exter, M., C. Fattinger, and D. Grischkowsky, *High-brightness terahertz beams characterized with an ultrafast detector.* Applied Physics Letters, 1989. **55**(4): p. 337-339.
67. Zhang, Y., et al., *A broadband THz-TDS system based on DSTMS emitter and LTG InGaAs/InAlAs photoconductive antenna detector.* Scientific Reports, 2016. **6**(1): p. 26949.
68. Wilk, R., et al., *Highly accurate THz time-domain spectroscopy of multilayer structures.* IEEE Journal of Selected Topics in Quantum Electronics, 2008. **14**(2): p. 392-398.
69. Mossotti, O., *Mem. di Math. e di Fis. della Soc.* Ital. della Sci. Resid. Modena, 1850. **24**: p. 49-74.
70. Clausius, R., *The mechanical theory of heat*. 1879: Macmillan.
71. Garnett, J.M., *XII. Colours in metal glasses and in metallic films.* Philosophical Transactions of the Royal Society of London. Series A, Containing Papers of a Mathematical or Physical Character, 1904. **203**(359-371): p. 385-420.
72. Belyaev, B. and V. Tyurnev, *Electrodynamic calculation of effective electromagnetic parameters of a dielectric medium with metallic nanoparticles of a given size.* Journal of Experimental and Theoretical Physics, 2018. **127**: p. 608-619.
73. Choy, T.C., *Effective medium theory: principles and applications*. Vol. 165. 2015: Oxford University Press.
74. Kirkpatrick, S., *Electrical conduction in a nonconjugated polymer doped with SnCl4 and SbCl5.* Rev Mod Phys, 1973. **45**: p. 574-88.
75. Kirkpatrick, S., *Classical transport in disordered media: scaling and effective-medium theories.* Physical review letters, 1971. **27**(25): p. 1722.
76. Bottcher, C. and P. Bordewijk, *Theory of electric polarization. Amsterdam.* 1952.
77. Hernandez-Cardoso, G.G., A.K. Singh, and E. Castro-Camus, *Empirical comparison between effective medium theory models for the dielectric response of biological tissue at terahertz frequencies.* Applied Optics, 2020. **59**(13): p. D6-D11.
78. Scheller, M., et al. *Applications for effective medium theories in the terahertz regime*. in *2009 34th International Conference on Infrared, Millimeter, and Terahertz Waves*. 2009. IEEE.
79. Afsar, M. and J. Hasted, *Measurements of the optical constants of liquid H 2 O and D 2 O between 6 and 450 cm− 1.* JOSA, 1977. **67**(7): p. 902-904.
80. Pinkley, L.W., P. Sethna, and D. Williams, *Optical constants of water in the infrared: Influence of temperature.* JOSA, 1977. **67**(4): p. 494-499.
81. Afsar, M. and J. Hasted, *Submillimetre wave measurements of optical constants of water at various temperatures.* Infrared Physics, 1978. **18**(5-6): p. 835-841.
82. Simpson, O., B. Bean, and S. Perkowitz, *Far infrared optical constants of liquid water measured with an optically pumped laser.* JOSA, 1979. **69**(12): p. 1723-1726.
83. Zelsmann, H.R., *Temperature dependence of the optical constants for liquid H2O and D2O in the far IR region.* Journal of molecular structure, 1995. **350**(2): p. 95-114.
84. Bertie, J.E. and Z. Lan, *Infrared intensities of liquids XX: The intensity of the OH stretching band of liquid water revisited, and the best current values of the optical constants of H 2 O (l) at 25 C between 15,000 and 1 cm-1.* Applied Spectroscopy, 1996. **50**(8): p. 1047-1057.

85. Elton, D.C., *The origin of the Debye relaxation in liquid water and fitting the high frequency excess response.* Physical Chemistry Chemical Physics, 2017. **19**(28): p. 18739-18749.
86. Geiger, A., *Mechanisms of the molecular mobility of water.* Journal of molecular liquids, 2003. **106**(2-3): p. 131-146.
87. Laage, D. and J.T. Hynes, *A molecular jump mechanism of water reorientation.* Science, 2006. **311**(5762): p. 832-835.
88. Laage, D. and J.T. Hynes, *On the molecular mechanism of water reorientation.* The Journal of Physical Chemistry B, 2008. **112**(45): p. 14230-14242.
89. Ludwig, R., *Ionic Liquids—Revolutionary Potential for Chemistry?* ChemPhysChem: A European Journal of Chemical Physics and Physical Chemistry, 2006. **7**(7): p. 1415-1416.
90. Luzar, A. and D. Chandler, *Hydrogen-bond kinetics in liquid water.* Nature, 1996. **379**(6560): p. 55-57.
91. Ellison, W., *Permittivity of Pure Water, at Standard Atmospheric Pressure, over the Frequency Range–25THz and the Temperature Range–100° C.* Journal of physical and chemical reference data, 2007. **36**(1): p. 1-18.
92. Hamelin, J., J.B. Mehl, and M.R. Moldover, *The static dielectric constant of liquid water between 274 and 418 K near the saturated vapor pressure.* International journal of thermophysics, 1998. **19**(5): p. 1359-1380.
93. Bawuah, P., et al., *Terahertz-based porosity measurement of pharmaceutical tablets: a tutorial.* Journal of Infrared, Millimeter, and Terahertz Waves, 2020. **41**: p. 450-469.
94. Lu, X., et al., *Terahertz detection of porosity and porous microstructure in pharmaceutical tablets: A review.* International Journal of Pharmaceutics, 2020. **591**: p. 120006.
95. Naftaly, M., et al., *Measuring open porosity of porous materials using THz-TDS and an index-matching medium.* Sensors, 2020. **20**(11): p. 3120.
96. Crawley, D.A., et al., *Terahertz pulse imaging: a pilot study of potential applications in dentistry.* Caries research, 2003. **37**(5): p. 352-359.
97. Patzek, T.W., A.M. Saad, and A. Hassan, *Multimodal carbonates: Distribution of oil saturation in the microporous regions of arab formations.* Energies, 2022. **15**(3): p. 1243.
98. Pittman, E.D., *Microporosity in carbonate rocks.* AAPG Bulletin, 1971. **55**(10): p. 1873-1878.
99. Cantrell, D.L. and R.M. Hagerty, *Microporosity in arab formation carbonates, Saudi Arabia.* GeoArabia, 1999. **4**(2): p. 129-154.
100. Clerke, E.A., *Permeability, Relative Permeability, Microscopic Displacement Efficiency and Pore Geometry of M_1 Bimodal Pore Systems in Arab D Limestone.* SPE Journal, 2009. **14**(03): p. 524-531.
101. timmeko, *Oil and Natural Gas formation*, in *flikr*, O.a.N.G. formation, Editor. 2010, timmeko: flikr.
102. Schön, J.H., *Physical properties of rocks: Fundamentals and principles of petrophysics*. 2015: Elsevier.
103. Chopra, S., N. Chemingui, and R.D. Miller, *An introduction to this special section—Carbonates.* The Leading Edge, 2005. **24**(5): p. 488-489.

104. Jobe, T.D., *Sedimentology, chemostratigraphy and quantitative pore architecture in microporous carbonates: examples from a giant oil field offshore Abu Dhabi, UAE*. 2013: Colorado School of Mines.
105. Conner, W., et al., *Characterization of pore structure: porosimetry and sorption.* Langmuir, 1986. **2**(2): p. 151-154.
106. Dandekar, A.Y., *Petroleum reservoir rock and fluid properties*. 2013: CRC press.
107. Eslava, S., et al., *Characterization of a molecular sieve coating using ellipsometric porosimetry.* Langmuir, 2007. **23**(26): p. 12811-12816.
108. Funk, J., et al. *Core imaging—twenty five years of equipment, techniques, and applications of X-ray computed tomography (CT) for core analysis*. in *International Symposium of the Society of Core Analysts*. 2011.
109. Mei, L., S. Svanberg, and G. Somesfalean, *Combined optical porosimetry and gas absorption spectroscopy in gas-filled porous media using diode-laser-based frequency domain photon migration.* Optics express, 2012. **20**(15): p. 16942-16954.
110. Pahlevaninezhad, H., B. Heshmat, and T. Darcie, *Advances in terahertz waveguides and sources.* IEEE Photonics Journal, 2011. **3**(2): p. 307-310.
111. Ramsey, M., *Schlumberger oilfield glossary.* SLB, URL: https://glossary. slb. com/. Accessed April, 2019. **9**: p. 2023.
112. Svensson, T., et al., *Optical porosimetry and investigations of the porosity experienced by light interacting with porous media.* Optics letters, 2010. **35**(11): p. 1740-1742.
113. Tiab, D. and E.C. Donaldson, *Petrophysics: theory and practice of measuring reservoir rock and fluid transport properties*. 2015: Gulf professional publishing.
114. Berodier, E., J. Bizzozero, and A.C. Muller, *Mercury intrusion porosimetry.* A practical guide to microstructural analysis of cementitious materials, 2016. **419**.
115. Reedy, C.L. and C.L. Reedy, *High-resolution micro-CT with 3D image analysis for porosity characterization of historic bricks.* Heritage Science, 2022. **10**(1): p. 83.
116. Heshmat, B., et al., *Terahertz scattering and water absorption for porosimetry.* Optics express, 2017. **25**(22): p. 27370-27385.
117. Huygens, C., *Treatise on Light: In which are Explained the Causes of that which Occurs in Reflexion, & in Refraction. And Particularly in the Strange Refraction of Iceland Crystal*. 1912: MacMillan and Company, limited.
118. Miller, D.A., *Huygens's wave propagation principle corrected.* Optics letters, 1991. **16**(18): p. 1370-1372.
119. Bouchard, J., et al., *Terahertz imaging for non-destructive porosity measurements of carbonate rocks.* Scientific Reports, 2022. **12**(1): p. 18018.
120. Zhan, H., et al., *CaCO3, its reaction and carbonate rocks: terahertz spectroscopy investigation.* Journal of Geophysics and Engineering, 2016. **13**(5): p. 768-774.
121. Wilson, M.A., *Surface of an ooid-rich limestone*, in *Wikimedia*, OoidSurface, Editor. 2008, Wikimedia: https://commons.wikimedia.org/wiki/File:OoidSurface01.jpg.
122. Farokhpoor, R., et al. *Core cleaning and wettability restoration–selecting appropriate method*. in *E3S Web of Conferences*. 2023. EDP Sciences.
123. TAPPI, *Forming handsheets for physical tests of pulp*. 2006, TAPPI.
124. DOE, U., *Barriers to Industrial Energy Efficiency*, U.S.D.o. Energy, Editor. 2015: Washington D.C.
125. Hnin, K.K., et al., *Emerging food drying technologies with energy-saving characteristics: A review.* Drying Technology, 2018.

126. Farzad, M. and J. Yagoobi, *Drying of moist cookie doughs with innovative slot jet reattachment nozzle.* Drying Technology, 2021. **39**(2): p. 268-278.

127. Noori O'Connor, Z., J.S. Yagoobi, and B.S. Tilley, *Experimental study of paper drying with direct-contact ultrasound mechanism.* Drying Technology, 2023. **41**(8): p. 1351-1364.

128. Yang, M. and J. Yagoobi, *Enhancement of drying rate of moist porous media with dielectrophoresis mechanism.* Drying Technology, 2022. **40**(14): p. 2952-2963.

129. Banerjee, D., et al., *Diagnosing water content in paper by terahertz radiation.* Optics express, 2008. **16**(12): p. 9060-9066.

130. Mousavi, P., et al., *Simultaneous composition and thickness measurement of paper using terahertz time-domain spectroscopy.* Applied optics, 2009. **48**(33): p. 6541-6546.

131. Hattori, T., H. Kumon, and H. Tamazumi. *Terahertz spectroscopic characterization of paper*. in *35th International Conference on Infrared, Millimeter, and Terahertz Waves*. 2010. IEEE.

132. Merbold, H., D. Maas, and J. van Mechelen. *Multiparameter sensing of paper sheets using terahertz time-domain spectroscopy: Caliper, fiber orientation, moisture, and the role of spatial inhomogeneity*. in *2016 IEEE SENSORS*. 2016. IEEE.

133. Yasui, T. and T. Araki. *Sensitive measurement of water content in dry material based on low-frequency terahertz time-domain spectroscopy*. in *ICO20: OPtical Devices and Instruments*. 2005. SPIE.

134. Tayvah, U., et al., *Nelly: A user-friendly and open-source implementation of tree-based complex refractive index analysis for terahertz spectroscopy.* Analytical Chemistry, 2021. **93**(32): p. 11243-11250.

135. Bruder, J., et al., *IEEE standard for letter designations for radar-frequency bands.* IEEE Aerospace & Electronic Systems Society, 2003: p. 1-3.

136. Savitzky, A. and M.J. Golay, *Smoothing and differentiation of data by simplified least squares procedures.* Analytical chemistry, 1964. **36**(8): p. 1627-1639.

137. Wang, J., et al., *Terahertz relaxation polarization modeling of micro-water inside nano-modified dielectrics and imaging distribution of free/bound water.* Polymer Testing, 2023. **122**: p. 108031.

138. Kaatze, U., *Bound water: Evidence from and implications for the dielectric properties of aqueous solutions.* Journal of Molecular Liquids, 2011. **162**(3): p. 105-112.

139. Fumagalli, L., et al., *Anomalously low dielectric constant of confined water.* Science, 2018. **360**(6395): p. 1339-1342.

140. Texas Instruments, *IWR1642 Evaluation Module User's Guide*. 2020, Texas Instruments.

141. Texas Instruments, *IWR1642 Single-Chip 76- to 81-GHz mmWave Sensor*. 2018, Texas Instruments.

9 APPENDICES

9.1 MOISTURE SENSOR MATLAB SCRIPTS

9.1.1 MATLAB Control Script

```
addpath(genpath('.\'))
% scale_bool=1; %%this was used for lab testing as the program can interface
% dry_mass=5.7;
% with a scale

%---------------connect_and_collect_with_reference_SmartDryer--------------
%This script connects to the IWR1642BOOST board after it is initialized in
%mmWavestudio and will run data collections and provide estimates of
%sample moisture content. The script reports moisture content in dry basis
%moisture content and assumes it will not see DBMCs below 110. It takes
%inputs of water temperature, sample density, sample thickness, and
%sample type.
%--------------------------------------------------------------------------



%---------------Sample Parameters------------------------------------------
%These must be set when taking the reference!!
temp = 20 ; %Set temperature of water in C
dens = 0.552253; %set the density of the sample in g/cc, unrefined handsheets are
typically around 0.5 g/cc
d=550; % set the thickness of the sample in microns
sample= "unrefined hardwood handsheet"; %set the type of sample, this will change
what the dry relative permittivity is estimated as
%--------------------------------------------------------------------------

k=0;
while(k~=1)
    refSet=input('Is this a reference measurement? (y/n)','s');
    y='y';
    n='n';
    if(strcmp(refSet,y))
        ReferenceBool=true;
        k=1;
    elseif(strcmp(refSet,n))
        ReferenceBool=false;
        k=1;
    else
        disp('Invalid input!')
    end
end

fnm=input('Filename: ','s');

Path= 'C:\ti\mmwave_studio_02_00_00_02\mmWaveStudio';
filePath = append(Path,fnm);

 % Initialize mmWaveStudio .NET connection
```

```
 RSTD_DLL_Path
='C:\ti\mmwave_studio_02_00_00_02\mmWaveStudio\Clients\RtttNetClientController\RtttNe
tClientAPI.dll';

ErrStatus = Init_RSTD_Connection(RSTD_DLL_Path);
if (ErrStatus ~= 30000)
    disp('Error inside Init_RSTD_Connection');
    return;
end
pth='C:\\ti\\mmwave_studio_02_00_00_02\\mmWaveStudio\\PostProc\\';
binpath = append(pth,fnm,'.bin');
binpath =['"' binpath '"'];
capturecommand = append('ar1.CaptureCardConfig_StartRecord(',binpath,', 1)');
capturecommand = ['' capturecommand ''];
%adc_data_path="C:\ti\mmwave_studio_02_00_00_02\rf_eval_firmware\masterss\xwr16xx_mas
terss.bin";
adc_data_path="C:\ti\mmwave_studio_02_00_00_02\mmWaveStudio\PostProc\adc_data_Raw_0.b
in";
%RtttNetClientAPI.RtttNetClient.SendCommand('ar1.CaptureCardConfig_StartRecord("C:\\t
i\\mmwave_studio_02_00_00_02\\mmWaveStudio\\PostProc\\adc_data_Raw_0.bin", 1)')
RtttNetClientAPI.RtttNetClient.SendCommand(capturecommand)
RtttNetClientAPI.RtttNetClient.SendCommand('WriteToLog("First command sent\n",
"green")')
%RtttNetClientAPI.RtttNetClient.SendCommand("ar1.CaptureCardConfig_StartRecord(C:\ti\
mmwave_studio_02_00_00_02\rf_eval_firmware\masterss\xwr16xx_masterss.bin, 1)")
RtttNetClientAPI.RtttNetClient.SendCommand('RSTD.Sleep(1000)')
RtttNetClientAPI.RtttNetClient.SendCommand('ar1.StartFrame()')
RtttNetClientAPI.RtttNetClient.SendCommand('RSTD.Sleep(5000)')
pause(5)
cube = fnm+"_cube.mat";
global Power
global Range
global Raw
rawnme= append(fnm,'_Raw_0.bin');
rawDataReader("C:\ti\OurScripts\IWR1642_moisture_setup.json", rawnme, cube, 1);
%change to rawDataReader_notClosing for debugging
Raw=Raw;
Power = Power';
Range = Range';
writematrix(Raw,fnm + "_rawADC.csv")
writematrix(Power,fnm + "_Power.csv")
writematrix(Range, fnm + "_Range.csv")
if(ReferenceBool)
    ReferenceFFT=Power;
    ReferenceAvg=mean(ReferenceFFT);


else

    [coeff_bru,coeff_loo] = transmissionModel(d,temp,dens,sample);
    SampleFFT=Power;
    SampleAvg=mean(SampleFFT);

    avg_dif = SampleAvg-ReferenceAvg;
    peak_dif = SampleFFT(3)-ReferenceFFT(3);
```

```
    disp(['The loss in dB is ', num2str(avg_dif),])
    Percent_trans = 10^((avg_dif)/10);
    Percent_trans_peak=10^((peak_dif)/10);
    Percent_trans_scaled=10^((avg_dif)/10)*100;
    disp(['The percent transmission is ', num2str(Percent_trans_scaled),])


DBMC_bru=coeff_bru(1)*Percent_trans^7+coeff_bru(2)*Percent_trans^6+coeff_bru(3)*Percent_trans^5+coeff_bru(4)*Percent_trans^4+coeff_bru(5)*Percent_trans^3+coeff_bru(6)*Percent_trans^2+coeff_bru(7)*Percent_trans+coeff_bru(8);

DBMC_loo=coeff_loo(1)*Percent_trans^7+coeff_loo(2)*Percent_trans^6+coeff_loo(3)*Percent_trans^5+coeff_loo(4)*Percent_trans^4+coeff_loo(5)*Percent_trans^3+coeff_loo(6)*Percent_trans^2+coeff_loo(7)*Percent_trans+coeff_loo(8);

    disp(['The moisture content from Looyengas model is ', num2str(DBMC_loo),])
    disp(['The moisture content from Bruggemans model is ', num2str(DBMC_bru),])

%     if(scale_bool==1)         %This is the old code to read the scale
%         sampleMass=scale_reader_function; %this is only for when the scale is connected over USB (assumes COM 12)
%         DBMC_real=((sampleMass-dry_mass)/dry_mass)*100;
%         DBMC_error_loo= DBMC_real-DBMC_loo;
%         DBMC_error_bru=DBMC_real-DBMC_bru;
%
%         fid=fopen(fnm+"_grav_DBMC.txt","w");
%         fprintf(fid,'%s\n','Gravimetric DBMC    Looyenga DBMC   Bruggeman DBMC Looyenga Error  Bruggeman Error');
%         fprintf(fid,'%g\t',DBMC_real);
%         fprintf(fid,'%g\t',DBMC_loo);
%         fprintf(fid,'%g\t',DBMC_bru);
%         fprintf(fid,'%g\t',DBMC_error_loo);
%         fprintf(fid,'%g\t',DBMC_error_bru);
%         fclose(fid);
%     end
end
```

9.1.2 Transmission Model Function

```
function [coeff_bru,coeff_loo] = transmissionModel(d,temp,dens,samp)
%transmissionModel Summary of this function goes here
%   d - Thickness in microns
%   temp - Sample temperature in C
%   dens - Sample density in g/cc
%   samp - Sample code to determine sample type for paper eps
d = d*10^-6;
c=3e8;
minDBMC=110; %minumum expected DBMC
maxDBMC=300; %maximum expected dry basis moisture content, setting this too high may cause issues

freq=77.76756e+9;  %midpoint of radar sweep

[epsP_water,epsPP_water]=debye(temp,freq);     %call debye fit for rel perm of water
[epsP_sample,epsPP_sample]=sampleEps(samp);
```

```
[DBMC,epsP_bru,epsPP_bru,epsP_loo,epsPP_loo]=effMedMods(maxDBMC, epsP_sample,
epsPP_sample, epsP_water, epsPP_water,temp,dens);

[Ref_bru,Trans_bru,TwoTrans_bru,TwoPassTrans_bru] = percentTransSim(epsP_bru,
epsPP_bru, freq, d, c, maxDBMC);
[Ref_loo,Trans_loo,TwoTrans_loo,TwoPassTrans_loo] = percentTransSim(epsP_loo,
epsPP_loo, freq, d, c, maxDBMC);

%plot(DBMC,TwoPassTrans_bru,DBMC,TwoPassTrans_loo)
%plot(TwoPassTrans_loo,DBMC,TwoPassTrans_bru,DBMC)

TwoPassTrans_bru_cut = TwoPassTrans_bru(minDBMC:maxDBMC);
TwoPassTrans_loo_cut = TwoPassTrans_loo(minDBMC:maxDBMC);
DBMC_cut=DBMC(minDBMC:maxDBMC);
cutsize=maxDBMC-minDBMC;
%plot(DBMC_cut,TwoPassTrans_bru_cut,DBMC_cut,TwoPassTrans_loo_cut)
%plot(TwoPassTrans_loo_cut,DBMC_cut,TwoPassTrans_bru_cut,DBMC_cut)
coeff_bru=polyfit(TwoPassTrans_bru_cut,DBMC_cut,7);
coeff_loo=polyfit(TwoPassTrans_loo_cut,DBMC_cut,7);
end
```

9.1.3 Debye Model Function

```
function [epsP_water,epsPP_water] = debye(temp,freq)
%debye - returns relative permittivity of liquid water using 3 parameter
%debye relaxation fitting. Terms from Ellison.

a1=79.3319; b1=0.00432795; c1=0.1353345E-12; d1=653.1149;  a2=3.610705;
b2=0.01069618; c2=3.654087E-16; d2=1220.405; a3=1.966861; b3=0.00251792;
c3=5.098792E-15; d3=396.1829;

Tc=132.4965;
Es=87.9144-0.404399*temp+(9.58726E-4)*temp^2 - (1.32802E-6)*temp^3;
Delta1=a1*exp(-b1*temp); Tau1=c1*exp(d1/(temp+Tc));
Delta2=a2*exp(-b2*temp); Tau2=c2*exp(d2/(temp+Tc));
Delta3=a3*exp(-b3*temp); Tau3=c3*exp(d3/(temp+Tc));

epsP_water=Es-
((2*pi*freq)^2)*(((Tau1^2)*Delta1)/(1+(2*pi*freq*Tau1)^2)+((Tau2^2)*Delta2)/(1+(2*pi*
freq*Tau2)^2)+((Tau3^2)*Delta3)/(1+(2*pi*freq*Tau3)^2));
epsPP_water=
((2*pi*freq))*(((Tau1)*Delta1)/(1+(2*pi*freq*Tau1)^2)+((Tau2)*Delta2)/(1+(2*pi*freq*T
au2)^2)+((Tau3)*Delta3)/(1+(2*pi*freq*Tau3)^2));

end
```

9.1.4 Sample Epsilon Function

```
function [epsP_sample,epsPP_sample] = sampleEps(sample)
%sampleEps - returns relative permittivity of bonedry sample based on input
%string. Data collected from TDS.

if sample=="unrefined hardwood handsheet"
    epsP_sample=1.7035;
    epsPP_sample=0.077965;                          %expand here for new samples
else
```

```
    print("invalid sample, check spelling. Current valid samples are: unrefined
hardwood handsheet")%add new samples to print statement
    return
end

end
```

9.1.5 Effective Medium Model Function

```
function [DBMC,epsP_bru,epsPP_bru,epsP_loo,epsPP_loo]=effMedMods(maxDBMC,
epsP_sample, epsPP_sample, epsP_water, epsPP_water, temp,dens)
%effMedMods - Builds effective medium models of samples over range of DBMC
    DBMC = 0:maxDBMC;
    epsP_bru = zeros(1,maxDBMC+1);
    epsPP_bru = zeros(1,maxDBMC+1);
    epsP_loo = zeros(1,maxDBMC+1);
    epsPP_loo = zeros(1,maxDBMC+1);

    %betP = zeros(1,maxDBMC+1);
    %betPP = zeros(1,maxDBMC+1);

    i=1;
    while(i<maxDBMC+2)
        phi = DBMCtoVolFrac(DBMC(i), temp, dens);
       epsP_loo(i)=(epsP_sample^(1/3)+phi*(epsP_water^(1/3)-epsP_sample^(1/3)))^3;
%looyenga method
       epsPP_loo(i)=(epsPP_sample^(1/3)+phi*(epsPP_water^(1/3)-
epsPP_sample^(1/3)))^3;
       i=i+1;
    end

    j=1;

    while(j<maxDBMC+2)
        eta2=DBMCtoVolFrac(DBMC(j), temp, dens);
             eta1=1-eta2;
             betP = (3*eta1-1)*epsP_sample+(3*eta2-1)*epsP_water;
             epsP_bru(j)= 0.25 * (betP+sqrt(betP^2+8*epsP_sample*epsP_water));
%Bruggeman method eq 1.43 in Effective medium theory
             betPP = (3*eta1-1)*epsPP_sample+(3*eta2-1)*epsPP_water;
             epsPP_bru(j)= 0.25 * (betPP+sqrt(betPP^2+8*epsPP_sample*epsPP_water));
        j=j+1;
    end
end
```